

#### ECG Signal Processing for Respiratory and Autonomic Modulation in Atrial Fibrillation and Environmental Exposure

Abdollahpur, Mostafa

2025

Document Version: Publisher's PDF, also known as Version of record

Link to publication

Citation for published version (APA):

Abdollahpur, M. (2025). ECG Signal Processing for Respiratory and Autonomic Modulation in Atrial Fibrillation and Environmental Exposure. [Doctoral Thesis (compilation), Department of Biomedical Engineering]. Department of Biomedical Engineering, Lund university.

Total number of authors:

Creative Commons License: CC BY-SA

Unless other specific re-use rights are stated the following general rights apply: Copyright and moral rights for the publications made accessible in the public portal are retained by the authors and/or other copyright owners and it is a condition of accessing publications that users recognise and abide by the legal requirements associated with these rights.

• Users may download and print one copy of any publication from the public portal for the purpose of private study

- or research.
- You may not further distribute the material or use it for any profit-making activity or commercial gain
- You may freely distribute the URL identifying the publication in the public portal

Read more about Creative commons licenses: https://creativecommons.org/licenses/

If you believe that this document breaches copyright please contact us providing details, and we will remove access to the work immediately and investigate your claim.

Download date: 21. Nov. 2025

## ECG Signal Processing for Respiratory and Autonomic Modulation in Atrial Fibrillation and Environmental Exposure

#### Mostafa Abdollahpur



#### **DOCTORAL DISSERTATION**

by due permission of the Faculty of Engineering, Lund University, Sweden.

To be defended in E:1406, Ole Römers väg 3, Lund

November 10, 2025, at 09:00

Faculty opponent
Dr. Marianna Meo

Organization: LUND UNIVERSITY Department of Biomedical Engineering	Document name DOCTORAL DISSERTATION Date of issue November 2025
Lund University Box 118, SE-22 1 00, Lund, Sweden  Author: Mostafa Abdollahpur	Sponsoring organization : EU Horizon 2020 MSCA (grant 766082) Swedish Research Council (grant VR2019-04272) Crafoord Foundation (grants 20200605, 20230954)

Title and subtitle:

ECG Signal Processing for Respiratory and Autonomic Modulation in Atrial Fibrillation and Environmental Exposure

Abstract: Atrial fibrillation (AF) is the most common sustained cardiac arrhythmia and is associated with increased risk of stroke, heart failure, and mortality. One of the systems which AF is influenced by is the autonomic nervous system (ANS), which regulates involuntary functions such as heart rate. Environmental stressors, such as air pollution, may also affect these physiological systems and contribute to cardiovascular morbidity. The electrocardiogram (ECG) provides a non-invasive tool to study these influences, but the irregular rhythm of AF poses challenges for conventional respiratory and autonomic analysis. The overall aim of this thesis was to develop ECG-based methods for assessing respiratory and autonomic modulation during AF, and to extend ECG analysis to explore autonomic responses to environmental stressors using different methodological approaches. The first aim was to develop and validate signal processing methods for modeling and tracking respiratory f-wave frequency modulation during AF, as a potential noninvasive marker of autonomic nervous system activity in the atria and of AF progression. This aim is addressed in Papers I and II, which introduced novel algorithms for estimating respiratory fwave frequency modulation from the ECG, and demonstrated that such modulation can be robustly quantified from the ECG, with results suggesting a contribution from parasympathetic activity. The second aim was to examine the influence of autonomic modulation on atrial activity during AF by analyzing respiratory f-wave frequency modulation during tilt-test, and to explore underlying mechanisms using computational modeling. This aim is addressed in Paper III, which combined clinical tilt-table testing in persistent AF patients with biatrial computer simulations to investigate sympathetic and parasympathetic contributions to observed modulation patterns. Results suggested that sympathetic activity primarily influenced the mean fibrillatory rate, while parasympathetic activity appeared to modulate respiration-related variations as a secondary effect rather than as an independent driver. The third aim was to apply ECG-based analysis to assess respiratory and autonomic responses in healthy individuals exposed to hydrotreated vegetable oil (HVO) emissions, using methods distinct from those developed for AF. This aim is addressed in Paper IV, which employed ECG analysis techniques in a controlled human exposure study and indicated that short-term exposure to HVO exhaust did not lead to significant alterations in autonomic or respiratory regulation. In summary, this thesis presents new methods for extracting respiratory and autonomic information from ECGs recorded under challenging conditions, including AF and environmental exposure scenarios. These tools extend the capabilities of ECG analysis, offering potential applications in clinical AF management, environmental health research, and personalized medicine.

Key words:  Atrial fibrillation, f-wave frequency, autonomic nervous system, ECG-Derived respiration, respiratory modulation				
Classification system and/or index terms (if any)				
Supplementary bibliographical information:	Language English			
ISSN and key title:		ISBN 978-91-8104-726-4 (printed) 978-91-8104-727-1(electronic)		
Recipient's notes	Number of pages 180	Price		
	Security classification			

I, the undersigned, being the copyright owner of the abstract of the above-mentioned dissertation, hereby grant to all reference sources permission to publish and disseminate the abstract of the above-mentioned dissertation.

Signature Date: 10 November 2025

#### Public defence

November 10, 2025, at 09:00 in E:1406, E-building, LTH, Ole Römers väg, 223 63 Lund, Sweden.

#### Supervisor

Associate Professor Frida Sandberg

Dept. of Biomedical Engineering, Lund University, Lund, Sweden

#### Co-supervisor

Professor Pyotr G. Platonov

Dept. of Cardiology, Clinical Sciences, Lund University, Lund, Sweden

#### Faculty opponent

Dr. Marianna Meo

Boston Scientific Corp, Kerkrade, Netherlands

#### Examination board

Professor Urban Wiklund

Dept. of Diagnostics and Intervention, Umeå University, Umeå, Sweden

Professor Maria Lindén

Dept. of Intelligent Future Technologies, Mälardalen University, Västerås, Sweden

Associate Professor Johannes Töger

Dept. of Clinical Sciences Lund, Lund University, Lund, Sweden

Deputy member: Professor Andreas Jakobsson

Centre for Mathematical Sciences, Lund University, Lund, Sweden

#### Chairman

Associate Professor Martin Stridh

Dept. of Biomedical Engineering, Lund University, Lund, Sweden

ISBN: 978-91-8104-726-4 (printed version) ISBN: 978-91-8104-727-1 (electronic version)

Report No. 7/25

ISRN: LUTEDX/TEEM-1146-SE

Printed by Tryckeriet, E-building, Faculty of Engineering, Lund University, Lund Sweden

©2025 Mostafa Abdollahpur

Dedicated to my father, **Mohammad**, a man of the land, whose hard work and quiet strength taught me perseverance.

And to my mother, **Roghayeh**, the heart of our home, whose love and unwavering support carried me through every challenge.

## Popular science summary

Atrial fibrillation (AF) is the most common sustained heart rhythm disorder, affecting millions worldwide. It is a progressive condition in which the upper chambers of the heart (the atria) beat rapidly and irregularly due to disorganized electrical activity. This electrical activity controls the contraction of the heart muscle and is influenced not only by the arrhythmia itself but also by the autonomic nervous system, the body's control network for "fight-or-flight" (sympathetic) and "rest-and-digest" (parasympathetic) responses. Breathing patterns and shifts in the balance between these two branches can affect how the heart's electrical signals are generated and conducted. Understanding these interactions is important, as they may play a role in how AF develops and progresses over time, offering clinicians potential markers to better assess heart function and guide more personalized treatment.

This thesis investigates how information contained in the electrocardiogram (ECG) can be used to study respiratory and autonomic influences on the heart, both during AF and during exposure to environmental air pollution. Advanced signal processing techniques are applied to ECG data from patients and healthy volunteers to reveal patterns that cannot be seen through visual inspection alone.

The first part of the work focuses on AF, where the irregular rhythm makes it challenging to measure autonomic nervous system activity from the ECG. New methods are developed to detect subtle variations in the small "f-wave" oscillations of the ECG, characteristic of AF, that are linked to breathing cycles and changes in nervous system activity. The second part applies techniques to study healthy individuals exposed to exhaust from hydrotreated vegetable oil (HVO), a renewable diesel fuel, in order to examine how short-term air pollution affects the heart's regulation.

The results show that, even in the irregular rhythm of AF, it is possible to assess respiratory modulation in the f-wave of the ECG. This modulation appears to be linked to parasympathetic activity in the atrial tissue, offering a new way to study autonomic influences despite the absence of normal heart rhythm. In the environmental exposure studies, different signal processing techniques were applied to ECGs from healthy individuals, but no consistent short-term changes in the heart's autonomic regulation were observed during exposure to exhaust.

Overall, the findings demonstrate that the ECG can serve as a valuable, non-invasive tool for studying respiratory and autonomic function in both disease and environmental health contexts. In the long term, this research could contribute to earlier diagnosis, more tailored treatments, and a better understanding of how environmental factors influence heart health.

## **Abstract**

#### Abstract

Atrial fibrillation (AF) is the most common sustained cardiac arrhythmia and is associated with increased risk of stroke, heart failure, and mortality. One of the systems which AF is influenced by is the autonomic nervous system (ANS), which regulates involuntary functions such as heart rate. Environmental stressors, such as air pollution, may also affect these physiological systems and contribute to cardiovascular morbidity. The electrocardiogram (ECG) provides a non-invasive tool to study these influences, but the irregular rhythm of AF poses challenges for conventional respiratory and autonomic analysis. The overall aim of this thesis was to develop ECG-based methods for assessing respiratory and autonomic modulation during AF, and to extend ECG analysis to explore autonomic responses to environmental stressors using different methodological approaches.

The first aim was to develop and validate signal processing methods for modeling and tracking respiratory f-wave frequency modulation during AF, as a potential non-invasive marker of autonomic nervous system activity in the atria and of AF progression. This aim is addressed in Papers I and II, which introduced novel algorithms for estimating respiratory f-wave frequency modulation from the ECG, and demonstrated that such modulation can be robustly quantified from the ECG, with results suggesting a contribution from parasympathetic activity.

The second aim was to examine the influence of autonomic modulation on atrial activity during AF by analyzing respiratory f-wave frequency modulation during tilt-test, and to explore underlying mechanisms using computational modeling. This aim is addressed in Paper III, which combined clinical tilt-table testing in persistent AF patients with biatrial computer simulations to investigate sympathetic and parasympathetic

iv Abstract

contributions to observed modulation patterns. Results suggested that sympathetic activity primarily influenced the mean fibrillatory rate, while parasympathetic activity appeared to modulate respiration-related variations as a secondary effect rather than as an independent driver.

The third aim was to apply ECG-based analysis to assess respiratory and autonomic responses in healthy individuals exposed to hydrotreated vegetable oil (HVO) emissions, using methods distinct from those developed for AF. This aim is addressed in Paper IV, which employed ECG analysis techniques in a controlled human exposure study and indicated that short-term exposure to HVO exhaust did not lead to significant alterations in autonomic or respiratory regulation.

In summary, this thesis presents new methods for extracting respiratory and autonomic information from ECGs recorded under challenging conditions, including AF and environmental exposure scenarios. These tools extend the capabilities of ECG analysis, offering potential applications in clinical AF management, environmental health research, and personalized medicine.

## **Contributions**

#### **Included**

I. Respiratory Induced Modulation in f-Wave Characteristics During Atrial Fibrillation

**Mostafa Abdollahpur**, Fredrik Holmqvist, Pyotr G. Platonov, Frida Sandberg *Published in: Frontiers in Physiology, vol. 12, 653492, 2021* 

The author developed the methodology for quantifying respiratory-induced modulation in f-wave frequency trends from ECG signals. The author implemented the entire signal processing pipeline, conducted simulations, and performed statistical analyses. The author analyzed the results and wrote the manuscript.

II. A Subspace Projection Approach to Quantify Respiratory Variations in the f-wave Frequency Trend.

**Mostafa Abdollahpur**, Gunnar Engström, Pyotr G. Platonov, Frida Sandberg *Published in: Frontiers in Physiology, vol. 13, 976925, 2022* 

The author proposed to use the orthogonal subspace projection method for the analysis introduced in the study. The author implemented the analysis framework and applied it to both simulated and clinical data. The author conducted all statistical analyses and interpreted the findings in relation to respiratory modulation and autonomic control. The author wrote the manuscript.

III. Tilt-induced changes in f-wave characteristics during atrial fibrillation: an experimental and computational investigation.

Mostafa Abdollahpur †, Chiara Celotto †, Carlos Sanchez, Felix Plappert,

vi Contributions

Sten Östenson, Pyotr Platonov, Pablo Laguna, Esther Pueyo, Frida Sandberg *Published in: Frontiers in Physiology, vol. 16, 1498426, 2025* 

†These authors have contributed equally to this work and share first authorship. The author was primarily responsible for the development and implementation of ECG preprocessing, f-wave frequency trend estimation, and respiratory modulation analysis. The author processed the clinical data and contributed to the interpretation of the results. The author was involved in the study design and collaborated closely with co-authors on experimental design and integration with computational modeling outcomes. The author co-wrote the manuscript.

## IV. A Chamber Study of Respiratory and Autonomic Responses to Hydrotreated Vegetable Oil Exhaust Using ECG-Derived Respiration.

**Mostafa Abdollahpur**, Louise Gren, Katrin Dierschke, Leo Stockfelt, Aneta Wierzbicka, Frida Sandberg

Manuscript

The author implemented the ECG signal processing framework used to extract heart rate variability and ECG-derived respiration features. The author applied established methods for linear and nonlinear cardiorespiratory coupling analysis and conducted the statistical modeling using linear mixed-effects models. The author interpreted the physiological effects of short-term pollutant exposure and integrated the findings with prior work. The author wrote the manuscript.

#### **Related Work**

Parts of this research were initially presented at scientific conferences and published as conference papers.

- I. Respiratory Modulation in Permanent Atrial Fibrillation Mostafa Abdollahpur, Fredrik Holmqvist, Pyotr G. Platonov, Frida Sandberg In Proceedings of Computing in Cardiology, Rimini, Italy, 2020.
- II. Relationship between atrial oscillatory acetylcholine release pattern and f-wave frequency modulation: a computational and experimental study Chiara Celotto, Carlos Sánchez, Konstantinos A Mountris, Mostafa Abdollahpur, Frida Sandberg, Pablo Laguna, Esther Pueyo

In Proceedings of Computing in Cardiology, Rimini, Italy, 2020.

## III. Dependence of Atrial Fibrillatory Rate Variations Induced by Head-Up/Down Tilt-Test on Autonomic Action

Chiara Celotto, Carlos Sánchez, **Mostafa Abdollahpur**, Frida Sandberg, Pablo Laguna, Esther Pueyo

In Proceedings of Computing in Cardiology, Atlanta, GA, USA, 2023.

In addition to the work included in this thesis, the author contributed to several collaborative studies during the Ph.D. period.

## I. Heart rate characteristic based modelling of atrial fibrillatory rate using implanted cardiac monitor data

Javier Saiz-Vivo, **Mostafa Abdollahpur**, Luca T Mainardi, Valentina D. A. Corino, Mirko De Melis, Robert Hatala, Frida Sandberg *Published in: Physiological Measurement, vol. 44, nr. 3, 035007, 2023* 

#### II. An atrioventricular node model incorporating autonomic tone

Felix Plappert, Mikael Wallman, **Mostafa Abdollahpur**, Pyotr G Platonov, Sten Östenson, Frida Sandberg

Published in: Frontiers in Physiology, vol. 13, 976468, 2022

## III. The frequency of atrial fibrillatory waves is modulated by the spatiotemporal pattern of acetylcholine release: a 3D computational study

Chiara Celotto, Carlos Sánchez, **Mostafa Abdollahpur**, Frida Sandberg, Jose F Rodriguez Mstas, Pablo Laguna, Esther Pueyo

Published in: Frontiers in Physiology, vol. 14, 1189464, 2024

## **Acknowledgments**

Like most things in life, this thesis is not the result of my efforts alone. Over the years leading up to it, I have been fortunate to receive support, guidance, and encouragement from many people, friends, colleagues, and mentors, some of whom I now consider to be both. First of all, I would like to express my deepest gratitude to my supervisor, *Frida*, who gave me this opportunity and, in many ways, changed the direction of my life. Your guidance, encouragement, and support over these past seven years have shaped not only this thesis but also my development as a researcher and as a person. I would also like to sincerely thank my co-supervisor, *Pyotr*, for offering new perspectives, thoughtful advice, and invaluable feedback throughout this journey.

I am grateful to the Biomedical Signal Processing group: Felix, Martin, Mattias, Mikael, and William, for all your help and our many fruitful discussions. A very special thanks goes to Leif, not only for our inspiring conversations but also for his encouragement and wise advice throughout my time there. I also want to thank Ulrika for her kindness and support in special moments, and both Ammi and her for the Friday music sessions that I will always remember. I am thankful to all my colleagues at the Department of Biomedical Engineering for creating a warm and friendly workplace. A big thank you also goes to Johan G., for your help and for being such a great office mate.

I would like to thank my dearest friends, *Azin* and *Hesam*. We began this journey together, and after seven years I am deeply grateful to have shared it with you. To *Nika*, you were the very first person I contacted before I even knew anyone in Lund or Sweden, and meeting you has truly been one of the best things that happened to me here.

I am also grateful for the friends I made during my time in Lund: Ali, Ali H., Ashkan, Hassan, Harry, Hedieh, Natalie, Negin, Peyman, Saeed, Shaghayegh, Sima, and Soren. I am deeply thankful for the many moments we shared, from trips and meals to gatherings, activities, and simple everyday conversations. Your friendship brought joy, balance, and meaning to my years in Lund, and the memories we created together will stay with me always.

To my old friends from Iran, with whom I started the PhD journey after our master's, thank you for the continued friendship even as life took us to different places. Most of you are now doctors: *Amin, Danial, Mehrdad, Mohammadreza, Peyman F., Poorya, Saeed, Sina, Soroush*, and *Zahra*, and I am proud to have shared part of the road with you. I would also like to thank my friends in Stockholm, *Pooyeh* and *Reza*, for their support and kindness. In my final year in Gothenburg, I was fortunate to meet new friends who helped me through that stage of the journey. Thank you all.

Last but not least, I want to express my deepest gratitude to my parents, who have always supported me and encouraged my pursuit of education and science for as long as I can remember. Their endless sacrifices, patience, and belief in me have laid the foundation for everything I have achieved, and I am forever indebted to them. I also want to thank my brother, *Meraj*, for all the cherished memories of our childhood together, you will always hold a special place in my heart, and those memories continue to give me joy and strength.

Finally, I wish to thank the love of my life, *Maryam*. Words cannot fully capture how grateful I am for your presence in my life. Your love, patience, and constant belief in me have been a source of strength and inspiration throughout this journey. You have been my anchor in difficult times and my greatest joy in the good ones. Your unwavering encouragement gave me the courage to keep going when challenges felt overwhelming, and your kindness reminded me of what truly matters beyond work and studies. This achievement is not mine alone, but something we share, because your support has been woven into every step I have taken. I look forward to all the journeys that still lie ahead of us, both in life and in love, with gratitude that I get to walk them with you.

## List of Abbreviations

AF Atrial fibrillation

AFR Atrial fibrillatory rate

ANS Autonomic nervous system

AV Atrioventricular

ECG Electrocardiogram

**EDR** ECG-derived respiration

f-waves Atrial fibrillatory waves

HRV Heart rate variability

HVO Hydrotreated vegetable oil

QRST Ventricular depolarization and repolarization (QRS complex + T wave)

**RR** Interval between consecutive ventricular activations

**SA** Sinoatrial

# Contents

ľo	pular science summary	1
Ał	stract	iii
Co	ntributions	v
Ac	knowledgments	viii
Li	t of Abbreviations	xi
Ι	Introduction	1
1	Background and Aims	3
	1.1 Background and Motivation	3
	1.2 Thesis Aims	4
	1.3 Thesis Structure	
2	Medical Background	5
	2.1 Anatomy and Function of the Heart	5
	2.2 Cardiac Conduction System	6
	2.3 Autonomic Nervous System and Cardiac Regulation	11
	2.4 Atrial Fibrillation	16
3	ECG Based Analysis of Atrial Fibrillation	19
	3.1 ECG in AF	19
	3.2 Extraction of f-waves	20

xiv Contents

	3.3	Characterization of f-waves	27
	3.4	Modelling of f-waves	34
4	ECG	Based Analysis of Respiration	41
	4.1	ECG-derived respiration	41
	4.2	Robust Assessment of Respiratory Information	46
	4.3	Assessment of Cardiorespiratory Interactions	48
5	Sum	mary of Papers	55
	5.1	Paper I - Respiratory Induced Modulation in f-wave Characteristics	
		During Atrial Fibrillation	56
	5.2	Paper II - A Subspace Projection Approach to Quantify Respiratory	
		Variations in the f-wave Frequency Trend	58
	5.3	Paper III - Tilt-induced Changes in f-wave Characteristics During	
		Atrial Fibrillation: An Experimental and Computational Investigation	60
	5.4	Paper IV - A Chamber Study of Respiratory and Autonomic Re-	
		sponses to Hydrotreated Vegetable Oil Exhaust Using ECG-Derived	
		Respiration	62
II	Inc	luded Papers	77

# Part I Introduction

Chapter 1

## **Background and Aims**

#### 1.1 Background and Motivation

Atrial fibrillation (AF) is the most prevalent sustained cardiac arrhythmia and a leading cause of cardiovascular morbidity worldwide [1]. Although the clinical features, mechanisms, and management strategies of AF have been extensively studied and are further reviewed in Chapters 2 and 3, many aspects remain under active investigation. Among these, the role of the autonomic nervous system (ANS) is of particular interest, as impaired autonomic modulation has been linked to both the initiation and progression of AF. Understanding these influences requires new non-invasive approaches, since existing methods are either invasive or inadequate in the absence of sinus rhythm. Capturing autonomic modulation directly from surface electrocardiogram (ECG) recordings therefore represents a promising, yet underexplored, direction of research. This thesis investigates whether respiratory variations in atrial activity, reflected in the frequency and morphology of f-waves, can serve as novel markers of autonomic influence during AF. Since these variations are subtle and often masked by other sources of variability, advanced signal processing techniques are essential for their reliable assessment.

Beyond AF, the thesis also explores ECG-derived markers of autonomic and respiratory regulation in healthy individuals exposed to environmental stressors such as hydrotreated vegetable oil (HVO) emissions. Although the clinical contexts differ, both applications rely on the same methodological foundation: the development of signal processing techniques to extract autonomic and respiratory information from surface ECG data. Together, these two branches aim to advance the use of the ECG as a versatile, non-invasive tool for studying autonomic—cardiac interactions under both pathological and physiological conditions.

#### 1.2 Thesis Aims

The overarching goal of this thesis is to develop and apply signal processing methods for analyzing autonomic modulation based on surface ECG recordings. The specific aims of the thesis, along with their connection to the individual studies, are as follows:

- Aim 1: To develop and validate signal processing methods for modeling and tracking respiratory f-wave frequency modulation during AF. (Addressed in Papers I and II)
- Aim 2: To investigate the association between respiratory f-wave frequency modulation and ANS activity. (Addressed in Paper III)
- Aim 3: To develop and validate signal processing methodology for continuous monitoring of respiratory and autonomic responses in healthy individuals in environmental exposure studies. (Addressed in Paper IV)

Together, these aims reflect a multidisciplinary effort to enhance the informational value of ECG signals, providing new tools for both AF-specific monitoring and broader cardiorespiratory assessment.

#### 1.3 Thesis Structure

This thesis is divided into two main parts. *Part I* establishes the conceptual and methodological foundation, while *Part II* presents the four original research papers that form the core scientific contributions of this work.

The subsequent sections of *Part I* are organized as follows: Chapter 2 provides the necessary medical background, including cardiac electrophysiology, autonomic regulation, respiratory dynamics, and the pathophysiology of AF. Chapter 3 is devoted to ECG-based analysis of AF, describing how AF manifests in the surface ECG, methods for extracting and characterizing fibrillatory waves (f-waves), and modelling strategies for quantifying atrial activity. Chapter 4 turns to ECG-derived respiration, outlining the methods used to extract respiratory information and assess cardiorespiratory interactions, with particular emphasis on respiratory rate estimation, orthogonal subspace projection, and coupling analysis. Finally, Chapter 5 summarizes the four research papers included in *Part II*, highlighting their individual contributions and showing how they collectively address the overarching aims of the thesis.

## Chapter 2

## Medical Background

#### 2.1 Anatomy and Function of the Heart

The human heart is a central organ in the circulatory system, tasked with continuously pumping blood to sustain life. It is structurally divided into two sides, left and right, each composed of an upper chamber (atrium) and a lower chamber (ventricle). The heart's ability to circulate blood effectively hinges on its coordinated electrical and mechanical activity, which manifests as cyclic phases of contraction (systole) and relaxation (diastole). Blood flow through the heart is regulated by four valves: the atrioventricular valves (the tricuspid on the right and the mitral on the left) and the semilunar valves (the pulmonary and aortic valves). These valves function to maintain unidirectional blood flow, allowing forward progression while preventing backflow.

On the right side, deoxygenated blood returns from the systemic circulation via the *superior* and *inferior vena cavae*, entering the *right atrium* (RA). Blood from the heart's own tissue drains into the RA through the coronary sinus. From the RA, blood passes through the tricuspid valve into the *right ventricle* (RV), which serves as the main pumping chamber of the right heart. During systole, the RV ejects blood across the pulmonary valve into the pulmonary artery, directing it to the lungs for gas exchange.

In the lungs, oxygen is absorbed through alveolar-capillary diffusion, and the oxygen-rich blood returns to the heart via four *pulmonary veins*, two from each lung, into the *left atrium* (LA). The LA acts as a reservoir before the blood flows through the mitral valve into the *left ventricle* (LV). The LV, the most muscular chamber of the heart, propels oxygenated blood through the *aortic valve* into the aorta, supplying the systemic circulation. An overview of the heart's anatomical structures and blood flow pathways is presented in Figure 2.1.

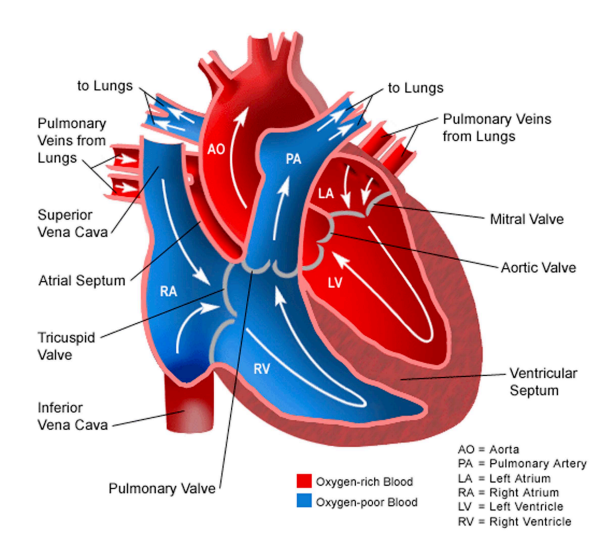


**Figure 2.1:** Anatomical overview of the heart chambers, valves, and blood flow direction. Deoxygenated blood (blue) returns via the venae cavae to the right atrium and is pumped to the lungs through the pulmonary artery. Oxygenated blood (red) returns via the pulmonary veins to the left atrium and is distributed to the systemic circulation through the aorta. Adapted from [2].

#### 2.2 Cardiac Conduction System

The rhythmic contraction of the heart is governed by its intrinsic conduction system, a specialized electrical network responsible for initiating and coordinating the impulses that drive myocardial activity. This system ensures that atrial and ventricular contractions occur in a precise, timely sequence, an essential requirement for effective cardiac output [2]. At the core of this system lies the *sinoatrial* (SA) node, located in the upper wall of the right atrium near the superior vena cava. It acts as the heart's primary pacemaker. Composed of autorhythmic, self-excitable cells, the SA node spontaneously generates electrical impulses at an intrinsic rate of approximately 100–120 beats per minute in the absence of autonomic regulation [3]. These impulses are finely modulated by the ANS, which adjusts the heart rate in response to physiological demands such as stress, exercise, or rest.

Once initiated in the SA node, the electrical activation spreads across the atrial myocardium, triggering atrial contraction and promoting blood flow into the ventricles. The impulse then reaches the *atrioventricular (AV) node*, located at the junction between the atria and ventricles. Here, the signal is briefly delayed, a critical pause that allows the ventricles adequate time to fill following atrial contraction. Following this delay, the electrical impulse proceeds along the *bundle of His*, which quickly bifurcates into the *right* and *left bundle branches* running along the interventricular septum. These branches carry the signal toward the apex of the heart, where it enters the *Purkinje fibers*. This dense, rapidly conducting fiber network distributes the impulse throughout the ventricular myocardium, ensuring a synchronized and powerful contraction of both ventricles.

This highly structured sequence of depolarization and repolarization, originating in the SA node and concluding with ventricular contraction, is what underlies the characteristic waveforms seen in the surface ECG. The conduction system plays a vital role in sustaining the heart's rhythmic pumping function, and any disruption to this system can lead to serious arrhythmias or compromised cardiac output. An overview of this electrical pathway is illustrated in Figure 2.2.

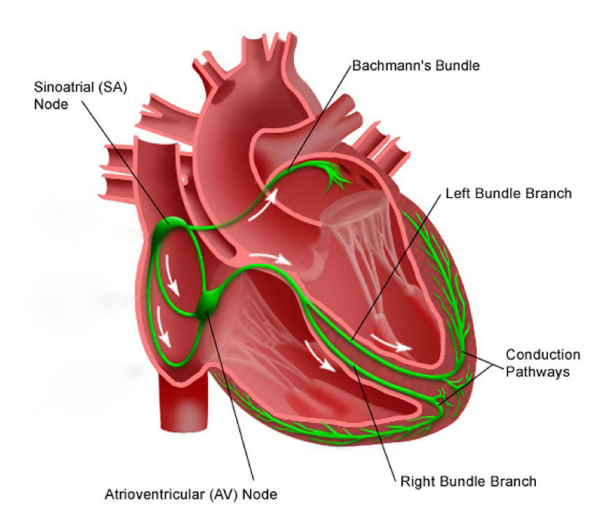


**Figure 2.2:** Illustration of the cardiac conduction system. Electrical impulses originate at the sinoatrial (SA) node and propagate through internodal tracts to the atrioventricular (AV) node. The impulse is then transmitted via the bundle of His, dividing into the right and left bundle branches, and dispersed throughout the ventricles via Purkinje fibers to ensure coordinated contraction. Adapted from [2].

#### 2.2.1 Cellular Electrical Activity

At the cellular level, the electrical behavior of cardiomyocytes is governed by the dynamic interplay of ion movement across the cell membrane. This membrane is composed of a semi-permeable phospholipid bilayer embedded with a variety of proteins, including ion channels, pumps, transporters, and receptors. These components are essential not only for maintaining the ionic homeostasis of the cell but also for mediating signal transmission and supporting metabolic processes. Ion channels facilitate passive movement of ions along electrochemical gradients, driven by both concentration differences (chemical gradient) and voltage differences across the membrane (electrical gradient). In contrast, active transport mechanisms, such as ion pumps and exchangers, move ions against their gradients. These processes are energy-dependent and typically regulated by shifts in membrane potential, intracellular ion concentrations, or the presence of signaling molecules [4]. In addition to these transmembrane mechanisms, cardiomyocytes are electrically coupled to one another through gap junctions. These specialized intercellular connections, formed by connexin proteins, create low-resistance pathways that allow ions and small molecules to pass directly between neighboring cells. Gap junctions are critical for the rapid spread of action potentials across the atrial and ventricular myocardium, ensuring coordinated contraction at the tissue level.

In a resting atrial cardiomyocyte, the membrane potential is typically between -65 and -80 mV, with the cell interior being more negatively charged than the exterior. This resting membrane potential arises from a high intracellular concentration of potassium ions (K<sup>+</sup>) and lower concentrations of sodium (Na<sup>+</sup>) and calcium (Ca<sup>2+</sup>) ions. Extracellularly, Na<sup>+</sup> and Ca<sup>2+</sup> are abundant, while K<sup>+</sup> levels are relatively low [5].

Upon electrical stimulation, the cardiomyocyte generates an action potential (AP), a rapid and transient depolarization of the membrane followed by repolarization. The AP is conventionally divided into five phases, illustrated in Figure 2.3. These phases are as follows:

- **Phase 0** *Rapid depolarization*: A sudden influx of  $Na^+$  through voltage-gated sodium channels increases the transmembrane potential sharply, generating the fast sodium current  $(I_{Na})$ .
- Phase 1 *Initial repolarization*: As Na<sup>+</sup> channels inactivate, transient outward K<sup>+</sup> currents (I<sub>to</sub>) initiates a brief repolarization of the cell.
- **Phase 2** *Plateau phase*: A balance forms between inward Ca<sup>2+</sup> current through L-type calcium channels (I<sub>CaL</sub>) and outward delayed rectifier K<sup>+</sup> currents (I<sub>Kur</sub>),

producing a relatively stable membrane potential. A small persistent  $Na^+$  current  $(I_{NaL})$  may also contribute, extending the duration of the plateau.

- Phase 3 Repolarization:  $Ca^{2+}$  channels inactivate while outward  $K^+$  currents dominate. These include the rapid  $(I_{Kr})$  and slow  $(I_{Ks})$  delayed rectifier currents, as well as the inward rectifier current  $(I_{K1})$ , which gradually restores the membrane to its resting state.
- Phase 4 Resting state: The membrane potential stabilizes at its resting level.
   I<sub>K1</sub> remains active, and the Na<sup>+</sup>/K<sup>+</sup> ATPase pump helps maintain ion gradients by moving Na<sup>+</sup> out and K<sup>+</sup> into the cell.

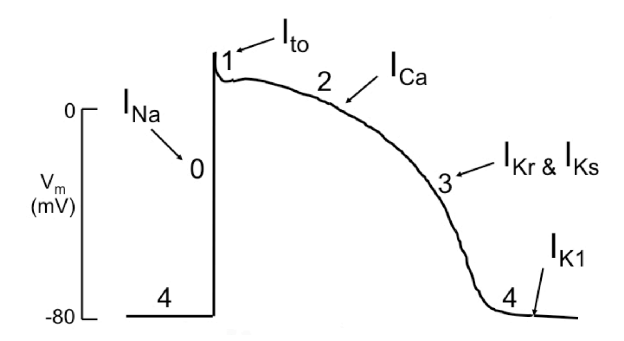


**Figure 2.3:** Schematic representation of the cardiac action potential and corresponding ionic currents in each phase. Adapted from [6].

Additional ionic mechanisms refine the atrial action potential. For example, voltage-gated and calcium-activated chloride channels contribute to fine-tuning repolarization. Similarly, the  $\mathrm{Na^+/Ca^{2^+}}$  exchanger plays a dual role. During rest, it removes intracellular  $\mathrm{Ca^{2^+}}$ , contributing to an inward current. During early repolarization, it can operate in reverse mode, briefly generating an outward current before switching back to help extrude calcium. Another player is the small-conductance calcium-activated potassium (SK) channel, which becomes active in response to increased intracellular  $\mathrm{Ca^{2^+}}$  during the plateau phase. This activation leads to a potassium efflux, aiding in repolarization [6].

The morphology and kinetics of action potentials vary between cardiac regions. In humans, atrial action potentials (APs) typically display a triangular profile, distinct from the spike-and-dome configuration of ventricular APs (see Figure 2.4.A). A common measure of AP duration is APD<sub>90</sub>, defined as the time interval from the initial depolarization to 90% repolarization. In atrial cells, APD<sub>90</sub> can vary significantly,

from 150 to 500 ms depending on heart rate and experimental conditions. The resting potential in atrial cells is also more depolarized than in ventricular cells, largely due to lower  $I_{K1}$  density [7].

Electrophysiologically, the AP cycle includes distinct refractory periods that are essential for maintaining normal cardiac rhythm. The absolute refractory period refers to the phase during which no stimulus, regardless of its strength, can trigger a new AP, as the sodium channels remain inactivated. This is followed by the relative refractory period, during which a new AP can be initiated, but only by a stimulus that is stronger than usual. Finally, the cell enters the resting phase, where membrane potential returns to baseline and normal excitability is restored. Together, these phases ensure orderly depolarization and prevent the heart from undergoing abnormal or premature re-excitation [8].

#### 2.2.2 Electrocardiography (ECG)

The ECG is a widely used, non-invasive method for recording the electrical activity of the heart. It is obtained by placing electrodes at standardized positions on the body surface, allowing the detection of voltage gradients generated by the depolarization and repolarization of cardiac tissue. The resulting signal provides a composite view of the heart's electrical behavior during each cardiac cycle. A standard 12-lead ECG configuration involves the use of 10 surface electrodes: 4 limb electrodes, positioned on the arms and legs to capture activity in the frontal plane, and 6 precordial (chest) electrodes, positioned across the thorax to capture activity in the horizontal plane. These electrodes generate 12 distinct leads, comprising 3 bipolar limb leads (I, II, and III), 3 augmented unipolar limb leads (aVR, aVL, and aVF), and 6 unipolar precordial leads (V1–V6). Bipolar leads, such as leads I, II, and III, measure the potential difference between two specific electrodes. In contrast, unipolar leads (augmented and precordial) measure the potential difference between a positive electrode and a calculated central terminal, which acts as a reference composed of a combination of other limb electrodes.

The ECG waveform consists of several key components that reflect specific phases of cardiac electrical activity. The *P-wave* corresponds to atrial depolarization, while the *QRS-complex* represents rapid depolarization of the ventricles. Due to the greater muscle mass of the left ventricle, it contributes more prominently to the ECG signal. Atrial repolarization, though present, is typically obscured by the QRS complex. The *T-wave* reflects ventricular repolarization.

Additional intervals provide further information about cardiac function. The *QT-interval* encompasses the full duration of ventricular depolarization and repolarization. The *ST-segment*, typically an isoelectric period, marks the interval between ventricular depolarization and the beginning of repolarization. The *RR-interval* indicates the time between two consecutive R-waves and is commonly used to assess heart rate and its variability. Figure 2.4.B illustrates the relationship between ECG waveforms and action potentials recorded from various cardiac cell types. The figure emphasizes how the coordinated electrical activity of atrial, ventricular, and nodal cells contributes to the overall ECG signal.

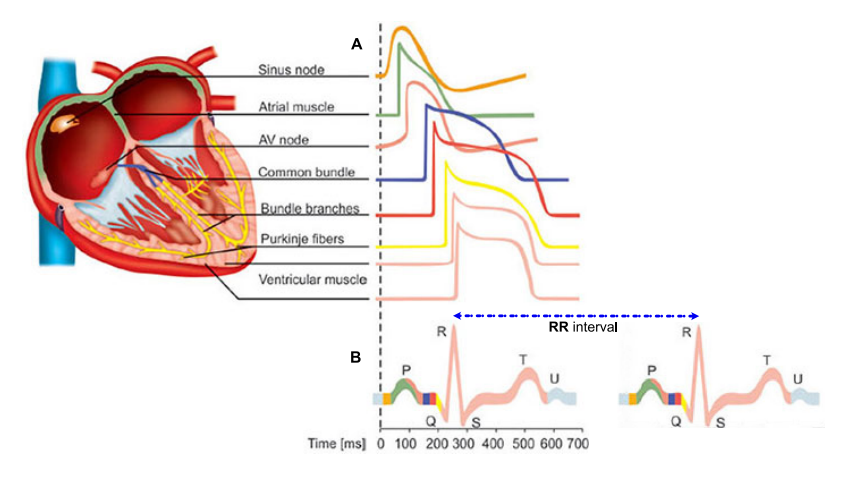


**Figure 2.4:** Schematic representation of ECG waveforms and corresponding action potentials from different cardiac cell types. Adapted from [9].

### 2.3 Autonomic Nervous System and Cardiac Regulation

The ANS plays a vital role in maintaining homeostasis, ensuring stable internal conditions such as pH, temperature, and nutrient levels despite changes in the external environment. This system continuously monitors physiological parameters and initiates appropriate adjustments to preserve a narrow range of values compatible with life [10].

For the cardiovascular system, the ANS enables the heart to dynamically adapt to both internal and external stimuli. It regulates heart rate and contractility through a balance of sympathetic and parasympathetic activity. This autonomic modulation is critical for maintaining proper circulation and responding to varying physiological demands. Dysregulation of autonomic input to the heart has been linked to multiple cardiovascular pathologies, including heart failure, hypertension, and arrhythmias [11]. Autonomic control of cardiac function is governed by a highly integrated system comprising both intrinsic and extrinsic components, collectively referred to as the cardiac autonomic nervous system [12]. The cardiac autonomic nervous system operates through two primary branches: the sympathetic nervous system, which orchestrates the body's "fight-or-flight" responses, and the parasympathetic nervous system, which promotes "rest-and-digest" activities associated with recovery and conservation of energy.

Both branches of the ANS are tonically active, meaning they provide continuous, baseline levels of input. Typically, they exert opposing effects on target tissues. When one branch increases its activity and the other decreases, this reciprocal relationship enables rapid and precise modulation of physiological functions. In the context of cardiovascular control, parasympathetic activation results in a reduction of heart rate and cardiac output, leading to lower blood pressure. In contrast, sympathetic activation enhances heart rate and myocardial contractility, increases stroke volume, and induces vasoconstriction. These changes elevate both cardiac output and systemic vascular resistance, thereby increasing blood pressure [13].

The functional effects of ANS activation are mediated through the release of specific neurotransmitters. The two primary neurotransmitters involved are acetylcholine (ACh), released by cholinergic neurons, and norepinephrine (NE), released by adrenergic neurons. Both the sympathetic and parasympathetic pathways are organized into two-neuron chains consisting of a preganglionic neuron, which originates in the central nervous system and projects to an autonomic ganglion, and a postganglionic neuron, which extends from the ganglion to the target organ. In both systems, the preganglionic neurons are cholinergic and release ACh. However, the postganglionic neurons differ: in the parasympathetic system, they are predominantly cholinergic and also release ACh, whereas in the sympathetic system, they are primarily adrenergic and release NE. This divergence in neurotransmitter output leads to distinct physiological effects, enabling the ANS to finely regulate cardiac function under a range of conditions [14].

#### 2.3.1 Extrinsic and Intrinsic Cardiac Autonomic Nervous System

The cardiac autonomic nervous system operates through a hierarchical structure composed of both extrinsic and intrinsic components. Together, these elements form a complex neural network that coordinates autonomic control of the heart. The extrin-

sic component includes central nervous system and intrathoracic extracardiac structures, while the intrinsic component consists of localized neural circuits embedded within the heart itself.

The extrinsic cardiac ANS comprises neuronal structures originating from the brain and spinal cord, whose axons project toward the heart. These include the *vagosympathetic trunk* and other ganglionic chains that relay sympathetic or parasympathetic input to cardiac tissues. The sympathetic arm of the extrinsic cardiac ANS primarily derives from autonomic ganglia located along the cervical and thoracic spinal segments. These include the superior *cervical ganglia* (linked to C1–C3), the *stellate* or *cervicothoracic ganglia* (linked to C7–T2), and *thoracic ganglia* [15, 16]. Parasympathetic preganglionic fibers travel via branches of the *vagus nerve*, subdivided into superior, middle, and inferior pathways. These fibers often converge in a region known as the "third fat pad," located between the superior vena cava and the aorta, from where they innervate the SA and AV nodes [17]. The activity of these parasympathetic fibers is governed by cardiac vagal motor neurons located in the medulla oblongata, which integrate inputs from higher brain centers, respiratory networks, and baroreceptor reflex pathways. This anatomical arrangement is illustrated in Figure 2.5.

By contrast, the intrinsic cardiac ANS is situated directly within cardiac tissue and functions as the final relay station for the regulation of regional cardiac activity. It is composed of afferent sensory neurons, interconnecting local circuit neurons, and efferent neurons with either adrenergic or cholinergic phenotypes. These neurons communicate with extrinsic ganglia and respond to both neural and humoral signals, including input from the central nervous system and circulating catecholamines. The intrinsic cardiac ANS modulates key physiological parameters such as heart rate, myocardial refractoriness, conduction velocity, contractility, and coronary blood flow. Notably, the intrinsic cardiac ANS can exert regulatory influence independently of the extrinsic cardiac ANS, as evidenced by preserved cardiac control even after heart autotransplantation (a surgical procedure in which the heart is removed and reimplanted in the same individual, thereby eliminating external neural inputs) [18, 19, 20].

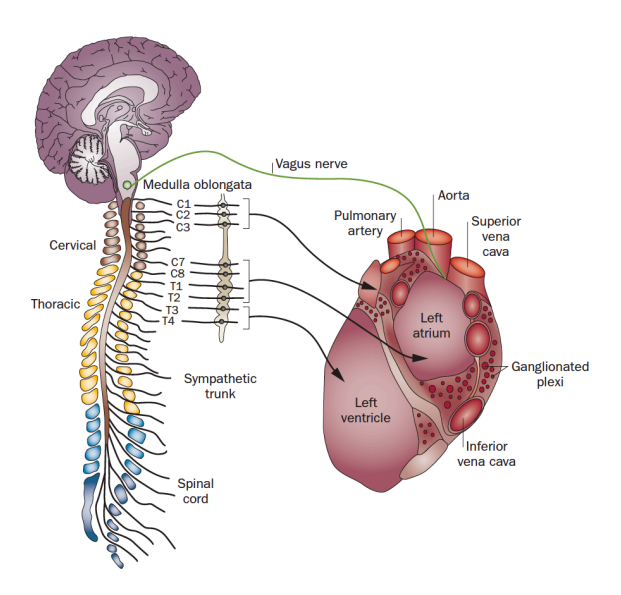


**Figure 2.5:** Anatomy of sympathetic and parasympathetic innervation of the heart. Reproduced with permission from Shen et al. [21], *Neural mechanisms of atrial arrhythmias, Nature Reviews Cardiology*, 2011. © Springer Nature.

#### 2.3.2 Cardiorespiratory Coupling and Heart Rate Variability

Respiratory sinus arrhythmia (RSA) is one of the most well-recognized manifestations of *cardiorespiratory coupling*, the physiological interplay between the cardiovascular and respiratory systems. Although anatomically distinct, these systems are functionally integrated through central autonomic pathways. Neural coupling originates in the brainstem, specifically the medulla oblongata, which houses the primary respiratory centers. These centers modulate vagal efferent output to the heart (cf. Sec. 2.3.1), primarily through cardiac vagal motor neurons [22]. This interaction produces phase-locked inhibition of vagal tone during inspiration and its restoration during expiration, giving rise to the beat-to-beat modulation observed in RSA, illustrated in Figure 2.6.

In addition to central neural control, mechanical factors also contribute. Changes in intrathoracic pressure during respiration alter venous return and activate the *baroreceptor reflex*. Baroreceptors, located in the carotid sinus and aortic arch, sense fluctuations in arterial pressure and trigger compensatory adjustments in heart rate and vascular tone via autonomic pathways [24]. The combined neural and mechanical mechanisms make RSA a sensitive index of parasympathetic responsiveness. It is typically more

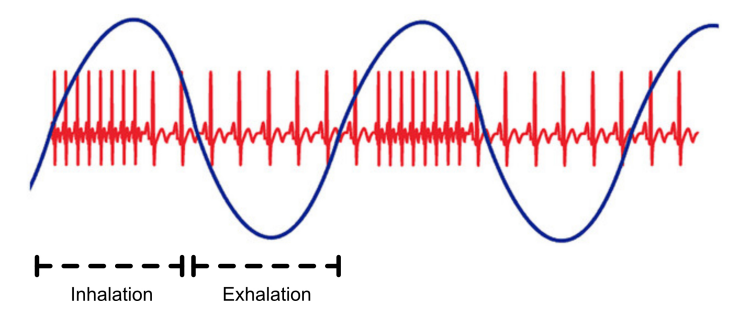


**Figure 2.6:** Schematic illustration of RSA, showing the ECG signal and respiratory trace. RR intervals shorten during inhalation and lengthen during exhalation, reflecting vagal modulation of heart rate. Adapted from [23].

pronounced at rest, particularly during slow and deep breathing, and attenuates under stress, during physical exertion, or when sympathetic activity dominates. RSA is also age-dependent, being strongest in healthy children and young adults, and progressively declining with aging, cardiovascular disease, and autonomic neuropathies [25].

Heart rate variability represents a broader non-invasive marker of autonomic regulation, reflecting the dynamic balance between sympathetic and parasympathetic activity. Reduced HRV has been consistently associated with impaired cardiac autonomic control and increased risk of adverse cardiovascular outcomes [26]. HRV is also sensitive to environmental and physiological stressors; for instance, air pollution, temperature extremes, and psychological stress can reduce HRV, signaling a shift in autonomic balance and increased cardiovascular vulnerability [27]. The HRV can be quantified using both time-domain and frequency-domain measures. In the time domain, commonly used indices include the standard deviation of normal-to-normal intervals, which reflects overall variability, and the root mean square of successive differences, which captures short-term vagal modulation. In the frequency domain, spectral analysis of RR intervals decomposes variability into distinct components: the high-frequency (HF) band (0.15–0.4 Hz), which reflects parasympathetic activity and encompasses RSA, and the low-frequency (LF) band (0.04-0.15 Hz), which represents a combination of sympathetic and parasympathetic influences. These classical HRV measures form the basis for assessing autonomic function in both clinical and experimental studies, including those presented in Paper IV. However, it should be emphasized that in arrhythmic conditions such as AF, conventional interpretation of HRV metrics are not applicable, since ventricular rhythm is irregular and not initiated by the sinus node.

#### 2.4 Atrial Fibrillation

Atrial fibrillation currently affects an estimated 30 to 46 million individuals world-wide, with projections indicating that this number could double by 2050 due to population aging and improved detection methods [28]. AF is characterized by rapid, disorganized electrical activity in the atria, leading to ineffective atrial contraction and an irregular ventricular response. Clinically, this arrhythmia can manifest as palpitations, fatigue, dyspnea, or may remain entirely asymptomatic. Despite variable presentation, AF is strongly associated with an increased risk of stroke, heart failure, and all-cause mortality [29].

According to the 2024 ESC Guidelines [1], AF should be classified using a combination of temporal pattern and additional descriptors:

- *First-diagnosed AF*: AF that has not previously been documented, regardless of symptom status, temporal pattern, or duration.
- *Paroxysmal AF*: AF that terminates within 7 days, either spontaneously or with intervention. Most self-terminating episodes last less than 48 hours.
- *Persistent AF*: AF that does not terminate spontaneously, with many clinical studies using 7 days as a practical cut-off.
- *Long-standing persistent AF*: Continuous AF lasting  $\geq$ 12 months.
- *Permanent AF*: AF in which no further attempts will be made to restore sinus rhythm, following shared decision-making between patient and physician.

In addition to these categories, the 2024 ESC Guidelines emphasize complementary descriptors that provide further clinical context. These include *AF burden* (the proportion of time spent in AF during monitoring), *recent-onset AF*, *trigger-induced AF* (AF occurring in proximity to a reversible precipitating factor), and *early AF* (defined as 3–24 months from first diagnosis). Moreover, the guidelines highlight the distinction between *self-terminating* and *non-self-terminating* AF, which may have implications for rhythm-control strategies. These classifications are based on observed temporal patterns and clinical context rather than underlying mechanisms, and reclassification may be required as the disease evolves. AF progression is common, with many patients transitioning from paroxysmal to more sustained forms over time. Symptoms of AF vary widely and may include palpitations, fatigue, and shortness of breath; however, many patients remain asymptomatic [1].

#### 2.4.1 AF mechanisms

Atrial fibrillation is typically triggered by ectopic electrical activity, most frequently originating from the pulmonary veins, especially the left superior pulmonary vein. However, a trigger alone is not sufficient. For AF to persist, a permissive atrial substrate must be present, shaped by remodeling processes and electrophysiological heterogeneity [30]. The development and maintenance of AF involve a complex interplay of four key pathophysiological mechanisms: electrical remodeling, structural remodeling, autonomic nervous system alterations, and intracellular calcium handling abnormalities [28].

Electrical remodeling includes the down-regulation of the L-type calcium current ( $I_{Ca}$ ), up-regulation of background potassium currents such as the inward rectifier current ( $I_{K1}$ ), and enhancement of the acetylcholine-activated potassium current. As described in Sec.2.2.1 and illustrated in Fig.2.3, these ionic changes lead to shortened action potential duration (APD), reduced refractoriness, and disrupted conduction, all of which promote reentrant arrhythmias [31]. Altered gap junction coupling may further contribute to conduction heterogeneity [32].

Structural remodeling encompasses atrial enlargement and fibrosis, both of which contribute to slowed conduction and the formation of reentrant circuits. Fibrosis in particular creates regions of conduction block and anisotropy, increasing the likelihood of wavebreaks. These structural changes are often driven by underlying conditions such as hypertension, heart failure, or the presence of AF itself, supporting the concept that "AF begets AF" [32, 33].

The role of ANS in AF has been recognized for decades. Early work by Coumel [34] implicated autonomic imbalance in paroxysmal AF, and subsequent studies, including HRV analysis [35] and direct nerve recordings in canine models [36, 37], demonstrated that simultaneous sympathetic and parasympathetic activation may precede AF onset. Mechanistically, both autonomic branches can shorten atrial refractory periods and promote triggered activity, while autonomic hyperinnervation, particularly in atrial tissue, has been linked to spontaneous ectopic discharges and AF initiation. These influences remain clinically relevant in permanent AF, where rate control strategies act partly by modulating ANS tone [38, 39].

Calcium handling abnormalities further contribute to the initiation and maintenance of AF. Defective regulation of intracellular Ca<sup>2+</sup> leads to spontaneous sarcoplasmic reticulum calcium release events, which in turn activate the sodium–calcium exchanger. The resulting transient inward current can cause delayed afterdepolarizations, thereby

triggering ectopic atrial activity [40]. In addition, impaired calcium reuptake and altered ryanodine receptor function promote intracellular Ca<sup>2+</sup> overload and electrical instability, further facilitating abnormal impulse formation and arrhythmogenic conduction [41].

## 2.4.2 AF management

The management of AF typically involves a combination of anticoagulation therapy and one of two core strategies: *rate control* or *rhythm control*. While anticoagulants are prescribed to mitigate the elevated risk of thromboembolic events, especially stroke, the choice between rate and rhythm control depends on patient-specific factors, symptom burden, and disease progression [42].

Rate control aims to regulate the ventricular response by slowing the heart rate without necessarily restoring sinus rhythm. This approach is often preferred as a first-line strategy, particularly in older or minimally symptomatic patients [42]. Pharmacological agents such as beta-blockers and calcium channel blockers are commonly used to decrease AV nodal conduction, thereby reducing the number of atrial impulses that reach the ventricles. The target resting heart rate is typically set below 80 beats per minute [43].

Rhythm control focuses on restoring and maintaining sinus rhythm and may be considered in patients who remain symptomatic despite adequate rate control or in those with early-stage AF to prevent disease progression [1]. Cardioversion, either pharmacologic or electrical, can be used to restore sinus rhythm, and antiarrhythmic drugs may be prescribed to prevent recurrence [1]. In patients with symptomatic AF who fail or are intolerant to antiarrhythmic drug therapy, catheter ablation may be offered as a rhythm control strategy. The primary purpose of ablation is to electrically isolate the pulmonary veins, which are common sources of AF triggers, thereby reducing arrhythmia recurrence. Ablation is particularly effective in patients with paroxysmal AF and less so in advanced or long-standing forms, where structural remodeling limits efficacy [44, 45].

Chapter 3

# ECG Based Analysis of Atrial Fibrillation

#### 3.1 ECG in AF

The surface ECG shows AF in characteristic ways that are used for both clinical identification and quantitative analysis. The most typical features are the absence of organized P-waves, reflecting the loss of coordinated atrial depolarization; the presence of rapid, low-amplitude oscillations known as fibrillatory waves (*f-waves*); and an "irregularly irregular" ventricular response, which produces beat-to-beat variability in RR intervals due to unpredictable AV conduction.

These features are illustrated in Figure 3.1, which shows a representative ECG segment from a patient with persistent AF. Among the standard 12 leads, lead V1 is often most informative for atrial activity, as its anatomical orientation enhances the visibility of f-waves [46]. In contrast, limb leads typically display lower-amplitude fibrillatory activity and more prominent ventricular complexes. While these characteristics are sufficient for visual diagnosis of AF, quantitative analysis requires the isolation of atrial activity from the dominating ventricular complexes. This motivates the development of dedicated methods for *f-wave extraction*, which are described in the following section.

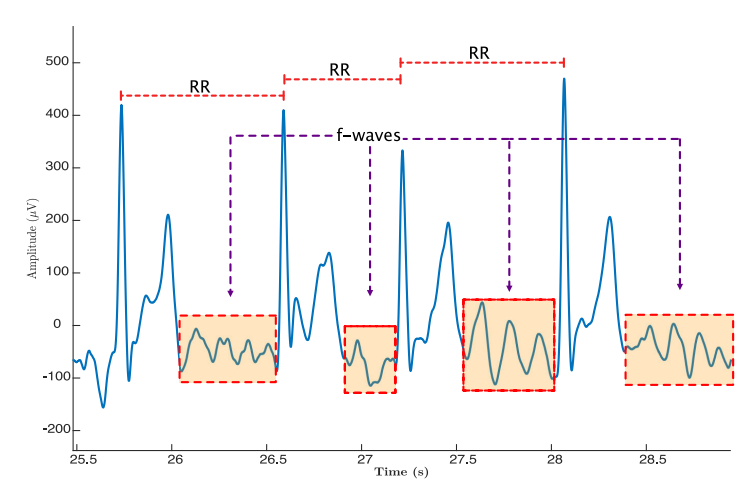


Figure 3.1: Example of ECG recording during AF.

#### 3.2 Extraction of f-waves

The extraction of f-waves from surface ECG recordings during AF plays a central role in the quantitative analysis and characterization of atrial activity. Historically, clinical interpretation of f-waves was limited to descriptive assessments, such as distinguishing between "coarse" and "fine" fibrillatory activity. However, a turning point occurred in the late 1990s when two pivotal studies [47, 48] demonstrated that spectral analysis of f-waves could provide meaningful insights into atrial refractoriness and predict pharmacological cardioversion outcomes. These findings emphasized the need for robust signal processing techniques capable of isolating f-waves from the dominating ventricular activity. In this context, the term f-wave extraction refers specifically to the removal of ventricular components, primarily the QRST complex, from the ECG to isolate atrial activity.

Designing an effective f-wave extraction method involves numerous considerations, including the number of leads available, signal duration, presence of noise and artifacts, and the occurrence of ectopic beats like ventricular premature beats (VPBs). While early methods operated on individual leads, it soon became evident that multilead analysis provides significant advantages, particularly through the use of signal separation techniques that exploit the distinct spatial origins of atrial and ventricular signals. Respiratory modulation, short recordings (e.g., 10-second ECGs), and VPBs present additional technical challenges that must be carefully addressed to avoid residual artifacts or distortions in the extracted atrial signal. Given these complexities, a

wide variety of methods have been developed to tackle f-wave extraction, each with its own strengths, assumptions, and limitations. These methods range from ensemble-based subtraction techniques to adaptive and statistical filtering approaches. In the following sections, several prominent extraction methods are briefly explained, beginning with average beat subtraction and progressing toward more advanced strategies such as adaptive filtering, principal component analysis, and independent component analysis.

## 3.2.1 Average Beat Subtraction (ABS)

Average Beat Subtraction (ABS) is one of the most well-established techniques for extracting f-waves from individual ECG leads. Initially developed for detecting atrioventricular dissociation during ventricular tachycardia, it has been widely adopted for processing AF signals due to its conceptual simplicity and clinical applicability [49, 50].

The core principle of ABS is to treat the ECG signal as a combination of two components: the ventricular activity (QRST complex) and a residual signal, which includes both the atrial activity (f-waves) and extracardiac noise. Mathematically, each beat segment  $x_i(n)$  of the ECG signal is modeled as:

$$x_i(n) = s(n) + z_i(n), \quad i = 1, \dots, M, \quad n = 0, \dots, N - 1,$$
 (3.1)

where s(n) represents the underlying QRST complex assumed common across beats, and  $z_i(n)$  is the residual component composed of the atrial signal  $d_i(n)$  and noise  $v_i(n)$ :

$$z_i(n) = d_i(n) + v_i(n).$$
 (3.2)

Here, M is the number of beats in the ensemble, and N is the number of samples in each beat. In its simplest form, ABS uses ensemble averaging to estimate the ventricular template  $\hat{s}(n)$ :

$$\hat{s}(n) = \frac{1}{M} \sum_{i=1}^{M} x_i(n). \tag{3.3}$$

The f-wave estimate for beat i is then obtained by subtracting the average QRST template:

$$\hat{d}_i(n) = x_i(n) - \hat{s}(n).$$
 (3.4)

This method assumes that ventricular activity is relatively invariant across beats, while atrial activity and noise are uncorrelated and randomly distributed. When this assumption holds, the averaging process attenuates non-repetitive components (e.g.,

f-waves), leaving behind a reliable QRST estimate.

However, ABS faces challenges in practice. Beat-to-beat variations in QRST morphology, caused by respiration, noise, or ectopic activity, can degrade the accuracy of the average template. To address this, morphology-specific averaging can be performed, where beats are first clustered based on shape before averaging. The accuracy of subtraction tends to be higher near the QRS complex, with increasing variance towards the boundaries of the cardiac cycle, since fewer samples are aligned for averaging. To address slow changes in QRST morphology over time, an exponential averaging approach can be used [51]:

$$\hat{s}_i(n) = \hat{s}_{i-1}(n) + \alpha(x_i(n) - \hat{s}_{i-1}(n)), \quad 0 < \alpha < 1, \tag{3.5}$$

where the weighting factor  $\alpha$  controls the adaptability of the template. This recursive formulation enables gradual tracking of morphological drift, which is common in long recordings. Despite its simplicity and limitations, ABS remains a foundational method for QRST cancellation and f-wave extraction. It often serves as a baseline against which more advanced techniques, such as ICA and adaptive filtering, are compared.

## 3.2.2 Adaptive Filtering

Adaptive filtering is one of the established approaches for extracting f-waves, where the QRST complex is dynamically estimated and subtracted from the ECG [52]. Unlike template-based methods that rely on averaging, adaptive filters continuously update their estimate of the ventricular activity in real-time, allowing the system to adapt to changes in QRS morphology caused by respiration, noise, or ectopic beats. In the context of f-wave extraction, adaptive filtering typically operates using a reference signal that is highly correlated with the QRST complex but uncorrelated with the atrial activity [53]. This reference may be derived from another lead in a multichannel ECG or generated by combining multiple leads using spatial filtering techniques. The most common implementation involves the least mean squares (LMS) algorithm, which iteratively adjusts filter coefficients to minimize the error between the primary signal and the estimated ventricular component.

Let x(n) represent the primary ECG signal containing both atrial and ventricular activity, and let r(n) be the reference signal. The adaptive filter generates an estimate  $\hat{s}(n)$  of the ventricular activity using a linear filter:

$$\hat{s}(n) = \sum_{k=0}^{L-1} w_k(n) r(n-k), \tag{3.6}$$

where  $w_k(n)$  are the time-varying filter coefficients and L is the filter length. The f-wave signal is then obtained as the residual:

$$\hat{d}(n) = x(n) - \hat{s}(n). \tag{3.7}$$

The coefficients are updated recursively using the LMS rule:

$$w_k(n+1) = w_k(n) + \mu \cdot e(n) \cdot r(n-k),$$
 (3.8)

where  $\mu$  is the step-size parameter and  $e(n)=x(n)-\hat{s}(n)$  is the estimation error. Adaptive filtering offers several advantages, including the ability to track slow variations in ventricular morphology and to operate in real-time. It is particularly useful in long-duration recordings where beat-to-beat variability may be substantial. However, its performance heavily depends on the availability of a clean and informative reference signal. If the reference signal contains significant atrial content or is poorly correlated with the ventricular activity in the primary signal, the subtraction may be incomplete or introduce artifacts. Despite this limitation, adaptive filtering remains a valuable tool for f-wave extraction, especially when combined with multilead recordings or in conjunction with other preprocessing techniques that enhance reference signal quality.

## 3.2.3 Principal Component Analysis (PCA)

Principal Component Analysis (PCA) is a statistical technique used for dimensionality reduction and signal separation, which has been effectively applied to the extraction of f-waves in multilead ECG recordings. The method exploits the fact that ventricular activity typically dominates the surface ECG and is highly correlated across leads, while atrial activity tends to be spatially more diverse and contributes less variance [54]. PCA transforms the multilead ECG data into a new set of orthogonal components, principal components, ranked by the amount of variance they explain in the signal. The first few components generally capture most of the QRST-related variance, while later components retain information with lower energy, such as the f-waves and noise.

Let the multilead ECG signal be represented by a matrix  $\mathbf{X} \in \mathbb{R}^{N \times L}$ , where each column corresponds to one of the L leads and each row to a time sample. PCA computes the covariance matrix:

$$\mathbf{C} = \frac{1}{N-1} \mathbf{X}^{\mathsf{T}} \mathbf{X},\tag{3.9}$$

and performs eigenvalue decomposition:

$$\mathbf{C} = \mathbf{U}\boldsymbol{\Lambda}\mathbf{U}^{\top},\tag{3.10}$$

where  ${\bf U}$  contains the eigenvectors (principal components) and  ${\bf \Lambda}$  is a diagonal matrix of eigenvalues. To remove the ventricular component, only the first K principal components corresponding to the largest eigenvalues are retained and used to reconstruct the QRST activity:

$$\hat{\mathbf{S}} = \mathbf{X} \mathbf{U}_K \mathbf{U}_K^{\top},\tag{3.11}$$

where  $\mathbf{U}_K$  contains the first K columns of  $\mathbf{U}$ . The estimated f-wave signal is then obtained as:

$$\hat{\mathbf{D}} = \mathbf{X} - \hat{\mathbf{S}}.\tag{3.12}$$

PCA is especially useful when a sufficient number of leads (e.g., 8–12) are available, and when beat morphology is relatively consistent across the recording. It is fully data-driven and does not require explicit beat detection or QRST alignment, which can be advantageous in noisy or artifact-prone signals. However, PCA is limited by its assumption of orthogonal sources and its reliance on energy dominance for signal separation. If the f-waves or noise dominate some leads, they may be inadvertently included in the leading components and removed during subtraction.

## 3.2.4 Independent Component Analysis (ICA)

Independent Component Analysis (ICA) is a blind source separation technique that extends the concept of principal component analysis (PCA) by aiming to recover statistically independent, rather than merely uncorrelated, components. In the context of AF, ICA models the multilead ECG as a linear mixture of physiologically distinct sources, including ventricular activity, atrial activity (f-waves), and background noise. The central assumption is that atrial and ventricular signals originate from independent electrophysiological processes, which can therefore be separated by maximizing the non-Gaussianity of the extracted components. This enables isolation of components corresponding to QRST complexes and f-waves without requiring explicit prior knowledge of their morphology.

Different ICA implementations have been proposed for atrial activity extraction. Rieta et al. [55] applied the FastICA algorithm, identifying the atrial component by its sub-Gaussian distribution (low kurtosis) and the presence of a dominant spectral peak in the AF frequency range. Castells et al. [56], on the other hand, introduced a maximum-likelihood ICA approach that explicitly incorporates prior assumptions about the source distributions (super-Gaussian for ventricular activity and sub-Gaussian for atrial activity). Both approaches exploit the same underlying independence assumption and linear mixing model, but they differ in their degree of reliance on prior statistical models: FastICA is data-driven with minimal assumptions,

whereas maximum-likelihood ICA leverages predefined source distributions to potentially improve separation and allow quantitative evaluation in simulations.

Let the multilead ECG signal be represented by a data matrix  $\mathbf{X} \in \mathbb{R}^{N \times L}$ , where N is the number of samples and L the number of leads. The observed signals are modeled as a linear mixture:

$$\mathbf{X} = \mathbf{AS},\tag{3.13}$$

where **A** is an unknown mixing matrix and **S** contains the independent source signals. ICA estimates an unmixing matrix **W** such that:

$$\hat{\mathbf{S}} = \mathbf{W}\mathbf{X},\tag{3.14}$$

where  $\hat{\mathbf{S}}$  contains the statistically independent components. Among these components, those representing QRST activity are identified based on their temporal morphology and amplitude. To reconstruct their contribution in the original signal space, the corresponding columns of the mixing matrix  $\mathbf{A}$  are needed. These can be estimated as the pseudo-inverse of the unmixing transformation, i.e.  $\mathbf{A} \approx \mathbf{W}^{-1}$ , after which the QRST-related submatrix  $\mathbf{A}_{\text{QRST}}$  is obtained by retaining only the columns associated with ventricular components. The ventricular contribution is then reconstructed as  $\hat{\mathbf{S}}_{\text{QRST}} \cdot \mathbf{A}_{\text{QRST}}$  and subtracted from the raw ECG to isolate the atrial signal:

$$\hat{\mathbf{D}} = \mathbf{X} - \hat{\mathbf{S}}_{QRST} \mathbf{A}_{QRST}. \tag{3.15}$$

ICA has proven highly effective in multilead recordings where the number of leads exceeds the number of underlying sources. It does not require beat detection, QRST alignment, or template averaging, making it suitable for continuous, unsegmented ECG analysis. Moreover, ICA is robust to overlapping atrial and ventricular activity due to its statistical formulation.

However, ICA has limitations. Its success depends on the validity of the independence assumption and the number of available leads. In underdetermined systems (fewer leads than sources), ICA cannot uniquely resolve all components. Additionally, components extracted by ICA may not be easily interpretable without post-processing or validation.

## 3.2.5 Spatiotemporal QRST Cancellation

The f-wave extraction in this thesis was performed using the *spatiotemporal QRST* cancellation method developed by Stridh and Sörnmo [57]. This approach generalizes ABS by introducing both spatial and temporal alignment in order to compensate for

variations in QRS morphology that arise from respiration, electrode placement, and beat-to-beat variability. These factors frequently cause incomplete cancellation with simpler techniques, leaving ventricular residuals that obscure the atrial activity. In the spatiotemporal framework, each observed beat in the multilead ECG is modeled as the sum of atrial activity ( $\mathbf{Y}_A$ ), ventricular activity ( $\mathbf{Y}_V$ ), and additive noise ( $\mathbf{W}_0$ ):

$$\mathbf{Y} = \mathbf{Y}_A + \mathbf{Y}_V + \mathbf{W}_0. \tag{3.16}$$

The ventricular contribution is represented by an averaged beat template X that is aligned to the observed beat through a combination of temporal and spatial transformations. Temporal alignment is achieved with a shift matrix  $J_{\tau}$ , which corrects for small misalignments in QRS timing, while spatial alignment is performed with a transformation matrix S defined as

$$S = DQ, (3.17)$$

where  ${\bf D}$  is a diagonal amplitude-scaling matrix and  ${\bf Q}$  is a rotation matrix. The ventricular activity is therefore modeled as

$$\mathbf{Y}_{V} = \mathbf{J}_{\tau} \mathbf{X} \mathbf{S}. \tag{3.18}$$

The cancellation task consists of estimating the optimal parameters  $\mathbf{D}$ ,  $\mathbf{Q}$ , and  $\tau$  by minimizing the squared error between the observed beat and the aligned template:

$$\min_{\mathbf{D}, \mathbf{Q}, \tau} \|\mathbf{Y} - \mathbf{J}_{\tau} \mathbf{X} \mathbf{S}\|_F^2, \tag{3.19}$$

where  $\|\cdot\|_F$  denotes the Frobenius norm. Because the presence of f-waves may bias parameter estimation, an intermediate estimate of the atrial activity is first constructed from adjacent TQ intervals and subtracted, yielding a residual signal **Z** with reduced atrial content. The optimization is then performed on **Z**, after which the final cancellation is applied to the original signal. This iterative procedure converges rapidly and provides robust estimates of the alignment parameters.

The spatiotemporal method has been shown to reduce QRS-related residuals by nearly 40% compared to ABS, with the largest improvements during the QRS complex itself [57]. This performance advantage is particularly important for spectral and time–frequency analysis of f-waves, where contamination from ventricular activity can bias frequency estimation or obscure autonomic modulations. The main limitations of the method are its dependence on multilead ECGs, increased computational complexity relative to ABS, and a tendency for residuals to remain during the T wave when its morphology varies substantially. Nonetheless, these drawbacks are outweighed by the

significant improvements in cancellation accuracy. For these reasons, the spatiotemporal QRST cancellation method was selected for all studies in this thesis. Its ability to exploit multilead information and adapt to beat-to-beat variations ensured a more faithful isolation of atrial activity, which was essential for investigating autonomic modulation, respiratory influences, and methodological extensions of f-wave analysis.

#### 3.3 Characterization of f-waves

Once the ventricular activity has been effectively removed, the residual signal primarily reflects atrial activity, which can be analyzed using a variety of signal processing techniques. Commonly used descriptors include time-domain metrics such as amplitude, frequency-domain parameters like atrial fibrillatory rate (AFR), and measures of signal complexity or regularity. These features provide different views of how the atria behave during AF and are useful for both clinical assessment and AF monitoring [58, 59].

## 3.3.1 Amplitude

One of the earliest and most intuitive features used to characterize f-waves is their amplitude. Historically, f-waves were classified as either "coarse" (≥0.1 mV) or "fine" (<0.1 mV) based on visual inspection, with this categorization typically performed in leads II and V1 [60, 61]. Coarse f-waves are generally associated with more organized atrial activity, while fine f-waves are typically associated with increased atrial remodeling, fibrosis, and a more disorganized substrate [62].

Several methods have been proposed for quantifying f-wave amplitude. It can be measured directly from the f-wave signal, for example by averaging the largest peak-to-peak values in a 10-s recording, or by computing the root-mean-square value of the f-wave signal samples, which reflects the average signal amplitude over time. An alternative technique involves envelope detection based on local extrema. In this method, the amplitude estimate  $\hat{a}$  is calculated from  $N_x$  samples of the f-wave signal x(n) as:

$$\hat{a} = \frac{1}{N_x} \sum_{n=0}^{N_x - 1} |x_{\text{max}}(n) - x_{\text{min}}(n)|, \tag{3.20}$$

where  $x_{\text{max}}(n)$  and  $x_{\text{min}}(n)$  represent interpolated local maxima and minima, respectively, typically derived using piecewise cubic Hermite interpolation [63].

However, accurate amplitude estimation can be confounded by residual ventricular activity that remains after QRST cancellation. Even small QRS-related residuals may distort the atrial signal and artificially increase the estimated amplitude. To address this, some studies restrict the analysis to carefully selected QRS-free segments of the ECG, while others apply alternative definitions such as averaging only the largest f-wave peaks within a segment [64, 65]. These strategies aim to minimize ventricular contamination and improve the robustness of amplitude estimates.

## 3.3.2 Atrial Fibrillatory Rate (AFR)

Atrial Fibrillatory Rate (AFR) is one of the most widely used and clinically informative features for quantifying atrial activity during atrial fibrillation. It reflects the average activation frequency of the atria and serves as an indirect indicator of atrial refractoriness [66]. AFR is most commonly estimated in the frequency domain following QRST cancellation, where it is defined as the frequency corresponding to the dominant peak of the power spectral density (PSD) of the f-wave signal. Welch's method is typically used for PSD estimation, as it reduces variance by averaging spectra from overlapping windowed segments. Specifically, if x(n) is divided into K overlapping segments  $x_k(n)$  of length M, each weighted by a window w(n), the periodogram of segment k is given by

$$P_k(f) = \frac{1}{MU} \left| \sum_{n=0}^{M-1} x_k(n) w(n) e^{-j2\pi f n} \right|^2, \tag{3.21}$$

where U is a normalization factor for window energy. The Welch estimate of the PSD is obtained by averaging across all segments:

$$\hat{P}(f) = \frac{1}{K} \sum_{k=1}^{K} P_k(f). \tag{3.22}$$

AFR is then identified as the dominant frequency  $f_{\rm AFR}$  within the physiological range of 3–10 Hz (commonly 4–9 Hz) [67]. Figure 3.2 illustrates an example of an extracted f-wave signal and its corresponding Welch spectrum, with the AFR marked at 4.9 Hz. Lead V1 is often favored for AFR estimation due to its prominent atrial signal content, although multilead averaging can improve robustness by mitigating localized noise or electrode variability [68].

Clinically, AFR has proven valuable for stratifying AF severity and predicting treatment outcomes. Higher AFR values are associated with more disorganized atrial activity, long-standing persistent AF, and lower success rates of cardioversion [69]. In

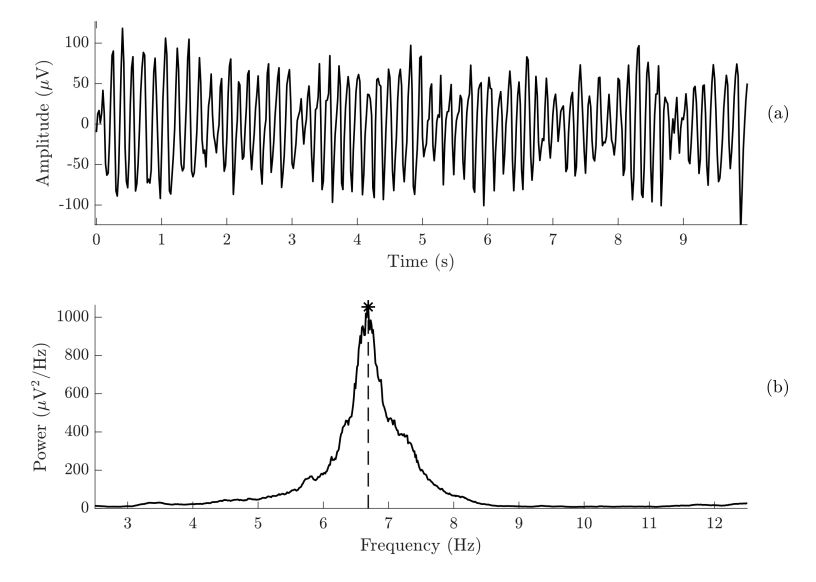


**Figure 3.2:** Example of (a) an extracted f-wave signal and (b) its corresponding power spectrum estimated with Welch's method. The AFR at 6.7 Hz, is indicated by a star.

contrast, lower AFR values are typically observed in paroxysmal AF and may reflect a more organized and reversible atrial substrate [69]. Nevertheless, AFR estimation remains sensitive to imperfect QRST cancellation and residual noise, making careful preprocessing and lead selection essential for reliable results.

## 3.3.3 Time-Varying AFR Analysis

Beyond static estimation, AFR can vary considerably over short time scales, reflecting the dynamic nature of atrial activation. Tracking these variations provides additional insight into AF mechanisms and their modulation by interventions, vagal activity, or spontaneous rhythm changes [70]. A range of time–frequency and adaptive methods have been developed for this purpose.

## Short-Time Fourier Transform (STFT)

The simplest approach is the short-time Fourier transform (STFT), in which the f-wave signal x(n) is multiplied by a sliding analysis window w(n) and transformed to yield

$$X(n,\omega) = \sum_{l=-\infty}^{\infty} x(l)w(l-n)e^{-j\omega l}.$$
 (3.23)

The squared magnitude  $S_x(n,\omega) = |X(n,\omega)|^2$  produces a spectrogram that reveals the temporal evolution of the dominant frequency. STFT is easy to implement and widely used, but it suffers from a fundamental trade-off: short windows yield good time resolution but poor frequency resolution, and vice versa [71].

#### Wigner-Ville and Cross Wigner-Ville Distributions

Quadratic time–frequency methods, such as the Wigner–Ville distribution (WVD), provide higher joint time–frequency resolution compared to linear approaches like STFT [72, 73]. For a signal x(n), the discrete-time WVD is defined as

$$W_x(n,\omega) = \sum_{m=-\infty}^{\infty} x\left(n + \frac{m}{2}\right) x^*\left(n - \frac{m}{2}\right) e^{-j\omega m},\tag{3.24}$$

where  $x^*(\cdot)$  denotes the complex conjugate of  $x(\cdot)$ . The WVD produces a time–frequency distribution that is highly concentrated around the instantaneous frequency of the signal. This makes it attractive for tracking rapid AFR changes that may be missed by STFT due to its resolution trade-off.

However, the quadratic formulation introduces cross-terms when multiple components are present, such as harmonics of the fibrillatory frequency or residual ventricular activity. These cross-terms appear as spurious oscillatory structures in the time-frequency plane and complicate interpretation in real ECG signals with low SNR. The cross Wigner–Ville distribution (XWVD) reduces these artifacts by computing the distribution between the signal of interest x(n) and a reference sinusoid y(n), typically based on an initial STFT estimate of the dominant frequency  $\omega_0(n)$  [70]. Iterative refinement is then performed:

$$W_{x,y}(n,\omega) = \sum_{m=-\infty}^{\infty} x\left(n + \frac{m}{2}\right) y^*\left(n - \frac{m}{2}\right) e^{-j\omega m}.$$
 (3.25)

The updated dominant frequency  $\hat{\omega}_0(n)$  is extracted from  $W_{x,y}(n,\omega)$  and used to construct a new reference signal, iterating until convergence. This iterative XWVD framework allows smoother tracking of AFR dynamics [70]. The main advantages of WVD/XWVD are their high joint time–frequency resolution and ability to reveal rapid AFR fluctuations. Their limitations are sensitivity to noise, computational cost, and the persistence of cross-term artifacts, especially when multiple atrial wavelets contribute to the signal.

#### **Spectral Profile Method**

The spectral profile method was developed to overcome the smearing and harmonic distortion often observed in STFT- or WVD-based analyses. Instead of treating each time segment independently, this method aligns and averages spectra from consecutive segments on a logarithmic frequency scale, thereby enhancing harmonic structure and suppressing noise [74]. Given a segment  $x_p(n)$  with N samples, the nonuniform discrete-time Fourier transform is computed as

$$q_p(\nu_\ell) = \sum_{n=0}^{N-1} x_p(n)w(n)e^{-j\nu_\ell n}, \quad \ell = 0, \dots, L-1,$$
 (3.26)

where w(n) is a window function and  $\nu_\ell$  are logarithmically spaced frequencies defined by

$$\nu_{\ell} = \nu_{\text{low}} \pi^{\frac{\eta \ell}{L}}, \quad \ell = 0, \dots, L - 1.$$
 (3.27)

Here,  $\nu_{\rm low}$  is the lowest frequency of interest (in normalized digital frequency),  $\eta$  determines the spacing factor, and L is the number of frequency bins. The corresponding upper frequency is given by  $\nu_{\rm high} = \nu_{\rm low} \pi^{\eta}$ .

The resulting spectra  $|q_p(\nu_\ell)|$  are shifted and scaled to align their dominant peaks, after which an exponentially weighted average is performed to update the spectral profile  $\hat{\phi}_p$ :

$$\hat{\phi}_{p+1} = (1 - \alpha_p)\hat{\phi}_p + \alpha_p J_{-\hat{\theta}_p} \frac{|q_p|}{\|J_{-\hat{\theta}_p}|q_p|\|}, \tag{3.28}$$

where  $J_{-\hat{\theta}_p}$  is a shift operator aligning the first harmonic to a fixed reference position, and  $\alpha_p$  is a forgetting factor controlling update speed.

The main advantage of this method is a much cleaner harmonic representation compared to Welch's method or the spectrogram, enabling reliable tracking of the harmonic structure even in noisy signals. Importantly, while the spectral profile itself is aligned to a reference, the AFR is obtained from the sequence of alignment shifts  $\hat{\theta}_p$ . Specifically, the frequency of the first harmonic in the p-th segment is estimated as

$$\hat{\omega}_{0,p} = \hat{\omega}_{0,0} - \hat{\theta}_p, \tag{3.29}$$

where  $\hat{\omega}_{0,0}$  is the initialization point of the spectral profile. Thus, the profile provides robustness to noise and spectral leakage, while the shift estimates yield accurate AFR tracking. The limitations of the spectral profile method are its higher computational complexity, its dependence on accurate alignment, and the fact that it has seen limited use in large-scale clinical studies compared to simpler approaches.

#### **Adaptive Frequency Tracking**

An alternative is adaptive line enhancement, which models the analytic representation of the signal as

$$x(n) = A_0 e^{j\omega_0 n} + v(n), (3.30)$$

where  $A_0$  and  $\omega_0$  denote the amplitude and fundamental frequency, respectively, and v(n) is additive noise. Although the measured signal is real-valued, its complex-valued analytic representation, obtained using the Hilbert transform, is employed here, since this formulation simplifies the estimation of instantaneous frequency while remaining fully applicable to real signals [75, 76].

A time-varying first-order bandpass filter H(z;n) with complex coefficients is then applied to enhance the sinusoidal component:

$$H(z;n) = \frac{1 - \beta}{1 - \beta e^{j\omega(n)} z^{-1}},$$
(3.31)

where  $\omega(n)$  is the time-varying center frequency and  $0<\beta<1$  controls the bandwidth. The filter has unit gain and zero phase delay at  $\omega(n)$ , ensuring that the harmonic component is preserved without distortion. The center frequency  $\omega(n)$  is adapted on a sample-by-sample basis using a recursive error-minimization approach. Specifically, the filter output y(n) is assumed to satisfy the discrete oscillator relation

$$y(n) \approx e^{j\omega(n+1)}y(n-1). \tag{3.32}$$

The instantaneous frequency  $\omega(n)$  is then estimated by minimizing the mean square error

$$J(n) = E\{|y(n) - e^{j\omega(n+1)}y(n-1)|^2\}.$$
 (3.33)

This leads to the recursive definition

$$Q(n) = Q(n-1) + \alpha (y(n)y^*(n-1) - Q(n-1)), \qquad (3.34)$$

$$\hat{\omega}_0(n+1) = \arg(Q(n)),\tag{3.35}$$

where  $\alpha$  is a smoothing factor  $(0 < \alpha < 1)$ . Here, Q(n) represents the exponentially smoothed correlation between consecutive filter outputs, i.e., a running average of  $y(n)y^*(n-1)$ . The phase angle of Q(n) provides a robust estimate of the instantaneous frequency  $\hat{\omega}_0(n)$ . The recursion is typically initialized with Q(0) = 0, although in practice one may also use  $Q(0) = y(1)y^*(0)$  to accelerate convergence. Since exponential averaging ensures rapid convergence, the specific choice of initialization has little influence on long-term tracking performance [52]. This adaptive mechanism allows the filter to track slow variations in  $\omega_0$  while suppressing noise, thereby enabling robust frequency tracking [75, 76].

## 3.3.4 Complexity and Regularity

Beyond amplitude- and frequency-based measures, the complexity and regularity of f-waves offer additional insight into the organization of atrial activity during AF [77]. These nonlinear measures quantify the unpredictability or irregularity of a time series, with higher values indicating greater disorder. In the context of f-waves, increased entropy values typically correspond to more chaotic and fragmented atrial activation, which may reflect advanced structural remodeling or persistent AF [78, 79]. Several entropy-based measures have been proposed:

• Shannon entropy and spectral entropy: Shannon entropy is a classical measure of uncertainty for a discrete probability distribution  $p_i$ :

$$H = -\sum_{i=1}^{M} p_i \log p_i. {(3.36)}$$

In f-wave analysis, two domains are typically considered:

- Time domain:  $p_i$  represents the normalized probability of occurrence of amplitude levels within the f-wave segment, usually estimated from a histogram of the signal. Higher values indicate more irregular atrial activity, whereas lower values correspond to more organized activity [80].
- Frequency domain (spectral entropy): Shannon entropy applied to the normalized power spectrum  $P(f_k)$ :

$$P(f_k) = \frac{S_x(f_k)}{\sum_{j=1}^L S_x(f_j)}, \quad H_s = -\sum_{k=1}^L P(f_k) \log P(f_k), \quad (3.37)$$

where  $S_x(f_k)$  is the spectral power at frequency  $f_k$ . A narrowband spectrum (organized activity) yields low entropy, while a broadband spectrum (disorganized activity) yields high entropy [81].

• **Approximate entropy (ApEn):** Quantifies the likelihood that similar sequences of length m remain similar when extended to m+1 points [82]. Given a time series  $\{x(1),\ldots,x(N)\}$ , vectors of length m are formed as

$$X_m(i) = [x(i), x(i+1), \dots, x(i+m-1)], \quad 1 \le i \le N-m+1$$
 (3.38)

For each  $X_m(i)$ , the fraction of neighboring vectors  $X_m(j)$  within distance r is

$$B_i^m(r) = \frac{1}{N - m + 1} \# \{ j : d[X_m(i), X_m(j)] \le r \}, \tag{3.39}$$

where  $d[\cdot]$  is the maximum absolute difference between corresponding elements. The average logarithmic probability of similarity is then

$$\Phi^{m}(r) = \frac{1}{N - m + 1} \sum_{i=1}^{N - m + 1} \log B_{i}^{m}(r), \tag{3.40}$$

Finally,

$$ApEn(m, r, N) = \Phi^{m}(r) - \Phi^{m+1}(r).$$
 (3.41)

Higher ApEn values indicate less predictable temporal dynamics. In AF research, ApEn has been widely used to quantify f-wave complexity in surface ECGs, providing insight into atrial organization [83]. However, studies confirmed that ApEn and related metrics are sensitive to signal irregularities and artifacts such as spikes, which is critical when analyzing atrial activity [84].

• Sample entropy (SampEn): A refinement of ApEn that reduces bias for short data segments by excluding self-matches [85]. Like ApEn, SampEn evaluates the conditional probability that sequences of length m which are similar within tolerance r remain similar at length m+1. If B and A denote the counts of matches of length m and m+1, respectively, then

$$SampEn(m, r, N) = -\ln \frac{A}{B}.$$
 (3.42)

By avoiding self-matches, SampEn provides a less biased and more consistent measure, particularly for shorter recordings. In AF analysis, SampEn has been applied to f-waves to quantify irregularity, and has even been shown to predict spontaneous AF termination after catheter ablation [83, 86].

These entropy-based measures are particularly useful for distinguishing between different AF types (e.g., paroxysmal vs. persistent) or for tracking changes in atrial dynamics over time. Several studies have demonstrated their value for patient characterization and clinical stratification [66, 80, 83].

# 3.4 Modelling of f-waves

While ECG signal databases, such as those available on PhysioNet [87], are essential for developing and evaluating analysis methods, simulated signals offer distinct advantages in controlled experimental settings. Simulated data allow precise control over signal characteristics through parameterization, making it possible to systematically

assess algorithm performance. This enables the use of quantitative metrics to compare estimated values against known ground truth. Furthermore, simulations can be generated under varying signal-to-noise ratios, facilitating robustness testing under realistic conditions.

A widely used model for simulating f-waves is the saw-tooth model, first introduced in [57] and subsequently applied in several studies for algorithm development and validation [88, 89]. In this model, the synthetic f-wave signal is constructed as the sum of K sinusoids with harmonically related amplitude and frequency modulation. The simulated signal  $x_{sim}(n)$  is defined as:

$$x_{sim}(n) = \sum_{k=1}^{K} a_k(n) \sin\left(2\pi k f_0 n + k \frac{\triangle F}{F_m} \sin(2\pi F_m n)\right), \qquad (3.43)$$

where  $f_0$  is the fundamental frequency (corresponding to the AFR),  $\triangle F$  and  $F_m$  define the maximum frequency deviation and modulation frequency, respectively. The time-varying amplitude of the  $k^{\text{th}}$  harmonic is given by:

$$a_k(n) = \frac{2}{k\pi} \left( a + \triangle a \sin(2\pi F_a n) \right), \tag{3.44}$$

where a is the average amplitude, and  $\triangle a$  and  $F_a$  define the amplitude modulation depth and frequency, respectively.

In Paper I [90], we proposed an enhanced version of the saw-tooth model to enable more comprehensive performance evaluation. This modified model includes both respiratory-induced frequency modulation and random variability in the f-wave signal. The simulated waveform is constructed as:

$$x'_{sim}(n) = \sum_{k=1}^{K} a_k(n) \sin(2\pi k f(n)n), \qquad (3.45)$$

where the instantaneous frequency  $f(\boldsymbol{n})$  varies over time according to:

$$f(n) = \frac{f_0}{f_s} + \frac{\Delta f}{2\pi f_r n} \sin\left(2\pi n \frac{f_r}{f_s}\right) + \frac{\Phi(n)}{2\pi k n},\tag{3.46}$$

Here,  $f_r$  and  $\Delta f$  represent the frequency and magnitude of respiratory-induced modulation, respectively. The term  $\Phi(n)$  introduces random phase variation, modeled as white Gaussian noise with standard deviation  $\sigma_{\Phi}$ , to simulate stochastic fluctuations

in the f-wave signal.

Figure 3.3 shows several examples of the simulated f-wave signal  $x'_{sim}(n)$  for different levels of phase noise, illustrating how increasing  $\sigma_{\Phi}$  leads to increasingly irregular frequency content. This model enables flexible and realistic simulation of f-wave signals for robust validation of signal processing algorithms.

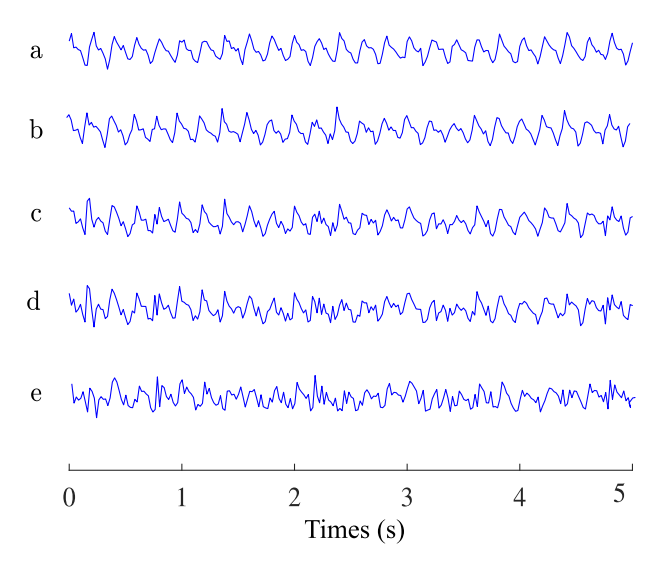


**Figure 3.3:** Example of the  $x'_{sim}(n)$  with K=2, f=5 Hz,  $f_r=0.2$  Hz,  $\Delta f=0.1$  Hz, and  $\sigma_{\Phi_a}$  = 0,  $\sigma_{\Phi_b}$  = 0.25,  $\sigma_{\Phi_c}$  = 0.5,  $\sigma_{\Phi_d}$  = 0.75,  $\sigma_{\Phi_e}$  = 1.

## 3.4.1 Model-based analysis of f-waves

Traditional time–frequency methods (see Sec. 3.3.3) provide valuable insight into AFR dynamics and harmonics, but they involve trade-offs between temporal and spectral resolution, robustness to noise, and interpretability. Adaptive trackers can offer high temporal precision but are often unstable under low-SNR conditions. To overcome these limitations, model-based approaches explicitly incorporate physiological and signal priors, enabling robust estimation of AFR trajectories even from short and noisy ECG segments. This motivates the use of model-based methods in Papers I–III.

Although the f-wave saw-tooth model has been widely used to simulate atrial fibrillatory signals, its relatively large number of parameters can make it impractical for direct parameter estimation. To address this limitation, a harmonic model for f-waves was introduced in [91] for estimating key signal components such as instantaneous frequency, amplitude, and phase. In this model, the f-wave signal is represented as a sum of complex exponentials with a fundamental angular frequency  $\omega_0$  and its harmonics:

$$s(n;\omega_0,\boldsymbol{\theta}) = \sum_{m=1}^{M} A_m e^{j(m\omega_0 n + \phi_m)}.$$
 (3.47)

where  $A_m$  and  $\phi_m$  are the amplitude and phase of the  $m^{\text{th}}$  harmonic, respectively. Hence, the full parameter vector describing the f-wave signal characteristics is given by  $\boldsymbol{\theta} = [A_1, \dots, A_M, \phi_1, \dots, \phi_M]^T$ . These parameters, along with the frequency  $\omega_0$ , are estimated using a maximum likelihood (ML) framework. The modeled signal of length N, denoted  $\boldsymbol{s}(\omega_0, \boldsymbol{\theta})$ , is given by

$$s(\omega_0, \boldsymbol{\theta}) = \boldsymbol{Z}(\omega_0)\boldsymbol{a}(\boldsymbol{\theta}), \tag{3.48}$$

where  $\boldsymbol{Z}(\omega_0)$  is an  $N \times M$  Vandermonde matrix containing the harmonic basis functions:

$$\mathbf{Z}(\omega_0) = \begin{bmatrix} 1 & 1 & \cdots & 1 \\ e^{j\omega_0 1} & e^{j2\omega_0 1} & \cdots & e^{jM\omega_0 1} \\ \vdots & \vdots & \ddots & \vdots \\ e^{j\omega_0(N-1)} & e^{j2\omega_0(N-1)} & \cdots & e^{jM\omega_0(N-1)} \end{bmatrix},$$
(3.49)

and  $oldsymbol{a}(oldsymbol{ heta})$  is an M imes 1 complex vector combining amplitude and phase:

$$\mathbf{a}(\mathbf{\theta}) = [A_1 e^{j\phi_1}, A_2 e^{j\phi_2}, \dots, A_M e^{j\phi_M}]^T.$$
(3.50)

The observed f-wave signal is represented in analytic form as  $x_a(n)$ , obtained by applying the Hilbert transform to the real-valued f-wave signal extracted from the ECG. This yields a complex-valued analytic signal in which negative frequency components are suppressed, thereby facilitating spectral modeling. The modeled signal  $s(n; \omega_0, \boldsymbol{\theta})$  represents the fitted harmonic expansion of  $x_a(n)$ , parameterized by the fundamental frequency  $\omega_0$ , harmonic amplitudes  $A_m$ , and phases  $\phi_m$ . An example of an extracted f-wave signal x(n) is shown in Fig. 3.4(a), with the corresponding fitted model s(n) in Fig. 3.4(b).

The relationship between the analytic observed signal and the harmonic model is expressed as

$$x_a(n) = s(n; \omega_0, \boldsymbol{\theta}) + e(n), \tag{3.51}$$

where e(n) denotes additive white complex Gaussian noise. Assuming a known noise variance  $\sigma^2$ , the likelihood function for  $x_a$  is given by [91]

$$p(x_a; \omega_0, \boldsymbol{\theta}) = \frac{1}{\pi^N \sigma^{2N}} \exp\left(-\frac{|x_a - \boldsymbol{Z}(\omega_0)\boldsymbol{a}(\boldsymbol{\theta})|^2}{\sigma^2}\right).$$
(3.52)

The corresponding log-likelihood function becomes:

$$\mathcal{L}(\omega_0, \boldsymbol{\theta}) = \ln p(x_a; \omega_0, \boldsymbol{\theta}) \propto -\frac{1}{\sigma^2} |x_a - \boldsymbol{Z}(\omega_0) \boldsymbol{a}(\boldsymbol{\theta})|^2.$$
 (3.53)

Direct joint ML estimation of  $\omega_0$  and  $\theta$  is computationally intensive due to the high dimensionality of the parameter space. In model-based spectral estimation, this is typically addressed by first obtaining the least-squares (LS) estimate of  $a(\theta)$  for a fixed  $\omega_0$ :

$$\hat{\boldsymbol{a}}(\boldsymbol{\theta}) = (\boldsymbol{Z}(\omega_0)^H \boldsymbol{Z}(\omega_0))^{-1} \boldsymbol{Z}(\omega_0)^H x_a, \tag{3.54}$$

Substituting this estimate into the log-likelihood function reduces it to a function of  $\omega_0$  alone:

$$\mathcal{L}(\omega_0) \propto -\frac{1}{\sigma^2} \left| x_a - \mathbf{Z}(\omega_0) (\mathbf{Z}(\omega_0)^H \mathbf{Z}(\omega_0))^{-1} \mathbf{Z}(\omega_0)^H x_a \right|^2, \tag{3.55}$$

Finally, the ML estimate of the fundamental frequency  $\omega_0$  is obtained by minimizing this expression:

$$\hat{\omega}_0 = \underset{\omega_{0,\min} < \omega_0 < \omega_{0,\max}}{\arg \min} \left\| x_a - \boldsymbol{Z}(\omega_0) (\boldsymbol{Z}(\omega_0)^H \ \boldsymbol{Z}(\omega_0))^{-1} \boldsymbol{Z}(\omega_0)^H \ x_a \right\|^2, \quad (3.56)$$

To estimate the fundamental frequency  $\omega_0$ , a grid search is performed over a predefined frequency range where atrial fibrillatory activity is typically observed, i.e., between 4 and 12 Hz. Since this estimate is computed over the entire segment of length N, it reflects a global frequency estimate for the full window. However, f-wave frequency can vary substantially over time, as discussed in Sec. 3.3.3. To account for such temporal variability, the analytic signal  $x_a$  is divided into K overlapping subsegments, denoted as  $x_{a_k}$ , where k=1,...,K. Each subsegment contains L samples, with L chosen to ensure that at least one f-wave cycle is present per segment. For each subsegment, a local frequency estimate  $\hat{\omega}_{0,k}$  is determined by minimizing the

least-squares error, but constrained to lie within a specified range  $\Delta\omega_0$  around the global frequency estimate  $\hat{\omega}_0$ :

$$\hat{\omega}_{0,k} = \underset{|\omega_{0,k} - \omega_0| < \Delta \omega_0}{\arg \min} \|x_{a_k} - \mathbf{Z}_L(\omega_{0,k})(\mathbf{Z}_L(\omega_{0,k})^H \ \mathbf{Z}_L(\omega_{0,k}))^{-1} \mathbf{Z}_L(\omega_{0,k})^H \ x_{a_k}\|^2,$$
(3.57)

Here,  $\Delta\omega_0$  sets the allowable range of deviation from the global frequency, and  $\mathbf{Z}_L(\omega_0)$  is the Vandermonde matrix computed for subsegment length L. The extracted f-wave frequency trend f(n) from such subsegment analysis is illustrated in Fig. 3.4(d).

The analytic representation of the f-wave signal is  $x_a(n)$ , while the modeled signal is denoted by s(n). The modeling error is defined as

$$\hat{e}(n) = x_a(n) - s(n; \hat{\omega}_0, \hat{\boldsymbol{\theta}}). \tag{3.58}$$

Based on this error, a signal quality index S is calculated as

$$S = 1 - \frac{\sigma_{\hat{e}}}{\sigma_{x_a}},\tag{3.59}$$

where  $\sigma_{\hat{e}}$  and  $\sigma_{x_a}$  denote the sample standard deviations of the residual  $\hat{e}(n)$  and the analytic f-wave signal  $x_a(n)$ , respectively. The signal quality index  $\mathcal{S}$  ranges from 0 to 1, with values closer to 1 indicating a better fit between the modeled and observed signals, as illustrated in Fig. 3.4(c).

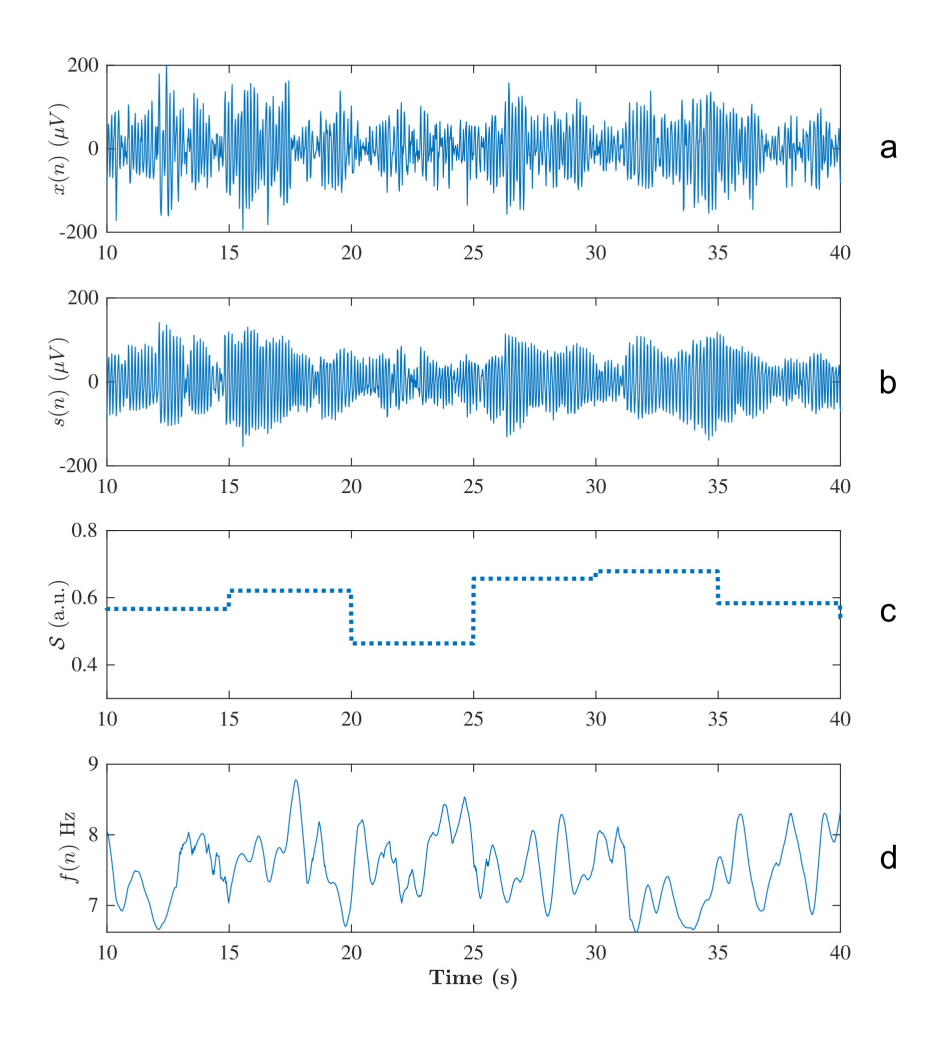


**Figure 3.4:** Illustration of the model-based f-wave analysis. (a) Extracted f-wave signal x(n). (b) Corresponding modeled signal s(n). (c) Signal quality index  $\mathcal{S}$ . (d) Extracted f-wave frequency trend f(n).

Chapter 4

# ECG Based Analysis of Respiration

# 4.1 ECG-derived respiration

ECG-derived respiration techniques allow non-invasive estimation of respiratory activity directly from the ECG. Instead of relying on dedicated respiratory sensors, these methods exploit respiration-induced changes in ECG morphology to reconstruct a surrogate respiratory signal. Such techniques are particularly useful in studies where ECG data are already available and the use of additional equipment would be impractical or undesirable.

The EDR approaches considered in this thesis are applicable to recordings in both sinus rhythm and atrial fibrillation (AF). Methods based on RR-interval variability, which reflect respiratory sinus arrhythmia (RSA) as discussed in Sec. 2.3.2, become unreliable in AF because of the irregular ventricular response. Morphology-based approaches, by contrast, remain valid since they rely on respiration-induced changes in QRS morphology rather than rhythm regularity, making them especially suitable for AF studies.

This chapter therefore focuses on morphology-based EDR methods. The considered approaches include single-lead techniques based on R-wave amplitude and R-wave morphology (angle and slope range), as well as multilead methods such as the QRS loop rotation angle. Although many additional EDR methods have been proposed in the literature, the emphasis here is placed on those most relevant to AF. Among these, the slope range method was employed in Papers II, III, and IV, while the R-wave amplitude method was specifically applied in Paper I due to the challenges introduced

by pacing spikes in pacemaker recordings. The remaining methods are included to illustrate alternative strategies. For each approach, the essential processing steps for deriving a surrogate respiration signal from single-lead or multilead ECG recordings are described.

#### 4.1.1 R-wave amplitude

A straightforward approach to EDR is based on the beat-to-beat variation in R-wave amplitude. These variations arise from respiration-induced changes in thoracic impedance, electrode position, heart geometry, and lung volume. By tracking successive R-wave amplitudes, a surrogate respiratory signal can be reconstructed [92]. In Paper I, the R-wave amplitude approach was selected because the study population consisted of pacemaker patients with permanent atrial fibrillation. The presence of pacing spikes in the ECG made alternative morphology-based methods more difficult to apply reliably.

In Paper I, respiration was extracted from amplitude modulation of the ECG, primarily reflecting R-wave amplitude variations. To emphasize slow respiratory-related changes, the ECG was first decimated to 50 Hz and low-pass filtered using a zero-phase first-order Butterworth filter with a cut-off frequency of 2 Hz, thereby preserving the respiratory band (0.1-0.5 Hz) while attenuating higher-frequency components. The envelope of the amplitude-modulated ECG was then obtained using homomorphic filtering, which relies on a logarithmic transformation of the analytic signal to separate multiplicative components such as amplitude modulation. Let x(n) denote the decimated ECG sequence. The analytic representation is computed using the Hilbert transform,

$$x_a(n) = x(n) + j \mathcal{H}\{x(n)\},$$
 (4.1)

where  $\mathcal{H}\{\cdot\}$  denotes the Hilbert transform, which shifts the phase of each frequency component by  $-90^\circ$  to form the analytic signal representation. The homomorphic envelope is then extracted as

$$\tilde{x}(n) = \exp(\mathcal{H}\{\ln|x_a(n)|\}),\tag{4.2}$$

Finally,  $\tilde{x}(n)$  was smoothed using a Savitzky–Golay filter, which applies a local polynomial regression within a sliding window. For each window of length 2M+1, a polynomial of order p is fitted by least squares, and the central point is replaced with the fitted value. This filter preserves local trends and peak morphology while reducing noise, making it particularly suitable for physiological signals. The resulting signal is denoted  $d_A(n)$ , representing the extracted EDR signal. An illustrative schematic of the processing pipeline is shown in Fig. 4.1.

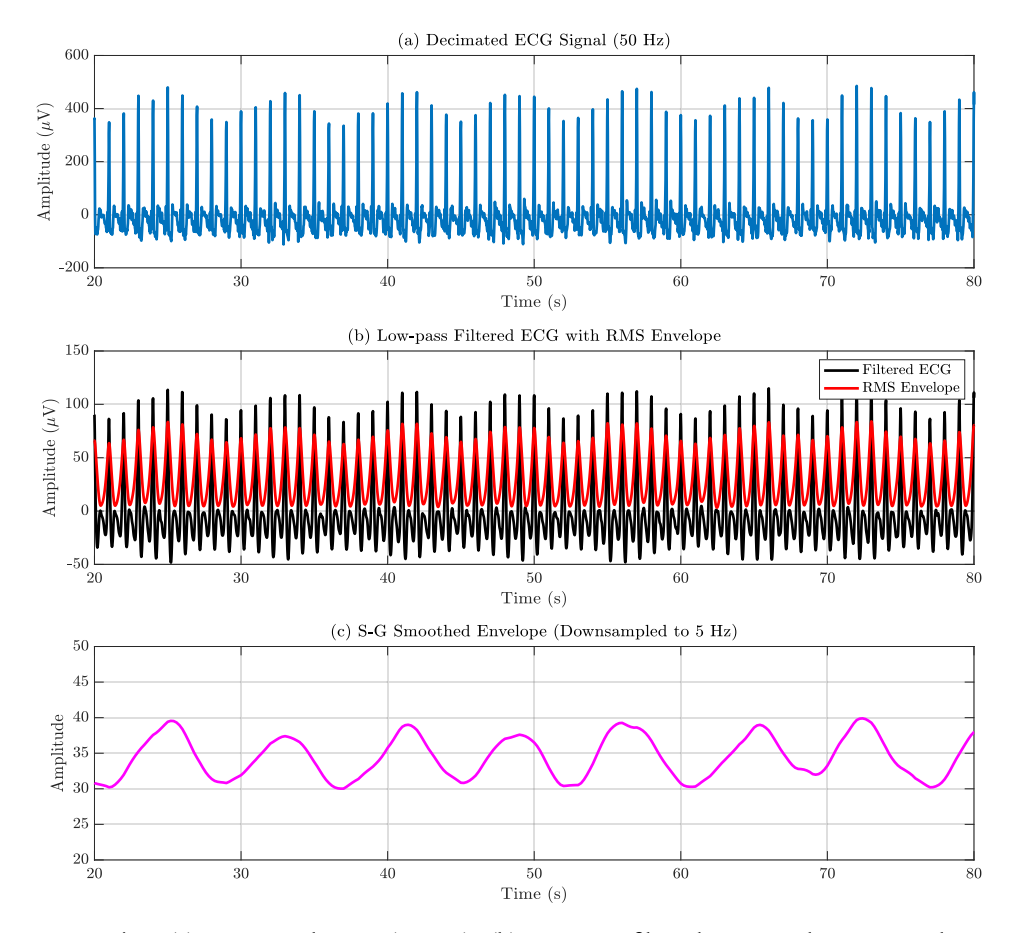


**Figure 4.1:** (a) Decimated ECG (50 Hz); (b) Low-pass filtered ECG with RMS envelope (2 Hz cutoff); (c) Smoothed envelope using a Savitzky-Golay filter, downsampled to 5 Hz.

## 4.1.2 R-wave Angle and Slope Range

Both the R-wave angle and slope range methods quantify respiratory modulation of the QRS complex by tracking beat-to-beat changes in its slopes. Respiratory-induced variations in thoracic impedance and electrode—heart geometry subtly alter the morphology of the QRS complex, and these slope-based features can be leveraged to derive an EDR signal [93, 94].

For each beat i, the QRS complex was defined over a 140 ms interval, starting 110 ms before and ending 30 ms after the R peak. Within this interval, two distinct features were extracted:

• **R-wave angle:** Two short windows were centered at the points of maximum positive slope (up-slope) and maximum negative slope (down-slope). The slopes of the best-fit lines in these windows are denoted  $I_{\mathrm{US},i}$  and  $I_{\mathrm{DS},i}$ , respectively. The R-wave angle is then defined as

$$d_{RA}(i) = \arctan\left(\frac{I_{\text{US},i} - I_{\text{DS},i}}{1 + I_{\text{US},i}I_{\text{DS},i}}\right). \tag{4.3}$$

This feature captures the relative orientation between the QRS up- and downslopes, providing a geometric descriptor of QRS shape. The use of line fitting increases robustness to high-frequency noise and minor morphological variability.

• **Slope range:** The discrete derivative of the ECG signal within the QRS interval is computed as

$$y_i'(n) = x_i(n) - x_i(n-1),$$
 (4.4)

where  $x_i(n)$  denotes the ECG samples for beat i. The slope range is defined as

$$d_{SR}(i) = \max_{n} \{y_i'(n)\} - \min_{n} \{y_i'(n)\}, \tag{4.5}$$

capturing the difference between the most extreme positive and negative slopes in the QRS complex. This method avoids line fitting, making it computationally efficient, though potentially more sensitive to high-frequency noise.

Both  $d_{RA}(i)$  and  $d_{SR}(i)$  vary slowly over time, primarily reflecting respiratory modulation. The resulting sequences can be detrended and low-pass filtered to suppress noise and enhance the respiratory component before use as EDR signals. In summary, the R-wave angle method provides a more noise-robust, geometry-based measure of QRS morphology, whereas the slope range method offers greater computational simplicity and slightly better performance in respiratory rate estimation, as shown in a comparative study of AF patients [94].

#### 4.1.3 QRS Loop Rotation Angle

The QRS loop represents the trajectory of the QRS complex in a two-dimensional space formed by two simultaneously recorded ECG leads. For each beat, the samples of the QRS complex from the two leads are plotted against each other, yielding a loop that captures the relative amplitude and timing between the leads. Respiration modulates the orientation of this loop because thoracic impedance and electrode–heart geometry change with lung volume [95].

Let  $\mathbf{Y}_i \in \mathbb{R}^{2 \times N}$  denote the QRS loop of beat i, where the rows contain the N samples of the QRS complex from two selected leads. In practice, the two leads are chosen to maximize orthogonality and signal quality, typically using standard limb and precordial leads known to exhibit clear respiratory modulation [95]. A reference loop,  $\mathbf{Y}_R$ , is defined as the average of the first ten beats with consistent morphology, where similarity is assessed by a cross-correlation coefficient greater than 0.8.

Each observed loop  $\mathbf{Y}_i$  can be approximated as a rotated, scaled, and time-shifted version of the reference loop  $\mathbf{Y}_R$ :

$$\mathbf{Y}_i \approx J_\tau \, \mathbf{Y}_R \, D \, Q, \tag{4.6}$$

where  $J_{\tau}$  is a temporal shift (synchronization) matrix, D is a diagonal amplitude scaling matrix, and Q is a  $2 \times 2$  rotation matrix. This model accounts for differences in temporal alignment, amplitude, and orientation between  $\mathbf{Y}_i$  and  $\mathbf{Y}_R$ .

To align the loops, a spatiotemporal registration is performed by minimizing the squared error between  $\mathbf{Y}_i$  and the transformed  $\mathbf{Y}_R$ . This procedure yields an estimated rotation matrix  $\hat{\mathbf{Q}}_i$  that best maps  $\mathbf{Y}_R$  onto  $\mathbf{Y}_i$ . The respiratory signal is then derived from the angular deviation of the loop, reflected in the off-diagonal elements of  $\hat{\mathbf{Q}}_i$ . Specifically, the respiratory surrogate signal  $d_{LA}(i)$  is obtained as

$$d_{LA}(i) = \arcsin\left(\hat{Q}_i(2,1)\right),\tag{4.7}$$

where  $\hat{Q}_i(2,1)$  denotes the element in the second row and first column of  $\hat{\mathbf{Q}}_i$ . Taking the arcsine emphasizes the angular interpretation of this matrix element, ensuring that the resulting signal varies approximately linearly with the respiratory-induced rotation of the QRS loop. In practice, the sequence  $d_{LA}(i)$  provides a beat-to-beat respiratory surrogate. A low-pass filter is typically applied to suppress high-frequency noise and retain the dominant respiratory component.

# 4.2 Robust Assessment of Respiratory Information

When multiple ECG leads are available, respiration-related information can be derived from each lead (or pair of leads for  $d_{LA}$ ) individually and then combined to form a more robust estimate of respiratory activity. This can be achieved using dimensionality reduction and source separation methods, which exploit inter-lead correlations and reduce the influence of noise or artifacts present in individual leads. In this section, two complementary approaches are described: principal component analysis (PCA) and periodic component analysis ( $\pi$ CA). An additional strategy, peak-conditioned spectral averaging, is presented as a general tool for reliable respiratory rate estimation.

## 4.2.1 Dimensionality Reduction Approaches

#### **Principal Component Analysis (PCA)**

Principal component analysis (PCA), introduced in Sec. 3.2.3, transforms a set of correlated signals into an orthogonal set of components ordered by explained variance. In the present context, PCA is applied to combine multiple single-lead EDR signals into a joint-lead respiration signal.

Let the lead-specific respiration signals be arranged in  $\mathbf{X} \in \mathbb{R}^{N \times L}$ , where each of the L columns corresponds to one lead and each of the N rows to a uniformly resampled time point. Since the single-lead signals are originally defined at irregular beat times, they are resampled to a common uniform grid prior to PCA. The covariance matrix is computed as

$$\mathbf{C} = \frac{1}{N-1} \mathbf{X}^{\mathsf{T}} \mathbf{X},\tag{4.8}$$

and eigendecomposition yields

$$\mathbf{C} = \mathbf{U}\boldsymbol{\Lambda}\mathbf{U}^{\top},\tag{4.9}$$

where  $\mathbf{U} = [\mathbf{u}_1, \dots, \mathbf{u}_L]$  contains eigenvectors as columns and  $\mathbf{\Lambda} = \text{diag}(\lambda_1, \dots, \lambda_L)$  contains eigenvalues. The k-th PCA component is obtained by projecting the multilead signals onto the eigenvector  $\mathbf{u}_k$ :

$$z_k(n) = \mathbf{X}(n,:) \, \mathbf{u}_k, \tag{4.10}$$

where  $\mathbf{X}(n,:)$  denotes the n-th row of  $\mathbf{X}$ , i.e., the vector of all lead values at time index n. The respiratory component is identified as the one exhibiting (i) a pronounced spectral peak in the respiratory frequency range  $(0.1-0.4 \,\mathrm{Hz})$ , and (ii) a substantial

eigenvalue  $\lambda_k$ , reflecting the fraction of variance explained by the corresponding eigenvector. The selected respiratory component is denoted  $d_{\text{PCA}}(n)$ . The selection is guided by the criterion that each eigenvalue corresponds to the variance explained by its associated component. Larger eigenvalues indicate components that capture more of the variability across leads, whereas components with very small eigenvalues typically represent only residual fluctuations and are therefore less informative for respiration estimation. This approach was employed to obtain a joint-lead EDR signal in Paper II.

#### Periodic Component Analysis ( $\pi$ CA)

Periodic component analysis ( $\pi$ CA) is a blind source separation method designed to extract the most periodic signal from multichannel data [96]. Unlike PCA, which is variance-based,  $\pi$ CA maximizes periodicity, making it well suited for respiration extraction.

Let the preprocessed EDR signals be arranged in  $\mathbf{X} \in \mathbb{R}^{N \times L}$ , where N is the number of uniformly resampled time points and L is the number of leads. As in PCA, the covariance matrix is defined as

$$\mathbf{C} = \frac{1}{N - 1} \mathbf{X}^{\mathsf{T}} \mathbf{X},\tag{4.11}$$

with eigendecomposition

$$\mathbf{C} = \mathbf{U}\boldsymbol{\Lambda}\mathbf{U}^{\top},\tag{4.12}$$

where **U** contains the eigenvectors and  $\Lambda = \text{diag}(\lambda_1, \dots, \lambda_L)$  contains the eigenvalues. The whitening transformation is then

$$\mathbf{Z} = \mathbf{\Lambda}^{-1/2} \mathbf{U}^{\mathsf{T}} \mathbf{X}^{\mathsf{T}},\tag{4.13}$$

where  $\Lambda^{-1/2}$  denotes the diagonal matrix with entries  $\lambda_i^{-1/2}$ , i.e., the reciprocal square roots of the eigenvalues. This operation scales the data so that the rows of  ${\bf Z}$  are uncorrelated and have unit variance, thus facilitating the subsequent periodicity analysis. Given  ${\bf Z}$ ,  $\pi{\rm CA}$  seeks a weight vector  ${\bf w}$  such that the projected signal

$$s(n) = \mathbf{w}^{\mathsf{T}} \mathbf{Z}(n), \tag{4.14}$$

is as periodic as possible. Here, s(n) represents a candidate joint-lead component formed as a linear combination of the whitened signals. Periodicity is quantified using the non-periodicity measure

$$\epsilon(\mathbf{w}, \tau, \mathbf{Z}) = \frac{\sum_{n} \left[ s(n) - s(n - \tau) \right]^{2}}{\sum_{n} s(n)^{2}},$$
(4.15)

evaluated over candidate lags  $\tau$  corresponding to plausible respiratory periods (0.1–0.4 Hz). The lag  $\tau_o$  yielding the smallest  $\epsilon$  defines the optimal weight  $\mathbf{w}_o$ , and the selected joint-lead respiration signal is

$$d_{\pi \text{CA}}(n) = \mathbf{w}_o^{\mathsf{T}} \mathbf{Z}(n). \tag{4.16}$$

The respiratory rate  $(f_r)$  can be obtained directly from  $\tau_o$ :

$$f_r = \frac{f_s}{\tau_o},\tag{4.17}$$

where  $f_s$  is the sampling frequency. In this way,  $\pi CA$  provides both a robust respiration surrogate and an associated frequency estimate. This approach was applied in Paper III for respiratory analysis during atrial fibrillation.

#### 4.2.2 Peak-Conditioned Spectral Averaging

Beyond PCA and  $\pi$ CA, respiratory rate  $f_r$  can be estimated from the spectral content of an EDR signal d(n). A common approach is to compute the power spectral density (PSD) and identify the dominant peak in the respiratory band (0.1–0.5 Hz). Welch's method (see Sec. 3.3.2) is typically used for PSD estimation, as it improves stability by averaging across overlapping, windowed segments. The criteria can also be applied in Welch's to exclude spectra of windowed segments of insufficient quality from the averaging. When multiple lead-specific signals are available, peak-conditioned spectral averaging further improves robustness [95, 97, 98]. Each spectrum is retained only if the respiratory peak is sufficiently pronounced (e.g., at least 85% of the global maximum) [98]. The retained spectra are then averaged, and the most prominent peak of the average is selected as  $f_r$ . This reduces the influence of noisy or poorly conditioned leads. Basic quality-control steps (e.g., checks on peak sharpness, bandwidth, and temporal consistency) are recommended to avoid spurious detections due to noise or transient artifacts.

# 4.3 Assessment of Cardiorespiratory Interactions

The interaction between cardiac and respiratory dynamics, often referred to as cardiorespiratory coupling, can be investigated using a range of analytical techniques. Such interactions provide insight into autonomic regulation and respiratory modulation of cardiac activity. Several complementary approaches are commonly used: signal decomposition methods that isolate respiration-related components, linear spectral methods that quantify frequency-specific coherence, and nonlinear informationtheoretic measures that capture more general dependencies. In this chapter, three representative methods are described: orthogonal subspace projection, coherent cross-power spectral analysis, and mutual information. These techniques were applied in Papers II–IV of this thesis to quantify respiratory modulation of atrial fibrillatory dynamics and to assess autonomic responses in experimental data.

## 4.3.1 Orthogonal Subspace Projection

Orthogonal subspace projection is a signal processing technique for separating the part of a signal that is linearly related to a known reference from the part that is unrelated [99, 100]. In cardiorespiratory analysis, this approach was originally applied to HRV to remove the linear influence of respiration on the tachogram, thereby allowing a cleaner assessment of sympathovagal balance [100]. In this thesis, the same framework is applied differently: instead of HRV, the target signal is the atrial fibrillatory frequency trend, and the goal is to quantify the magnitude of respiratory modulation (Papers II–III).

Let  $\mathbf{x} \in \mathbb{R}^M$  denote the zero-mean version of the time series of interest (e.g., the f-wave frequency trend f(n)), and let r(n) be the respiratory reference signal, both sampled at the same uniform rate. To construct the respiratory subspace, a Hankel-structured matrix  $\mathbf{V} \in \mathbb{R}^{(M-q)\times q}$  is formed from delayed versions of r(n):

$$\mathbf{V} = \begin{bmatrix} r(1) & r(2) & \dots & r(q) \\ r(2) & r(3) & \dots & r(q+1) \\ \vdots & \vdots & \ddots & \vdots \\ r(M-q) & r(M-q+1) & \dots & r(M) \end{bmatrix}, \tag{4.18}$$

where q is the embedding dimension. The projection of  $\mathbf{x}$  onto the subspace spanned by the columns of  $\mathbf{V}$  is given by

$$\mathbf{x}_r = \mathbf{V} \left( \mathbf{V}^\mathsf{T} \mathbf{V} \right)^{-1} \mathbf{V}^\mathsf{T} \mathbf{x},\tag{4.19}$$

with  $\mathbf{x}_r$  representing the component of  $\mathbf{x}$  that is linearly related to respiration. An illustrative example of this decomposition is shown in Figure 4.2. The factor

$$\Delta F = \sqrt{\frac{2}{M - q} \mathbf{x}_r^\mathsf{T} \mathbf{x}_r} \tag{4.20}$$

quantifies the absolute magnitude of the respiration-related modulation. The prefactor 2/(M-q) assumes sinusoidal modulation and provides an amplitude-equivalent

measure over the analysis window length M-q. The relative contribution of respiration is expressed as

$$P_r(\%) = \frac{\mathbf{x}_r^\mathsf{T} \mathbf{x}_r}{\mathbf{x}^\mathsf{T} \mathbf{x}} \times 100. \tag{4.21}$$

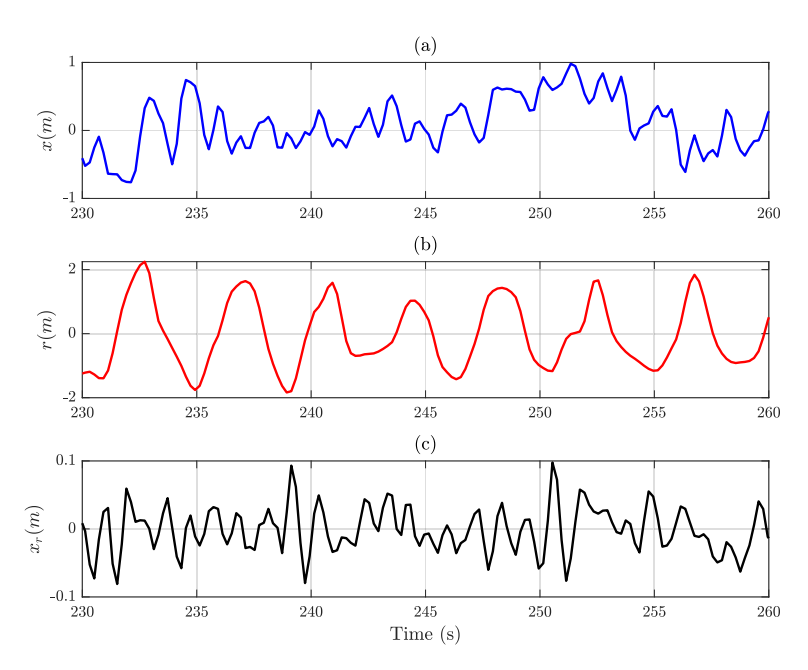


**Figure 4.2:** (a) The zero-mean atrial frequency trend x(m); (b) The respiration signal r(m) defining the projection subspace; (c) The projected component  $x_r(m)$  representing the part of x linearly related to respiration.

## 4.3.2 Coherent Cross-Power Spectral Analysis

Like orthogonal subspace projection (Sec. 4.3.1), coherent cross-power spectral analysis is a linear method that assumes cardiorespiratory coupling can be approximated as a linear process within the analysis window [101]. Given two uniformly sampled signals x(n) and y(n), their auto-power spectra  $P_{xx}(f)$  and  $P_{yy}(f)$  and cross-power spectrum  $P_{xy}(f)$  are estimated using Welch's method (see Sec. 3.3.2). Based on these segment-averaged estimates (Eqs. 3.21–3.22), the magnitude-squared coherence is defined as

$$C_{xy}(f) = \frac{|P_{xy}(f)|^2}{P_{xx}(f)P_{yy}(f)}. (4.22)$$

which quantifies the linear correlation between x and y at frequency f, ranging from 0 (no coupling) to 1 (perfect coupling). The coherent cross-power spectral index (CPC) further combines the strength of common oscillations with the stability of their phase relationship:

$$CPC(f) = |P_{xy}(f)| \cdot C_{xy}(f). \tag{4.23}$$

Band-averaged CPC values are typically derived for physiologically relevant regions, such as the low-frequency (LF: 0.04–0.15 Hz) and high-frequency/respiratory (HF: 0.15–0.4 Hz) bands [102]. Figure 4.3 illustrates the estimation of  $P_{xx}(f)$ ,  $P_{yy}(f)$ ,  $P_{xy}(f)$ , and  $C_{xy}(f)$  for representative HRV and respiration signals, highlighting the LF and HF bands commonly analyzed in cardiorespiratory coupling studies.

In this thesis, CPC was applied in Paper IV to assess the stability of cardiorespiratory coupling in healthy volunteers exposed to HVO exhaust in a controlled chamber study.

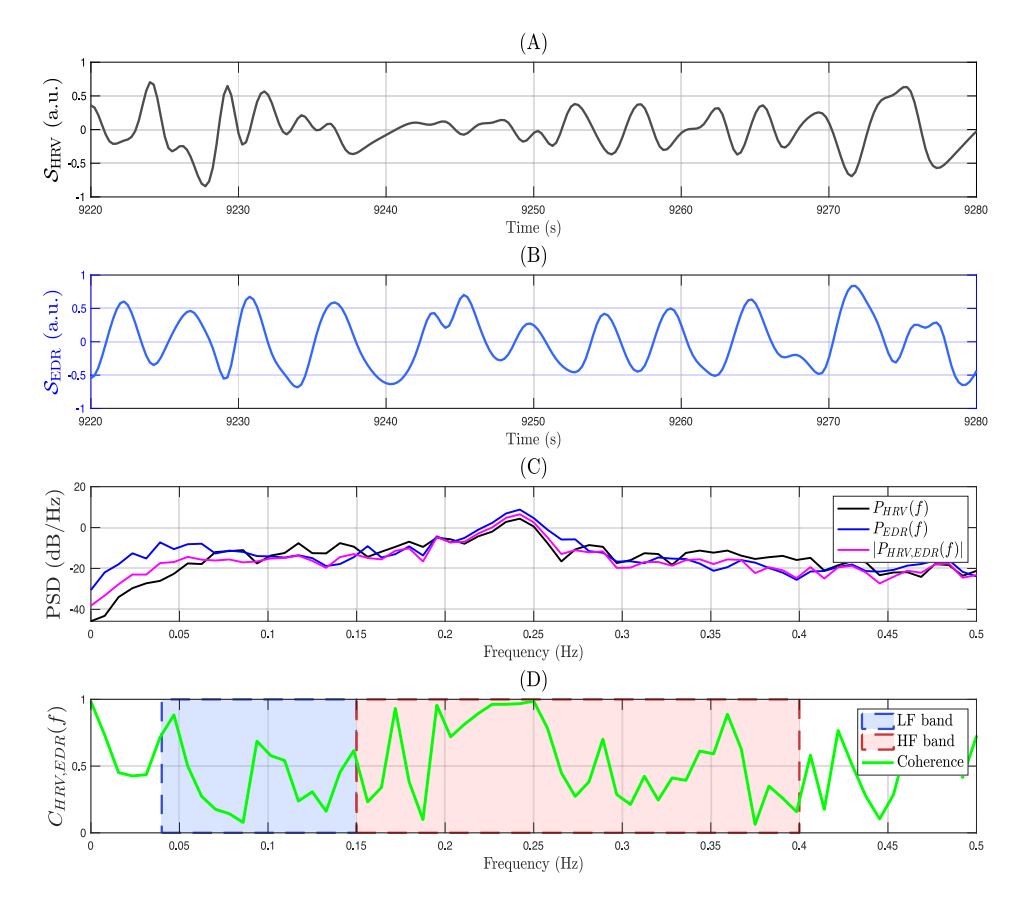


**Figure 4.3:** Illustration of coherent cross-power spectral analysis between HRV and respiration. (A) Normalized HRV signal ( $\mathcal{S}_{HRV}$ , a.u.) and (B) normalized EDR signal ( $\mathcal{S}_{EDR}$ , a.u.) over a representative 60-second window. (C) Power spectral densities (PSD) of HRV and EDR ( $P_{xx}(f)$  and  $P_{yy}(f)$ , dB/Hz), together with the cross-power spectrum magnitude ( $|P_{xy}(f)|$ , dB/Hz). (D) Magnitude-squared coherence  $C_{xy}(f)$  (dimensionless), with shaded regions indicating the low-frequency (LF: 0.04–0.15 Hz) and high-frequency (HF: 0.15–0.4 Hz) bands.

#### 4.3.3 Mutual Information

While linear methods detect frequency-specific coupling, they may miss more complex dependencies. Mutual information (MUI) is an information-theoretic measure that quantifies the amount of shared information between two random variables X and Y [101]. It is defined as

$$MUI(X;Y) = H(X) + H(Y) - H(X,Y),$$
 (4.24)

where  $H(X) = -\sum_x p(x)\log p(x)$  and  $H(Y) = -\sum_y p(y)\log p(y)$  are the marginal entropies, and  $H(X,Y) = -\sum_{x,y} p(x,y)\log p(x,y)$  is the joint entropy. MUI is zero if X and Y are statistically independent and increases with stronger dependencies, whether linear or nonlinear. In practical implementations, continuous signals are first discretized into a small number of amplitude states to enable robust probability estimation. A common strategy is quantile-based binning, where the signal range is partitioned into equally populated bins, ensuring balanced histograms and stable entropy estimates even for relatively short recordings [103].

By combining linear measures with nonlinear measures such as MUI, cardiorespiratory coupling analysis can provide a more comprehensive view of the interaction between cardiac and respiratory dynamics. Linear methods identify frequency-specific, phase-locked coupling, while nonlinear methods reveal broader dependencies that may arise from complex physiological interactions. In this thesis, these techniques are applied in Paper IV to assess the stability of cardiorespiratory coupling in healthy volunteers exposed to HVO exhaust in a controlled chamber study.

Chapter 5 \_\_\_\_\_\_
Summary of Papers

# 5.1 Paper I - Respiratory Induced Modulation in f-wave Characteristics During Atrial Fibrillation

This study presents the first systematic attempt to quantify respiratory modulation in the f-wave frequency trend during AF using resting ECG recordings. The motivation for this work stems from the observation that respiration influences atrial activity through both autonomic and mechanical mechanisms, yet its effect on f-wave characteristics had not been previously quantified.

Following QRST cancellation, the f-wave was extracted and its frequency trend estimated using a model-based approach [104]. The respiratory rate was derived from the ECG using the R-wave amplitude method and peak-conditioned spectral averaging to ensure robustness [98], and was used to set the centre frequency of a narrow bandpass filter applied to the f-wave frequency trend. The envelope of the filtered signal was taken as an estimate of the amplitude of respiratory f-wave frequency modulation. The method was first validated using simulated f-wave signals generated from a sinusoidal harmonic model, showing that for high-quality signals ( $\mathcal{S}>0.5$ ) the modulation amplitude could be estimated with an error below 0.01 Hz.

The approach was applied to ECG data from eight pacemaker patients with persistent AF recorded under three conditions: baseline, controlled respiration, and controlled respiration after atropine administration to block parasympathetic influences. The results, summarised in Table 5.1, show that the respiratory f-wave frequency modulation is higher during deep breathing and often lower after atropine injection, suggesting that parasympathetic ANS regulation contributes to the modulation.

**Table 5.1:** Estimated mean  $(\pm \, \mathrm{SD})$  respiratory modulation amplitude  $(\Delta \hat{f})$  and mean f-wave frequency  $(\hat{f})$  across baseline (B), controlled respiration (CR), and post-atropine (PA) phases. Subscripts  $\{\mathrm{B},\,\mathrm{CR},\,\mathrm{PA}\}$  indicate the recording phase. An asterisk (\*) denotes significant differences compared to B, and a bullet  $(\bullet)$  denotes significant differences compared to CR. The baseline recording from patient g was excluded due to insufficient signal quality  $(\mathcal{S})$ .

Patient	$\Delta\hat{f}_B$ (Hz)	$\Delta\hat{f}_{CR}$ (Hz)	$\Delta \hat{f}_{PA}$ (Hz)	$\hat{f}_B$ (Hz)	$\hat{f}_{CR}$ (Hz)	$\hat{f}_{PA}$ (Hz)
a	$0.16 \pm 0.06$	$0.17 \pm 0.09^*$	$0.16 \pm 0.08^{\bullet}$	$6.84 \pm 0.43$	$6.77 \pm 0.45^*$	$6.71 \pm 0.41^{\bullet*}$
С	$0.13 \pm 0.06$	$0.16 \pm 0.08^*$	$0.13 \pm 0.07^{\bullet}$	$6.17 \pm 0.35$	$6.31 \pm 0.37^*$	$6.46 \pm 0.36^{\bullet*}$
d	$0.16 \pm 0.08$	$0.17 \pm 0.08^*$	$0.14 \pm 0.07^{\bullet*}$	$6.57 \pm 0.43$	$6.75 \pm 0.39^*$	$6.36 \pm 0.43^{\bullet*}$
e	$0.16 \pm 0.08$	$0.19 \pm 0.10^*$	$0.19 \pm 0.10^*$	$7.68 \pm 0.51$	$7.39 \pm 0.54^*$	$7.57 \pm 0.54^{\bullet*}$
f	$0.14 \pm 0.07$	$0.21 \pm 0.10^*$	$0.21\pm0.12^*$	$7.46 \pm 0.46$	$7.29 \pm 0.49^*$	$7.14 \pm 0.48^{\bullet*}$
g	_	$0.17 \pm 0.08$	$0.16 \pm 0.08^{\bullet}$	_	$5.91 \pm 0.41$	$5.96 \pm 0.42^{\bullet}$
h	$0.15 \pm 0.08$	$0.17\pm0.07^*$	$0.17\pm0.07^*$	$7.73 \pm 0.43$	$8.11\pm0.44^*$	$7.98 \pm 0.43^{\bullet*}$
Overall average	$0.15 \pm 0.01$	$0.18 \pm 0.02$	$0.17 \pm 0.03$	$7.07 \pm 0.64$	$6.93 \pm 0.73$	$6.88 \pm 0.71$

# 5.2 Paper II - A Subspace Projection Approach to Quantify Respiratory Variations in the f-wave Frequency Trend

This study builds on the work of Paper I by introducing an orthogonal subspace projection (OSP) approach to quantify respiration-induced modulation in the f-wave frequency trend during AF. Unlike the narrow-band filtering approach in Paper I, which required accurate estimation of the respiratory frequency, OSP directly projects the f-wave frequency trend onto a subspace defined by a respiratory reference signal, enabling selective extraction of the respiration-related component without explicit bandpass filtering.

The OSP method is described in detail in Sec. 4.3.1. In brief, it projects the f-wave frequency trend onto a subspace spanned by delayed versions of a respiratory reference signal, thereby extracting the respiration-related component. In Paper II, the respiratory reference r(m) was obtained as an ECG-derived respiration signal using the slope range method (Sec. 4.1.2) applied beat-wise to the QRS complexes, with principal component analysis used to form a joint-lead signal (Sec. 4.2.1). The f-wave frequency trend f(m) was estimated from the analytic f-wave signal using the harmonic model-based approach described in Sec. 3.4.1. Projection of f(m) onto the respiratory subspace defined by r(m) yielded the respiration-related component, from which the absolute modulation magnitude ( $\Delta f_{\rm OSP}$ ) was computed.

The OSP method was evaluated using both simulated and clinical AF data. Results from analysis of simulated data demonstrated that OSP more accurately recovered the modulation amplitude than the previous bandpass filtering method, particularly in noisy conditions and when respiration frequency varied over time. Clinical recordings from 28 patients with persistent AF were analysed during baseline and deep breathing phases. Group-level analysis showed no statistically significant difference in  $\Delta f_{\rm OSP}$  between baseline and deep breathing, although individual responses varied, as shown in Figure 5.1. While some individuals exhibited higher values during deep breathing compared to baseline, others showed little or no change, illustrating the marked interindividual variability in respiration-induced modulation of the f-wave frequency.

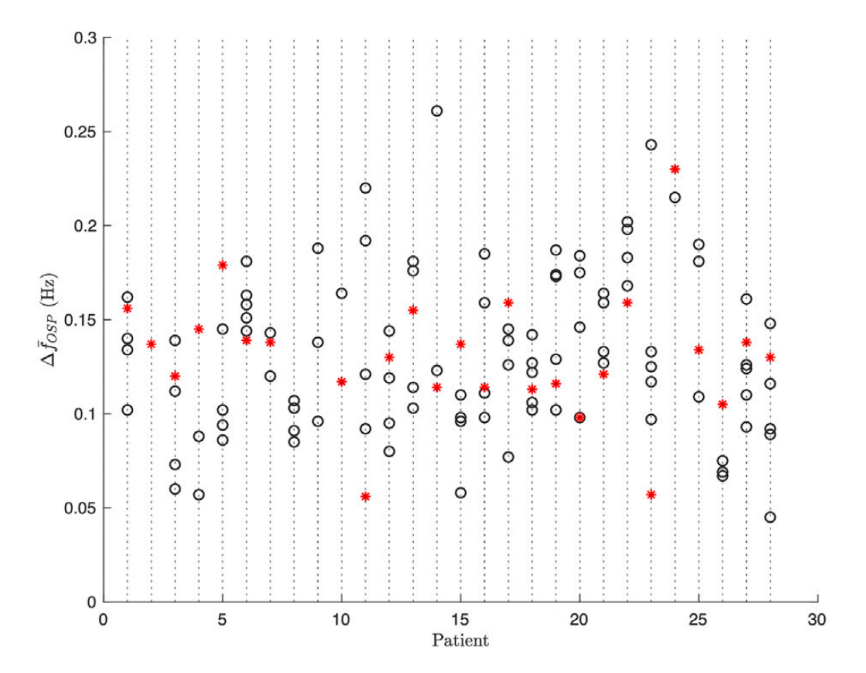


**Figure 5.1:** Estimates of respiration-induced f-wave frequency variations ( $\Delta f_{\rm OSP}$ ) for all one-minute segments from each patient during baseline (black circles) and deep breathing (red points) phases.

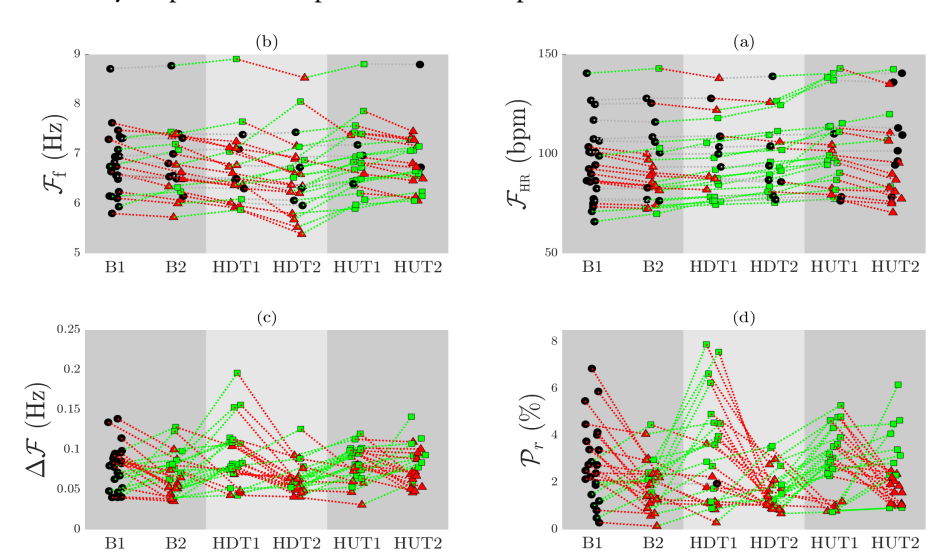
# 5.3 Paper III - Tilt-induced Changes in f-wave Characteristics During Atrial Fibrillation: An Experimental and Computational Investigation

This study applied the methodology developed in Paper II to investigate how the ANS influences AF dynamics during postural changes, and to examine the impact of sympathetic and parasympathetic activity on the mean f-wave frequency  $(F_f)$  and respiration-related modulation of the f-wave frequency  $(\Delta F_f)$ . The findings were compared with computational simulations of atrial tissue during AF under varying levels of acetylcholine (ACh, parasympathetic stimulation) and isoproterenol (Iso, sympathetic stimulation).

Electrocardiograms recorded from patients with persistent AF during a tilt test including baseline supine rest, head-down tilt (HDT), and head-up tilt (HUT) were analyzed [105]. Each phase was divided into a transient period (first two minutes) and a steady-state period (last three minutes). The mean  $F_f$ ,  $\Delta F_f$ , and the respiratory power ratio  $P_r$  were estimated for each period using the harmonic model-based frequency estimation and the orthogonal subspace projection method proposed in Paper II. In parallel, 2D and 3D biatrial simulations were performed under different levels of ACh and Iso to mimic parasympathetic and sympathetic stimulation, respectively.

Figure 5.2 summarizes the results of the analysis across the tilt test. The mean heart rate  $(F_{HR})$  and f-wave frequency  $(F_f)$  exhibited heterogeneous patient-specific responses, although at the group level  $F_f$  tended to decrease from baseline to HDT and increase again during HUT. The respiration-related modulation index  $(\Delta F_f)$  and the percentage of respiratory contribution  $(P_r)$  also varied substantially among individuals. Group-level analysis showed that  $\Delta F_f$  increased during transient HDT, decreased during steady HDT, and increased again during early HUT. Simulation results demonstrated that Iso consistently increased  $F_f$ , whereas cyclic fluctuations in ACh concentration primarily determined the magnitude of  $\Phi F_f$ , with larger ACh variations producing stronger respiration-related modulation. Their combined action produced complex interactive effects that mirrored the diverse clinical responses.

In summary, tilt maneuvers induced clear, phase-dependent changes in f-wave patterns that reflect shifts in autonomic balance: sympathetic activity predominantly influenced the mean fibrillatory rate  $(F_f)$ , whereas parasympathetic activity modulated respiration-related variations  $(\Delta F_f)$ . Combining tilt-test analysis with computational simulations provides a non-invasive framework for assessing autonomic function in



AF and may help tailor therapies to individual patients.

**Figure 5.2:** Individual patient trends for (a)  $\mathcal{F}_{HR}$ , (b)  $\mathcal{F}_f$ , (c)  $\Delta \mathcal{F}_f$ , and (d)  $\mathcal{P}_r$  across the tilt test. Responses relative to the preceding period are illustrated by point shapes and line colors: increases are shown by green squares with green lines, decreases by red triangles with red lines, and minimal variations (less than 1%) by black circles with gray lines.

# 5.4 Paper IV - A Chamber Study of Respiratory and Autonomic Responses to Hydrotreated Vegetable Oil Exhaust Using ECG-Derived Respiration

This study investigated physiological effects of short-term exposure to hydrotreated vegetable oil (HVO) exhaust in healthy adults. The specific objectives were to evaluate whether autonomic and respiratory regulation, as reflected in HRV, EDR, and cardiorespiratory coupling, were altered by exposures to dilute HVO exhaust. In the context of this thesis, Paper IV extends the application of cardiorespiratory coupling as a non-invasive marker of autonomic modulation in healthy individuals exposed to environmental stressors.

Nineteen volunteers (10 men, 9 women, aged 20–55 years) participated in a randomized, double-blind, crossover chamber study. Each participant underwent four three-hour exposures: (A) filtered air, (B) filtered air with NaCl particles, (C) HVO exhaust with aftertreatment, and (D) HVO exhaust without aftertreatment. Continuous ECG recordings were acquired and processed to extract time-domain and frequency-domain HRV features, respiratory frequency and amplitude from EDR, and cardiorespiratory coupling indices including coherent cross-power spectral coupling in the low- and high-frequency bands (CPC<sub>LF</sub>, CPC<sub>HF</sub>, CPC<sub>LF/HF</sub>) and mutual information (MUI). A linear mixed model (LMM) was fitted to evaluate time- and exposure-related effects:

$$Y_{ijp} = \beta_0 + \beta_t \operatorname{Time}_j + \beta_B \operatorname{Time}_j + \beta_C \operatorname{Time}_j + \beta_D \operatorname{Time}_j + b_{0ip} + b_{1ip} \operatorname{Time}_j + \epsilon_{ijp},$$
(5.1)

where  $Y_{ijp}$  denotes the measurement of a given feature for subject i at time point j under exposure p. The term  $\beta_0$  is the fixed intercept representing the baseline level in the reference exposure, while  $\beta_t$  captures the overall effect of time. The coefficients  $\beta_B$ ,  $\beta_C$ , and  $\beta_D$  represent additional time-related effects specific to exposure scenarios B, C, and D relative to the reference. The random effects  $b_{0ip}$  and  $b_{1ip}$  account for subject-specific deviations in intercept and slope within each exposure scenario, and  $\epsilon_{ijp}$  denotes the residual error.

Table 5.2 summarizes the estimated fixed effects from the LMM across HRV, EDR, and cardiorespiratory coupling indices. The group-level time effects  $(\beta_t)$  were small and likely reflected normal intra-day variations. Results indicate no significant effects of the exposures  $(\beta_B, \beta_C, \beta_D)$ . Thus, short-term exposure to HVO exhaust at concentrations near EU occupational exposure limits did not measurably affect autonomic or respiratory regulation in this healthy cohort.

Feature	$\beta_0$	$\beta_t$	$\beta_B$	$\beta_C$	$\beta_D$				
HRV features									
$P_{LF}$ (s <sup>2</sup> ) $0.0053^*$ $-2.37 \times 10^{-6}$ $-2.67 \times 10^{-7}$ $-3.35 \times 10^{-6}$ $-$									
$P_{HF}$ (s <sup>2</sup> )	0.0029*	$-2.80 \times 10^{-6}$	$1.50 \times 10^{-6}$	$-2.20\times10^{-6}$	$-5.46 \times 10^{-7}$				
LF/HF (n.u.)	2.2032*	$1.28 \times 10^{-3}$	$9.32 \times 10^{-4}$	$5.01 \times 10^{-4}$ $-5.98 \times 10^{-5}$	$1.32 \times 10^{-3}$				
$LF_{norm}$ (n.u.)	0.6103*	$2.66 \times 10^{-4*}$	$2.66 \times 10^{-4*}$   $-2.57 \times 10^{-5}$		$-7.87 \times 10^{-5}$				
$HF_{norm}$ (n.u.)	0.3897*	$-2.66 \times 10^{-4}$	$2.57 \times 10^{-5}$	$5.98 \times 10^{-5}$	$7.87 \times 10^{-5}$				
$NN_{mean}$ (s)	1.0159*	$-1.97 \times 10^{-4}$	$-1.49 \times 10^{-5}$	$-1.98 \times 10^{-4}$	$2.26 \times 10^{-5}$				
SDNN (s)	0.0661*	$1.20 \times 10^{-5}$	$-8.44 \times 10^{-6}$	$-3.75 \times 10^{-5}$	$-4.24 \times 10^{-5}$				
RMSSD (s)	0.0611*	$-1.75 \times 10^{-5}$	$-1.21 \times 10^{-5}$	$-4.47 \times 10^{-5}$	$-2.08 \times 10^{-5}$				
SDSD (s)	0.0612*	$-1.76 \times 10^{-5}$	$-1.21 \times 10^{-5}$	$-4.47 \times 10^{-5}$	$-2.08 \times 10^{-5}$				
		EDR fe	eatures						
$F_R$ (Hz)	0.2592*	$2.61 \times 10^{-5}$	$-2.15 \times 10^{-6}$	$-1.06 \times 10^{-5}$	$2.63 \times 10^{-5}$				
$A_R$ (a.u.)	0.2885*	$-2.53 \times 10^{-5}$	$7.82 \times 10^{-5}$	$3.17 \times 10^{-5}$	$2.63 \times 10^{-5}$				
CRC features									
MUI (n.u.)	0.1012*	$-3.11 \times 10^{-5}$	$4.70 \times 10^{-5}$	$-3.92 \times 10^{-5}$	$-1.80 \times 10^{-5}$				
$CPC_{LF}$ (n.u.)	0.1615*	$1.12 \times 10^{-5}$	$-8.38 \times 10^{-6}$	$-3.57 \times 10^{-5}$	$-1.52 \times 10^{-5}$				
$CPC_{HF}$ (n.u.)	0.1222*	$7.34 \times 10^{-6}$	$-3.54 \times 10^{-6}$	$-2.78 \times 10^{-5}$	$1.06 \times 10^{-5}$				
$CPC_{LF/HF}$ (n.u.)	1.9399*	$-1.94 \times 10^{-4}$	$-2.48 \times 10^{-4}$	$9.44 \times 10^{-5}$	$4.02 \times 10^{-4}$				

**Table 5.2:** Fixed effects coefficients from linear mixed models in Paper IV. Significant coefficients (p < 0.05) are marked with an asterisk (\*).

#### **Author's Declaration of Generative AI Assistance**

I used generative AI tools to assist with academic editing and language refinement during the writing of this thesis, specifically OpenAI's ChatGPT (GPT-5, 2025). The AI was used exclusively to enhance clarity, grammar, structure, and tone in sections that I drafted myself. No part of the conceptual development, content generation, or idea formulation was performed by the AI. All suggestions provided by the tool were critically reviewed, edited, and verified by me.

- [1] I. C. Van Gelder, M. Rienstra, K. V. Bunting, *et al.*, "2024 ESC Guidelines for the management of atrial fibrillation developed in collaboration with the European Association for Cardio-Thoracic Surgery (EACTS)," *European Heart Journal*, p. ehae176, 2024.
- [2] R. K. Clark, *Anatomy and physiology: understanding the human body.* Jones & Bartlett Learning, 2005.
- [3] C. Antzelevitch and A. Burashnikov, "Overview of basic mechanisms of cardiac arrhythmia," *Cardiac electrophysiology clinics*, vol. 3, no. 1, p. 23, 2011.
- [4] M. T. Keating and M. C. Sanguinetti, "Molecular and cellular mechanisms of cardiac arrhythmias," *Cell*, vol. 104, no. 4, pp. 569–580, 2001.
- [5] T. Watanabe, Modeling Electrochemical Dynamics and Signaling Mechanisms in Excitable Cells with Pathological Case Studies. Academic Press, 2022.
- [6] E. Pueyo, J. P. Martínez, and P. Laguna, "Cardiac repolarization analysis using the surface electrocardiogram," *Philosophical Transactions of the Royal Society A: Mathematical, Physical and Engineering Sciences*, vol. 367, no. 1887, pp. 213–233, 2009.
- [7] L. Skibsbye, C. Poulet, J. G. Diness, B. H. Bentzen, *et al.*, "Small-conductance calcium-activated potassium (SK) channels contribute to action potential repolarization in human atria," *Cardiovascular research*, vol. 103, no. 1, pp. 156–167, 2014.
- [8] M. Courtemanche, R. J. Ramirez, and S. Nattel, "Ionic mechanisms underlying human atrial action potential properties: insights from a mathemati-

- cal model," American Journal of Physiology-Heart and Circulatory Physiology, vol. 275, no. 1, pp. H301–H321, 1998.
- [9] G. Levine, *Color Atlas of Cardiovascular Disease*. Jaypee Brothers Medical Publishers Pvt. Limited, 2014.
- [10] R. W. Shields Jr, "Functional anatomy of the autonomic nervous system," *Journal of clinical Neurophysiology*, vol. 10, no. 1, pp. 2–13, 1993.
- [11] J. Hadaya and J. L. Ardell, "Autonomic modulation for cardiovascular disease," *Frontiers in physiology*, vol. 11, p. 617459, 2020.
- [12] J. A. Armour, "Functional anatomy of intrathoracic neurons innervating the atria and ventricles," *Heart Rhythm*, vol. 7, no. 7, pp. 994–996, 2010.
- [13] J. A. Waxenbaum, V. Reddy, and M. A. Varacallo, "Anatomy, autonomic nervous system," in *StatPearls [Internet]*, StatPearls Publishing, 2023.
- [14] I. Stanković, I. Adamec, V. Kostić, and M. Habek, "Autonomic nervous system-anatomy, physiology, biochemistry," in *International Review of Movement Disorders*, vol. 1, pp. 1–17, Elsevier, 2021.
- [15] T. Kawashima, "The autonomic nervous system of the human heart with special reference to its origin, course, and peripheral distribution," *Anatomy and embryology*, vol. 209, pp. 425–438, 2005.
- [16] M. J. Shen and D. P. Zipes, "Role of the autonomic nervous system in modulating cardiac arrhythmias," *Circulation research*, vol. 114, no. 6, pp. 1004–1021, 2014.
- [17] C.-W. Chiou, J. N. Eble, and D. P. Zipes, "Efferent vagal innervation of the canine atria and sinus and atrioventricular nodes: the third fat pad," *Circulation*, vol. 95, no. 11, pp. 2573–2584, 1997.
- [18] J. A. Armour, "Intrinsic cardiac neurons involved in cardiac regulation possess alpha 1-, alpha 2-, beta 1-and beta 2-adrenoceptors.," *The Canadian journal of cardiology*, vol. 13, no. 3, pp. 277–284, 1997.
- [19] J. A. Armour, "Potential clinical relevance of the 'little brain' on the mammalian heart," *Experimental physiology*, vol. 93, no. 2, pp. 165–176, 2008.
- [20] J. A. Armour, D. A. Murphy, B.-X. Yuan, S. MacDonald, and D. A. Hopkins, "Gross and microscopic anatomy of the human intrinsic cardiac nervous system," *The Anatomical Record: An Official Publication of the American Association of Anatomists*, vol. 247, no. 2, pp. 289–298, 1997.

- [21] M. J. Shen, E.-K. Choi, A. Y. Tan, et al., "Neural mechanisms of atrial arrhythmias," *Nature Reviews Cardiology*, vol. 9, no. 1, pp. 30–39, 2012.
- [22] F. Yasuma and J.-i. Hayano, "Respiratory sinus arrhythmia: why does the heartbeat synchronize with respiratory rhythm?," *Chest*, vol. 125, no. 2, pp. 683–690, 2004.
- [23] W. Burggren, A. Fahlman, and W. Milsom, "Breathing patterns and associated cardiovascular changes in intermittently breathing animals:(Partially) correcting a semantic quagmire," *Experimental Physiology*, vol. 109, no. 7, pp. 1051–1065, 2024.
- [24] A. F. Sved, S. Ito, and C. J. Madden, "Baroreflex dependent and independent roles of the caudal ventrolateral medulla in cardiovascular regulation," *Brain research bulletin*, vol. 51, no. 2, pp. 129–133, 2000.
- [25] I. Tonhajzerova, M. Mestanik, A. Mestanikova, and A. Jurko, "Respiratory sinus arrhythmia as a non-invasive index of 'brain-heart'interaction in stress," *Indian Journal of Medical Research*, vol. 144, no. 6, pp. 815–822, 2016.
- [26] K. Kiyono, J. Hayano, E. Watanabe, and Y. Yamamoto, "Heart rate variability (HRV) and sympathetic nerve activity," *Clinical assessment of the autonomic nervous system*, pp. 147–161, 2016.
- [27] Z. Visnovcova, A. Calkovska, and I. Tonhajzerova, "Heart rate variability and electrodermal activity as noninvasive indices of sympathovagal balance in response to stress," *Acta Medica Martiniana*, vol. 13, no. 1, p. 5, 2013.
- [28] R. S. Wijesurendra and B. Casadei, "Mechanisms of atrial fibrillation," *Heart*, vol. 105, no. 24, pp. 1860–1867, 2019.
- [29] D. Ko, M. K. Chung, P. T. Evans, E. J. Benjamin, and R. H. Helm, "Atrial fibrillation: a review," *JAMA*, 2025.
- [30] K. Patel, J. Romero, and L. Di Biase, "Persistent atrial fibrillation: should we always ice the back of the left atrium?," *Journal of Interventional Cardiac Electrophysiology*, vol. 56, no. 1, pp. 95–97, 2019.
- [31] D. R. V. Wagoner, "Electrophysiological remodeling in human atrial fibrillation," *Pacing and clinical electrophysiology*, vol. 26, no. 7p2, pp. 1572–1575, 2003.
- [32] S. Dhein and A. Salameh, "Remodeling of cardiac gap junctional cell-cell coupling," *Cells*, vol. 10, no. 9, p. 2422, 2021.

[33] E. Kwan, E. Ghafoori, W. Good, M. Regouski, B. Moon, J. M. Fish, E. Hsu, I. A. Polejaeva, R. S. MacLeod, D. J. Dosdall, *et al.*, "Diffuse functional and structural abnormalities in fibrosis: Potential structural basis for sustaining atrial fibrillation," *Heart Rhythm*, 2024.

- [34] P. Coumel, P. Attuel, J. Lavallee, D. Flammang, J. Leclercq, and R. Slama, "The atrial arrhythmia syndrome of vagal origin," *Archives des maladies du coeur et des vaisseaux*, vol. 71, no. 6, pp. 645–656, 1978.
- [35] T. Tomita, M. Takei, Y. Saikawa, T. Hanaoka, S.-I. Uchikawa, H. Tsutsui, M. Aruga, T. Miyashita, Y. Yazaki, H. Imamura, *et al.*, "Role of autonomic tone in the initiation and termination of paroxysmal atrial fibrillation in patients without structural heart disease," *Journal of cardiovascular electrophysiology*, vol. 14, no. 6, pp. 559–564, 2003.
- [36] A. Y. Tan, S. Zhou, M. Ogawa, J. Song, M. Chu, H. Li, M. C. Fishbein, S.-F. Lin, L. S. Chen, and P.-S. Chen, "Neural mechanisms of paroxysmal atrial fibrillation and paroxysmal atrial tachycardia in ambulatory canines," *Circulation*, vol. 118, no. 9, pp. 916–925, 2008.
- [37] M. Ogawa, S. Zhou, A. Y. Tan, J. Song, G. Gholmieh, M. C. Fishbein, H. Luo, R. J. Siegel, H. S. Karagueuzian, L. S. Chen, et al., "Left stellate ganglion and vagal nerve activity and cardiac arrhythmias in ambulatory dogs with pacing-induced congestive heart failure," *Journal of the American College of Cardiology*, vol. 50, no. 4, pp. 335–343, 2007.
- [38] V. Malik, D. Linz, and P. Sanders, "The role of the autonomic nervous system as both "trigger and "substrate" in atrial fibrillation," *Cardiac Electrophysiology Clinics*, vol. 16, no. 3, pp. 271–280, 2024.
- [39] B. Vandenberk, P. Haemers, and C. Morillo, "The autonomic nervous system in atrial fibrillation—pathophysiology and non-invasive assessment," *Frontiers in Cardiovascular Medicine*, vol. 10, p. 1327387, 2024.
- [40] J. Heijman, N. Voigt, S. Nattel, and D. Dobrev, "Calcium handling and atrial fibrillation," *Wiener Medizinische Wochenschrift*, vol. 162, no. 13, pp. 287–291, 2012.
- [41] A. M. Gillis and D. Dobrev, "Targeting the ryr2 to prevent atrial fibrillation," *Circulation: Arrhythmia and Electrophysiology*, vol. 15, no. 10, p. e011514, 2022.

- [42] J. A. Joglar, M. K. Chung, A. L. Armbruster, E. J. Benjamin, J. Y. Chyou, E. M. Cronin, A. Deswal, L. L. Eckhardt, Z. D. Goldberger, R. Gopinathannair, et al., "2023 ACC/AHA/ACCP/HRS guideline for the diagnosis and management of atrial fibrillation: a report of the American College of Cardiology/American Heart Association Joint Committee on Clinical Practice Guidelines," *Journal of the American College of Cardiology*, vol. 83, no. 1, pp. 109–279, 2024.
- [43] M. Alobaida and A. Alrumayh, "Rate control strategies for atrial fibrillation," *Annals of medicine*, vol. 53, no. 1, pp. 682–692, 2021.
- [44] K. Filipovic, A. Sultan, J. Lüker, J.-H. van den Bruck, J. Wörmann, C. Scheurlen, J.-H. Schipper, S. Dittrich, and D. Steven, "Comparison of pulmonary vein isolation between two commercially available cryoballoon systems," *International Journal of Arrhythmia*, vol. 25, no. 1, p. 17, 2024.
- [45] U. Ahmed, F. Kamran, S. Ahmed, D. A. Ashraf, M. I. Bilal, Z. Amin, and E. Ahmad, "Outcomes of pulmonary vein isolation with or without adjunctive posterior wall isolation in patients with paroxysmal atrial fibrillation: A systematic review and meta-analysis," *Circulation*, vol. 150, no. Suppl\_1, pp. A4139264–A4139264, 2024.
- [46] S. Yamashita, A. Mizukami, M. Ono, J. Hiroki, S. Miyakuni, T. Arashiro, D. Ueshima, A. Matsumura, S. Miyazaki, and T. Sasano, "The positive F wave in lead v1 of typical atrial flutter is caused by activation of the right atrial appendage: Insight from mapping during entrainment from the right atrial appendage," *Journal of Cardiovascular Electrophysiology*, vol. 35, no. 11, pp. 2211–2219, 2024.
- [47] M. Holm, S. Pehrson, M. Ingemansson, L. Sörnmo, R. Johansson, L. Sandhall, M. Sunemark, B. Smideberg, C. Olsson, and S. B. Olsson, "Non-invasive assessment of the atrial cycle length during atrial fibrillation in man: introducing, validating and illustrating a new ECG method," *Cardiovascular research*, vol. 38, no. 1, pp. 69–81, 1998.
- [48] A. Bollmann, N. Kanuru, K. McTeague, P. Walter, D. DeLurgio, and J. Langberg, "Frequency analysis of human atrial fibrillation using the surface electrocardiogram and its response to ibutilide," *The American journal of cardiology*, vol. 81, no. 12, pp. 1439–1445, 1998.
- [49] S. Petrutiu, A. V. Sahakian, and S. Swiryn, "Abrupt changes in fibrillatory wave characteristics at the termination of paroxysmal atrial fibrillation in humans," *Europace*, vol. 9, no. 7, pp. 466–470, 2007.

[50] H. Grubitzsch, D. Modersohn, T. Leuthold, and W. Konertz, "Analysis of atrial fibrillatory activity from high-resolution surface electrocardiograms: Evaluation and application of a new system," *Experimental & Clinical Cardiology*, vol. 13, no. 1, p. 29, 2008.

- [51] V. D. Corino, M. W. Rivolta, R. Sassi, F. Lombardi, and L. T. Mainardi, "Ventricular activity cancellation in electrograms during atrial fibrillation with constraints on residuals' power," *Medical Engineering & Physics*, vol. 35, no. 12, pp. 1770–1777, 2013.
- [52] L. Sörnmo, A. Petrėnas, and V. Marozas, *Atrial fibrillation from an engineering perspective*. Springer, 2018.
- [53] A. Petrenas, V. Marozas, L. Sornmo, and A. Lukosevicius, "An echo state neural network for QRST cancellation during atrial fibrillation," *IEEE Trans. Biomed. Eng.*, vol. 59, no. 10, pp. 2950–2957, 2012.
- [54] F. Castells, P. Laguna, L. Sörnmo, A. Bollmann, and J. M. Roig, "Principal component analysis in ECG signal processing," *EURASIP Journal on Advances in Signal Processing*, vol. 2007, pp. 1–21, 2007.
- [55] J. J. Rieta, F. Castells, C. Sánchez, V. Zarzoso, and J. Millet, "Atrial activity extraction for atrial fibrillation analysis using blind source separation," *IEEE Trans. Biomed. Eng.*, vol. 51, no. 7, pp. 1176–1186, 2004.
- [56] F. Castells, J. Igual, J. Millet, and J. J. Rieta, "Atrial activity extraction from atrial fibrillation episodes based on maximum likelihood source separation," *Signal Processing*, vol. 85, no. 3, pp. 523–535, 2005.
- [57] M. Stridh and L. Sornmo, "Spatiotemporal QRST cancellation techniques for analysis of atrial fibrillation," *IEEE Trans. Biomed. Eng.*, vol. 48, no. 1, pp. 105– 111, 2001.
- [58] P. Escribano, J. Rodenas, M. Garcia, M. A. Arias, V. M. Hidalgo, S. Calero, J. J. Rieta, and R. Alcaraz, "Preoperative prediction of catheter ablation outcome in persistent atrial fibrillation patients through spectral organization analysis of the surface fibrillatory waves," *Journal of Personalized Medicine*, vol. 12, no. 10, p. 1721, 2022.
- [59] T. A. Lankveld, S. Zeemering, H. J. Crijns, and U. Schotten, "The ECG as a tool to determine atrial fibrillation complexity," *Heart*, vol. 100, no. 14, pp. 1077–1084, 2014.

- [60] M. Thurmann and J. G. Janney Jr, "The diagnostic importance of fibrillatory wave size," *Circulation*, vol. 25, no. 6, pp. 991–994, 1962.
- [61] R. H. Peter, J. J. Morris Jr, and H. D. McIntosh, "Relationship of fibrillatory waves and P waves in the electrocardiogram," *Circulation*, vol. 33, no. 4, pp. 599–606, 1966.
- [62] T. X. Zhao, C. A. Martin, J. P. Cooper, and P. R. Gajendragadkar, "Coarse fibrillatory waves in atrial fibrillation predict success of electrical cardioversion," *Annals of Noninvasive Electrocardiology*, vol. 23, no. 4, p. e12528, 2018.
- [63] M. Meo, V. Zarzoso, O. Meste, D. G. Latcu, and N. Saoudi, "Spatial variability of the 12-lead surface ECG as a tool for noninvasive prediction of catheter ablation outcome in persistent atrial fibrillation," *IEEE Trans. Biomed. Eng.*, vol. 60, no. 1, pp. 20–27, 2012.
- [64] Q. Xi, A. V. Sahakian, J. Ng, and S. Swiryn, "Atrial fibrillatory wave characteristics on surface electrogram: ECG to ECG repeatability over twenty-four hours in clinically stable patients," *Journal of cardiovascular electrophysiology*, vol. 15, no. 8, pp. 911–917, 2004.
- [65] Q. Xi, A. V. Sahakian, T. G. Frohlich, J. Ng, and S. Swiryn, "Relationship between pattern of occurrence of atrial fibrillation and surface electrocardiographic fibrillatory wave characteristics," *Heart Rhythm*, vol. 1, no. 6, pp. 656–663, 2004.
- [66] A. Bollmann, D. Husser, L. Mainardi, F. Lombardi, P. Langley, A. Murray, J. J. Rieta, J. Millet, S. B. Olsson, M. Stridh, *et al.*, "Analysis of surface electrocardiograms in atrial fibrillation: techniques, research, and clinical applications," *Europace*, vol. 8, no. 11, pp. 911–926, 2006.
- [67] J. Ng and J. J. Goldberger, "Understanding and interpreting dominant frequency analysis of af electrograms," *Journal of cardiovascular electrophysiology*, vol. 18, no. 6, pp. 680–685, 2007.
- [68] S. A. Sheikh, A. Z. Majoka, K. U. Rehman, N. Razzaq, and T. Zaidi, "Non-parametric spectral estimation technique to estimate dominant frequency for atrial fibrillation detection," *Journal of signal and information processing*, vol. 6, no. 4, pp. 266–276, 2015.
- [69] P. G. Platonov, V. D. Corino, M. Seifert, F. Holmqvist, and L. Sörnmo, "Atrial fibrillatory rate in the clinical context: natural course and prediction of intervention outcome," *Europace*, vol. 16, no. suppl\_4, pp. iv110–iv119, 2014.

[70] M. Stridh, L. Sornmo, C. J. Meurling, and S. B. Olsson, "Characterization of atrial fibrillation using the surface ECG: time-dependent spectral properties," *IEEE Trans. Biomed. Eng.*, vol. 48, no. 1, pp. 19–27, 2001.

- [71] C. Vayá and J. J. Rieta, "Time and frequency series combination for non-invasive regularity analysis of atrial fibrillation," *Medical & biological engineering & computing*, vol. 47, no. 7, pp. 687–696, 2009.
- [72] S. Quian and D. Chen, "Joint time-frequency analysis. methods and applications," *Prentince–Hall PTR, New York*, 1996.
- [73] L. Cohen, "Time-frequency analysis," Englewood Cliffs, 1995.
- [74] M. Stridh, L. Sornmo, C. J. Meurling, and S. B. Olsson, "Sequential characterization of atrial tachyarrhythmias based on ECG time-frequency analysis," *IEEE Trans. Biomed. Eng.*, vol. 51, no. 1, pp. 100–114, 2004.
- [75] J. Van Zaen, L. Uldry, C. Duchêne, Y. Prudat, R. A. Meuli, M. M. Murray, and J.-M. Vesin, "Adaptive tracking of EEG oscillations," *Journal of neuroscience methods*, vol. 186, no. 1, pp. 97–106, 2010.
- [76] A. Buttu, E. Pruvot, J. Van Zaen, A. Viso, A. Forclaz, P. Pascale, S. M. Narayan, and J.-M. Vesin, "Adaptive frequency tracking of the baseline ECG identifies the site of atrial fibrillation termination by catheter ablation," *Biomedical Signal Processing and Control*, vol. 8, no. 6, pp. 969–980, 2013.
- [77] P. Bonizzi, M. de la Salud Guillem, A. M. Climent, J. Millet, V. Zarzoso, F. Castells, and O. Meste, "Noninvasive assessment of the complexity and stationarity of the atrial wavefront patterns during atrial fibrillation," *IEEE Trans. Biomed. Eng.*, vol. 57, no. 9, pp. 2147–2157, 2010.
- [78] R. Alcaraz and J. J. Rieta, "Application of wavelet entropy to predict atrial fibrillation progression from the surface ECG," *Computational and mathematical methods in medicine*, vol. 2012, no. 1, p. 245213, 2012.
- [79] S. Muengtaweepongsa, R. Sungnoon, and T. Ngarmukos, "Increased sample entropy and high heart rate variability fluctuation in persistent atrial fibrillation as compared with paroxysmal atrial fibrillation: A matched case-control study," *Journal of Cardiovascular Disease Research*, vol. 12, no. 1, pp. 125–133, 2021.
- [80] M. Julián, R. Alcaraz, and J. Rieta, "Comparative assessment of nonlinear metrics to quantify organization-related events in surface electrocardiograms of atrial fibrillation," *Computer Methods and Programs in Biomedicine*, vol. 113, no. 2, pp. 420–429, 2014.

- [81] T. Inouye, K. Shinosaki, H. Sakamoto, S. Toi, S. Ukai, A. Iyama, Y. Katsuda, and M. Hirano, "Quantification of EEG irregularity by use of the entropy of the power spectrum," *Electroencephalography and clinical neurophysiology*, vol. 79, no. 3, pp. 204–210, 1991.
- [82] S. M. Pincus, "Approximate entropy as a measure of system complexity.," *Proceedings of the national academy of sciences*, vol. 88, no. 6, pp. 2297–2301, 1991.
- [83] R. Alcaraz and J. J. Rieta, "A review on sample entropy applications for the non-invasive analysis of atrial fibrillation electrocardiograms," *Biomedical Signal Processing and Control*, vol. 5, no. 1, pp. 1–14, 2010.
- [84] A. Molina-Picó, D. Cuesta-Frau, M. Aboy, C. Crespo, P. Miró-Martínez, and S. Oltra-Crespo, "Comparative study of approximate entropy and sample entropy robustness to spikes," *Artificial Intelligence in Medicine*, vol. 53, no. 2, pp. 97–106, 2011.
- [85] J. S. Richman and J. R. Moorman, "Physiological time-series analysis using approximate entropy and sample entropy," *American journal of physiology-heart and circulatory physiology*, vol. 278, no. 6, pp. H2039–H2049, 2000.
- [86] R. Alcaraz and J. J. Rieta, "Sample entropy of the main atrial wave predicts spontaneous termination of paroxysmal atrial fibrillation," *Medical Engineering & Physics*, vol. 31, no. 8, pp. 917–922, 2009.
- [87] A. L. Goldberger, L. A. N. Amaral, L. Glass, J. M. Hausdorff, P. C. Ivanov, R. G. Mark, J. E. Mietus, G. B. Moody, C.-K. Peng, and H. E. Stanley, "PhysioBank, PhysioToolkit, and PhysioNet: Components of a new research resource for complex physiologic signals," *Circulation*, vol. 101, no. 23, pp. e215–e220, 2000.
- [88] F. Sandberg, M. Stridh, and L. Sornmo, "Frequency tracking of atrial fibrillation using hidden markov models," *IEEE Trans. Biomed. Eng.*, vol. 55, no. 2, pp. 502–511, 2008.
- [89] R. Sassi, V. D. Corino, and L. T. Mainardi, "Analysis of surface atrial signals: time series with missing data?," *Annals of biomedical engineering*, vol. 37, no. 10, pp. 2082–2092, 2009.
- [90] M. Abdollahpur, G. Engström, P. G. Platonov, and F. Sandberg, "A subspace projection approach to quantify respiratory variations in the f-wave frequency trend," *Frontiers in Physiology*, vol. 13, p. 976925, 2022.

[91] M. Henriksson, A. Petrėnas, V. Marozas, F. Sandberg, and L. Sörnmo, "Model-based assessment of f-wave signal quality in patients with atrial fibrillation," *IEEE Trans. Biomed. Eng.*, vol. 65, no. 11, pp. 2600–2611, 2018.

- [92] G. B. Moody, R. G. Mark, A. Zoccola, and S. Mantero, "Derivation of respiratory signals from multi-lead ECGs," *Computers in cardiology*, vol. 12, no. 1985, pp. 113–116, 1985.
- [93] J. Lázaro, A. Alcaine, D. Romero, E. Gil, P. Laguna, E. Pueyo, and R. Bailón, "Electrocardiogram derived respiratory rate from QRS slopes and R-wave angle," *Annals of biomedical engineering*, vol. 42, no. 10, pp. 2072–2083, 2014.
- [94] S. Kontaxis, J. Lázaro, V. D. Corino, F. Sandberg, R. Bailón, P. Laguna, and L. Sörnmo, "ECG-derived respiratory rate in atrial fibrillation," *IEEE Trans. Biomed. Eng.*, vol. 67, no. 3, pp. 905–914, 2019.
- [95] R. Bailón, L. Sornmo, and P. Laguna, "A robust method for ECG-based estimation of the respiratory frequency during stress testing," *IEEE Trans. Biomed. Eng.*, vol. 53, no. 7, pp. 1273–1285, 2006.
- [96] R. Sameni, C. Jutten, and M. B. Shamsollahi, "Multichannel electrocardiogram decomposition using periodic component analysis," *IEEE Trans. Biomed. Eng.*, vol. 55, no. 8, pp. 1935–1940, 2008.
- [97] J. Lázaro, E. Gil, R. Bailón, A. Mincholé, and P. Laguna, "Deriving respiration from photoplethysmographic pulse width," *Med. Biol. Eng. Comput.*, vol. 51, no. 1-2, pp. 233–242, 2013.
- [98] F. Sandberg, M. Holmer, and B. Olde, "Monitoring respiration using the pressure sensors in a dialysis machine," *Physiol. Meas.*, vol. 40, no. 2, p. 025001, 2019.
- [99] C.-I. Chang, "Orthogonal subspace projection (OSP) revisited: A comprehensive study and analysis," *IEEE Trans. Geosci. Remote Sens.*, vol. 43, no. 3, pp. 502–518, 2005.
- [100] C. Varon, J. Lázaro, J. Bolea, A. Hernando, J. Aguiló, E. Gil, S. Van Huffel, and R. Bailón, "Unconstrained estimation of HRV indices after removing respiratory influences from heart rate," *IEEE J. Biomed. Health Inform.*, vol. 23, no. 6, pp. 2386–2397, 2018.
- [101] S. Schulz, F.-C. Adochiei, I.-R. Edu, R. Schroeder, H. Costin, K.-J. Bär, and A. Voss, "Cardiovascular and cardiorespiratory coupling analyses: a review,"

- Philos. Trans. R. Soc. A Math. Phys. Eng. Sci., vol. 371, no. 1997, p. 20120191, 2013.
- [102] H. Hilmisson, R. J. Thomas, and S. Magnusdottir, "Cardiopulmonary coupling-calculated sleep stability and nocturnal heart rate kinetics as a potential indicator for cardiovascular health: a relationship with blood pressure dipping," *Frontiers in Sleep*, vol. 3, p. 1230958, 2024.
- [103] R. Steuer, J. Kurths, C. O. Daub, J. Weise, and J. Selbig, "The mutual information: detecting and evaluating dependencies between variables," *Bioinformatics*, vol. 18, no. suppl\_2, pp. S231–S240, 2002.
- [104] M. Henriksson, A. Petrenas, V. Marozas, F. Sandberg, and L. Sornmo, "Model-based assessment of f-wave signal quality in patients with atrial fibrillation," *IEEE Trans. Biomed. Eng.*, vol. 65, no. 11, pp. 2600–2611, 2018.
- [105] S. Östenson, V. D. Corino, J. Carlsson, and P. G. Platonov, "Autonomic influence on atrial fibrillatory process: head-up and head-down tilting," *Annals of Noninvasive Electrocardiology*, vol. 22, no. 2, p. e12405, 2017.

# Part II Included Papers

# $Paper\ I$





# Respiratory Induced Modulation in f-Wave Characteristics During Atrial Fibrillation

Mostafa Abdollahpur1\*, Fredrik Holmqvist2, Pyotr G. Platonov2 and Frida Sandberg1

<sup>1</sup> Department of Biomedical Engineering, Lund University, Lund, Sweden, <sup>2</sup> Department of Cardiology, Clinical Sciences, Lund University, Lund, Sweden

The autonomic nervous system (ANS) is an important factor in cardiac arrhythmia, and information about ANS activity during atrial fibrillation (AF) may contribute to personalized treatment. In this study we aim to quantify respiratory modulation in the f-wave frequency trend from resting ECG. First, an f-wave signal is extracted from the ECG by QRST cancelation. Second, an f-wave model is fitted to the f-wave signal to obtain a high resolution f-wave frequency trend and an index for signal quality control (S). Third, respiratory modulation in the f-wave frequency trend is extracted by applying a narrow band-pass filter. The center frequency of the band-pass filter is determined by the respiration rate. Respiration rate is estimated from a surrogate respiration signal, obtained from the ECG using homomorphic filtering. Peak conditioned spectral averaging, where spectra of sufficient quality from different leads are averaged, is employed to obtain a robust estimate of the respiration rate. The envelope of the filtered f-wave frequency trend is used to quantify the magnitude of respiratory induced f-wave frequency modulation. The proposed methodology is evaluated using simulated f-wave signals obtained using a sinusoidal harmonic model. Results from simulated signals show that the magnitude of the respiratory modulation is accurately estimated, quantified by an error below 0.01 Hz, if the signal quality is sufficient (S > 0.5). The proposed method was applied to analyze ECG data from eight pacemaker patients with permanent AF recorded at baseline, during controlled respiration, and during controlled respiration after injection of atropine, respectively. The magnitude of the respiratory induce f-wave frequency modulation was  $0.15\pm0.01$ ,  $0.18\pm0.02$ , and  $0.17\pm0.03$  Hz during baseline, controlled respiration, and post-atropine, respectively. Our results suggest that parasympathetic regulation affects the magnitude of respiratory induced f-wave frequency modulation.

### OPEN ACCESS

#### Edited by: Juan Pablo Martínez,

University of Zaragoza, Spain

#### Reviewed by:

Marianna Meo, EPD Solutions, a Philips Company, Netherlands Vessela Krasteva, Bulgarian Academy of Sciences, Bulgaria

#### \*Correspondence:

Mostafa Abdollahpur mostafa.abdollahpur@bme.lth.se

#### Specialty section:

This article was submitted to Cardiac Electrophysiology, a section of the journal Frontiers in Physiology

Received: 14 January 2021 Accepted: 12 March 2021 Published: 08 April 2021

#### Citation:

Abdollahpur M, Holmqvist F, Platonov PG and Sandberg F (2021) Respiratory Induced Modulation in f-Wave Characteristics During Atrial Fibrillation. Front. Physiol. 12:653492. doi: 10.3389/fphys.2021.653492 Keywords: atrial fibrillation, autonomic nervous system, ECG processing, f-wave frequency, parasympathetic regulation, respiratory modulation

#### 1. INTRODUCTION

Despite progress in atrial fibrillation (AF) treatment, such as ablation procedures, strokeprevention procedures, and anti-arrhythmic drugs, AF still is associated with significant mortality in middle-aged and older adults, and it constitutes a substantial burden to the health economy (Hindricks et al., 2020). The current estimate of AF prevalence for adults in the United States is ranged between 2 and 4% (Benjamin et al., 2019). The prevalence of AF increases with age and is

1

higher in men. In a Swedish study including 30,447 individuals, AF prevalence was 1.5% higher in men and increased from 2 per 1,000 in ages 45–49 to 29 per 1,000 in ages 70–74 (Smith et al., 2010). There are some substantial modifiers which contribute to the maintenance and progression of AF, such as atrial fibrosis and aging, ion-channel dysfunction, autonomic imbalance, and genetic background (Fabritz et al., 2016). Better understanding and monitoring of these AF-causing factors can contribute to personalized AF treatment.

Autonomic dysfunction is one of the main factors which can contribute to AF (Fabritz et al., 2016). The autonomic nervous system (ANS) plays an important role in cardiac arrhythmogenesis. Previous research has established an understanding of the cardiac ANS and provided evidence to support the relationship between autonomic tone and cardiac arrhythmia (Shen and Zipes, 2014). For example, low-level vagal stimulation has been shown to suppress AF episodes in ambulatory dogs (Shen et al., 2011). Further, experimental studies has shown that changes in sympathetic or parasympathetic tone may change the atrial action potential and refractory period (Liu and Nattel, 1997; Sharifov et al., 2004).

The atrial electrical activity during AF can be characterized from the f-waves in the ECG; f-wave amplitude, f-wave frequency, f-wave morphology, f-wave regularity, and f-wave complexity has been proposed for this purpose (Petrutiu et al., 2006; Meo et al., 2013; Lankveld et al., 2014; Sörnmo, 2018). Such f-wave characteristics has been suggested for prediction of treatment outcome, e.g., a low f-wave amplitudes predicted AF recurrence after catheter ablation in a study including 54 patients with persistent AF (Cheng et al., 2013), and large f-wave amplitude predicted termination of AF during catheter ablation in another study including 90 patients with persistent AF (Nault et al., 2009). Also, Lankveld et al. (2016) found the chances of successful in cather ablation in patients with persistent AF can be predicted by AF complexity and frequency parameters; the study included 91 patients for training of the prediction models and validated by 83 patients.

The f-wave frequency, often referred to as the atrial fibrillatory rate, has received considerable clinical attention (Platonov et al., 2014). Low f-wave frequency can predict successful outcome in patient with persistent AF undergoing cardioversion (Bollmann et al., 2008) and high f-wave frequency predicts early AF recurrence (Bollmann et al., 2003). The f-wave frequency can increase with the progression of AF, and patients with persistent AF often have a higher f-wave frequency than patients with paroxysmal AF (Alcaraz et al., 2011; Park et al., 2019). Further, it has been shown that a low f-wave frequency is associated with spontaneous conversion of recent-onset AF (Choudhary et al., 2013). However, the link between f-wave frequency and progression of disease is ambiguous since a low f-wave frequency is also associated with poor outcome in heart failure patients with long-standing AF (Platonov et al., 2012).

Previous studies have shown that the f-wave frequency can change in response to changes in autonomic tone. The f-wave frequency has been shown to increase in response to head-up tilt (Ingemansson et al., 1998; Östenson et al., 2017) and decrease in response to head-down tilt (Östenson et al., 2017). Further,

the f-wave frequency has been shown to follow a circadian pattern where it increases during daytime and decreases at night (Meurling et al., 2001; Sandberg et al., 2010). Controlled respiration can induce cyclic fluctuations in the f-wave frequency. Holmqvist et al. (2005) found that the spectral power of the f-wave frequency trend in the respiratory frequency band increased in response to controlled respiration and decreased in response to vagal blockade for eight patients with permanent AF. However, individual variations were large. In another study using a similar methodology, the f-wave frequency was influenced by controlled respiration and attenuated by the vagal blockade in only two out of eight patients with permanent AF (Stridh et al., 2003).

The aim of this study is to develop a methodology that can be used to quantify respiratory induced variations in the f-wave frequency from resting ECG. This is challenging, since (1) respiratory induced f-wave frequency modulation is very small and may be concealed by other variations and (2) the respiration rate is unknown and may vary over time. A preliminary version of this work, where the respiration rate was assumed to be known, was presented at the CinC conference 2020 (Abdollahpur et al., 2020). In contrast, the respiration rate in the present study is estimated from the ECG.

#### 2. MATERIALS AND METHODS

A schematic outline of the methodology is shown in **Figure 1**. An f-wave signal x(n) is extracted from the ECG by QRST cancelation (section 2.3). A model-based approach to f-wave characterization is applied to estimates an f-wave frequency trend  $\hat{f}(n)$  and a signal quality index S from x(n) (section 2.4). Respiratory modulation in  $\hat{f}(n)$  is estimated using a bandpass filtering approach (section 2.5). A respiration rate estimate  $\hat{f}_r(n)$ , which is required for the bandpass filtering, is derived from the ECG (section 2.6). The accuracy of the estimated respiratory modulation magnitude  $\Delta \hat{f}$  is evaluated using simulated f-wave signals  $x_{sim}(n)$  (section 2.1). Finally, the method is applied to analyse data from a clinical study (section 2.2).

#### 2.1. Simulated Data

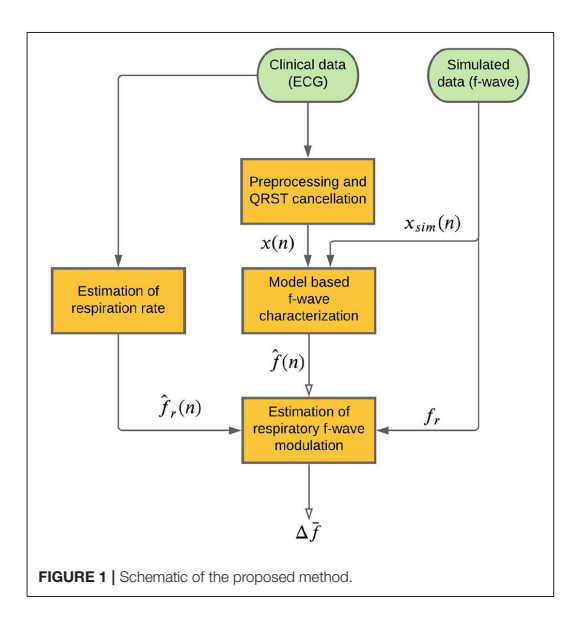
A modified version of the saw-tooth model (Stridh and Sörnmo, 2001) is used to simulate f-wave signals. The simulated f-waves consists of the sum of a sinusoid with time-varying frequency and its harmonic

$$x_{sim}(n) = \sum_{k=1}^{2} a_k(n) \sin(2\pi k f(n)n) + v(n)$$
 (1)

The time-varying frequency is given by

$$f(n) = \frac{f}{f_s} + \frac{\Delta f}{2\pi f_r n} \sin(2\pi n \frac{f_r}{f_s}) + \frac{\Phi(n)}{2\pi k n}$$
 (2)

where f defines the average fundamental frequency, and respiratory f-wave frequency modulation is quantified by  $f_r$  and  $\Delta f$ , defining the modulation frequency and the modulation magnitude, respectively. Random phase variation,  $\Phi(n)$ , is added



to account for other variations in the f-wave frequency; it is modeled as white Gaussian noise with standard deviation  $\sigma_{\Phi}$ . The amplitude of the kth harmonic is given by

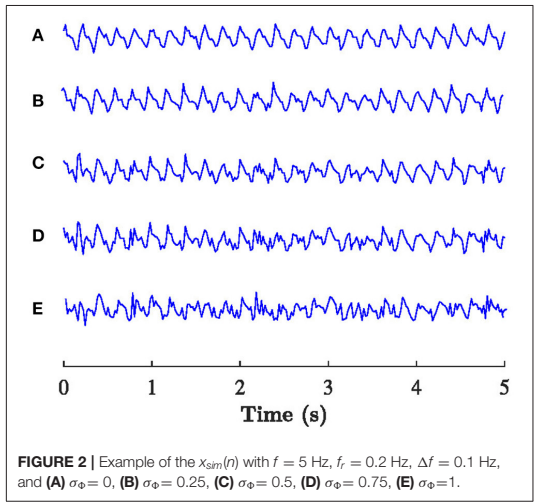
$$a_k(n) = \frac{2}{k\pi} \left( a + \Delta a(n) \right) \tag{3}$$

where a is the average f-wave amplitude, and  $\Delta a(n)$  quantifies random amplitude variation and is assumed to have a Gaussian distribution with mean zero and standard deviation a/5.

The following parameters are used for the simulations f-wave signals:  $f=\{5,6,7\}$  Hz,  $f_r=\{0.1,0.2,0.3\}$  Hz,  $\Delta f=\{0,0.1,0.2\}$  Hz, a chosen such that standard deviation of signal  $\sigma_x=50~\mu\text{V}$ , and  $\sigma_\Phi=\{0,0.25,0.5,0.75,1\}$ . White Gaussian noise v(n) with standard deviation of 0.1a is added to form realistic f-wave signals and the sampling frequency was set to  $f_s=50$ Hz. For each parameter setting 10 realizations of  $x_{sim}(n)$  were considered, resulting in a total of 1,350 simulated signals. Examples of  $x_{sim}(n)$  with different values of  $\sigma_\Phi$  are displayed in Figure 2.

#### 2.2. Clinical Data

The study population consists of eight pacemaker patients with permanent AF and complete atrioventricular block that participated in a clinical study (Holmqvist et al., 2005). The clinical characteristics of the study population is summarized in **Table 1**. The study was conducted in accordance with the Declaration of Helsinki, and the protocol was approved by the local Ethics Committee. All subjects gave their informed consent for inclusion before they participated in the study. The study protocol consisted of three phases; baseline rest (B), controlled respiration (CR), and controlled respiration following injection



of atropine to induce full vagal blockade (PA), respectively. Each phase lasted 5 min, and standard 12-lead ECG at 1 kHz sampling rate was recorded throughout the study protocol. During controlled respiration, the patients inhaled for 4 s and exhaled for 4 s, following instructions from the study nurse.

#### 2.3. Preprocessing and QRST Cancelation

Following preprocessing, atrial activity was extracted from ventricular activity in the ECG using a spatiotemporal QRST cancelation technique (Stridh and Sörnmo, 2001). Briefly, a scaled, spatial, and temporally aligned average QRS complexes is subtracted from each QRS complex in the ECG, the Cardiolund ECG Parser was used for this task. Since the resulting f-wave signal has negligible frequency content above 25 Hz, it was downsampled to 50 Hz. In the present study, the extracted f-wave signal from lead V1 was subjected to analysis; this signal is denoted x(n).

#### 2.4. Model Based f-Wave Characterization

The harmonic f-wave model (Henriksson et al., 2018) is employed to estimate the local f-wave frequency, phase, and amplitude. In this model, f-waves are formulated by the complex signal  $s(n; \theta)$ , defined as the sum of a complex exponential signal with fundamental frequency f and its second harmonic,

$$s(n;\theta) = \sum_{m=1}^{2} A_m e^{j(m2\pi \frac{f}{f_s}n + \phi_m)}$$
 (4)

where  $A_m$  and  $\phi_m$  define the amplitude and phase, respectively, of the m:th harmonic, and  $f_s$  is sampling frequency of x(n).

The model is fitted to the complex-valued analytic representation of x(n), denoted  $x_a(n)$ , and obtained using Hilbert transformation. The parameter vector

TABLE 1 | Patient characteristics.

Patient	Age, yr	Gender	EF,%	Left atrial diameter (mm)	AF duration, mo	Number of cardioversions	Heart active drugs	Comorbidity
a	62	Female	55	41	7	10	Diltiazem	None
b	64	Male	45	43	5	15	None	COPD
С	65	Female	35	37	9	4	Metoprolol	HT, CHF
d	64	Female	55	32	30	4	None	None
е	54	Male	55	46	24	7	Losartan	None
f	59	Male	55	53	32	10	Losartan	HT
g	68	Female	55	45	7	26	Spironolactone	None
h	53	Male	55	32	24	7	Enalapril	HT
Gross average	61 ± 5		51 ± 7	41 ± 7	17 ± 11	10 ± 7		

CHF, chronic heart failure; COPD, chronic obstructive pulmonary disease; EF, ejection fraction; HT, hypertension

 $\theta = [f \ A_1 \ A_2 \ \phi_1 \ \phi_2]^T$  is estimated using a maximum likelihood approach

$$\hat{\theta} = \arg\min_{a} ||x_a(n) - s(n; \theta)||^2$$
 (5)

The model is fitted to 20 ms overlapping 0.5 s segments of  $x_a(n)$ ; the local estimates  $\hat{f}$  results in an f-wave frequency trend  $\hat{f}(n)$  sampled at 50 Hz.

In the present study, we analyse 5 min recordings obtained during stable conditions and therefore we assume that the f-wave frequency will not change drastically within the recording. Hence, the local estimation of  $\hat{f}$  is constrained to the interval  $|\hat{f}_0 - 1.5, \hat{f}_0 + 1.5|$  Hz, where  $\hat{f}_0$  is an initial f-wave frequency estimate determined by the maximum spectral peak in the interval [4, 12] Hz of the Welch periodogram of the entire recording x(n).

The model error  $\hat{e}(n) = x_a(n) - s(n; \hat{\theta})$  is used to estimate a signal quality index,

$$S = 1 - \frac{\sigma_{\hat{e}}}{\sigma_{x_*}} \tag{6}$$

where  $\sigma_{\hat{e}}$  and  $\sigma_{x_a}$  denote the standard deviation of  $\hat{e}(n)$  and  $x_a(n)$ , respectively (Henriksson et al., 2018). For any reasonable estimate of  $s(n; \hat{\theta})$ , S is limited to the interval [0, 1], where one represents the best model fit. A poor model fit, quantified by a low value of S suggests that the parameter estimates  $\hat{\theta}$  are unreliable. In the present study, S is estimated based on the entire 5-min recording.

## 2.5. Estimation of Respiratory f-Wave Modulation

A forth-order Butterworth band pass filter with a fixed bandwidth  $\beta$  (Raja Kumar and Pal, 1985) and a center frequency determined by the respiration rate  $\hat{f}_r(n)$  is employed to extract respiratory modulation in  $\hat{f}(n)$ . The bandwidth of filter is set to 0.06 Hz since the magnitude of respiration rate estimation error is expected to

be constrained to this range (Kontaxis et al., 2020). The transfer function of the filter is given by

$$H(z) = \frac{a_0 + a_2 z^{-2} + a_4 z^{-4}}{1 + b_1 W z^{-1} + (b_2 W^2 + b_2 t) z^{-2} + b_3 W z^{-3} + b_4 z^{-4}}$$
(7)

where the coefficients are given by

$$a_{0} = 1/(k^{2} + \sqrt{2}k + 1)$$

$$a_{2} = -2a_{0}$$

$$a_{4} = a_{0}$$

$$b_{1} = -2k(2k + \sqrt{2})a_{0}$$

$$b_{2} = 4k^{2}a_{0}$$

$$b_{2}' = 2(k^{2} - 1)a_{0}$$

$$b_{3} = 2k(-2k + \sqrt{2})a_{0}$$

$$b_{4} = (k^{2} - \sqrt{2}k + 1)a_{0}$$

$$(8)$$

and k and W are given by

$$k = \cot(\pi \beta / f_s)$$

$$W = \frac{\cos(2\pi f_r / f_s)}{\cos(\pi \beta / f_s)}$$
(9)

respectively. The output of the filter is denoted  $\tilde{f}(n)$ . An estimate of the magnitude of the respiratory f-wave frequency modulation is given by the envelope of  $\tilde{f}(n)$ , obtained as the magnitude of its analytic equivalent using Hilbert transformation. The estimate is denoted  $\Delta \hat{f}(n)$ . Since  $\Delta \hat{f}(n)$  varies over time, we use its 5 min average  $\Delta f$  to quantify the magnitude of respiratory f-wave frequency modulation in this study.

#### 2.6. Estimation of Respiration Rate

A surrogate respiration signal is derived from the ECG leads (V1, V2, V3, V4, V5, V6, I, II, III) by using homomorphic filtering to extract slow variations in the amplitudes (Rezek and

Roberts, 1998). First, the ECG signal is decimated to 50 Hz and a zero-phase first-order Butterworth low-pass filter with a cut-off frequency of 2 Hz is applied to emphasize slow variation

in the ECG amplitude caused by chest movements during the respiratory cycle. Then, the peak envelope of the filtered ECG signal is determined and smoothed using a Savitzky-Golay filter

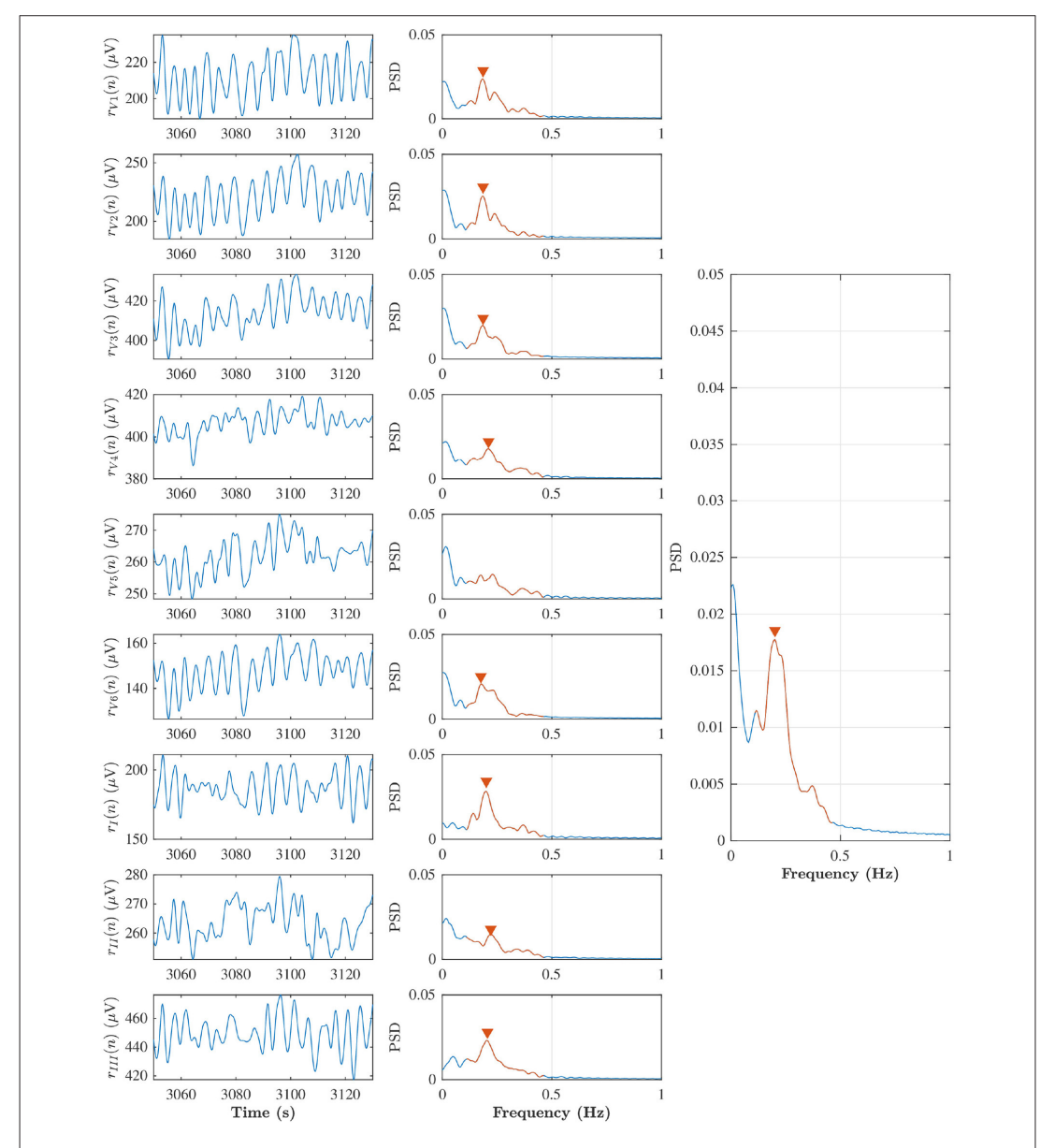


FIGURE 3 | Left subplots indicate  $r_i(n)$  from lead V1, V2, V3, V4, V5, V6, I, II, and III during baseline in the patient (b), and middle subplots are corresponding Welch periodogram. The prominent peak in the respiratory interval (red solid line) is shown with red marker. The averaged spectra and respiration rate estimate can be seen in the right subplot.

with polynomial order four and frame length 251 corresponding to 5 s, and the resulting envelope is down-sampled to 5 Hz. A similar approach is applied separately to each ECG lead; the surrogate respiration signal obtained from lead l is denoted  $r_l(n)$ . A robust estimate of the respiration rate is obtained by combining  $r_l(n)$  obtained from all ECG leads using peak conditioned spectral averaging (Bailón et al., 2006; Lázaro et al., 2013; Sandberg et al., 2019). In this technique, Welch periodograms are estimated from sliding segments of  $r_l(n)$  from each lead, and periodograms of sufficient quality are averaged to produce a power spectrum from which the respiration rate can be estimated more robustly. In the present study, Welch periodograms were computed based on 80 s sliding 75 s overlapping segments of  $r_l(n)$ , by averaging power spectra of 50% overlapping 24 s subintervals. A periodogram is considered to be of sufficient quality if it has a prominent peak in the respiratory interval, defined by at least 85% of the maximal peak height in the spectrum. The respiration rate estimates obtained from the averaged spectra every 5 s are denoted  $\hat{f}_r(n)$ . An example of  $r_l(n)$ , corresponding Welch periodograms, and averaged power spectra obtained from an 80 s time segment from patient b in phase B, is displayed in Figure 3. In this example, the average spectrum used for respiration rate estimation is based on all leads except lead V5, for which the periodogram was considered of insufficient quality.

#### 3. RESULTS

The estimation accuracy of  $\Delta \bar{f}$  is evaluated using simulations and the estimation accuracy of  $\hat{f}_r(n)$  is evaluated using the CR and PA phases of the clinical data for which the respiration rate is known. Finally, results from analysis of clinical data during B, CR, and PA are presented.

## 3.1. Estimation Accuracy of Respiratory f-Wave Modulation

Signal quality S and  $\Delta \bar{f}$  were estimated from the simulated fwave signals using the methods described in sections 2.4 and 2.5, respectively. The sampling frequency  $f_s$  in Equation (4) was set to 50 Hz to match the sampling frequency of the simulated f-wave signals. The respiration rate used for the band-pass filtering was set to  $f_r$  as used for the corresponding simulation. Results from the analysis of simulated data are presented in **Figure 4**, **5**. **Figure 4** shows that S decreases with increasing  $\sigma_{\Phi}$ independently of the other parameter settings. The estimation error, quantified by the absolute difference between  $\Delta f$  and  $\Delta f$  is displayed in Figure 5. Results suggest that  $\Delta f$  can be accurately estimated if  ${\cal S}$  is above  $\Gamma_{\cal S}\,=\,0.5;\,95\%$  of the estimates has an error below 0.01 Hz if  $\mathcal{S} > 0.5$ . For  $\mathcal{S} < 0.5$  the estimation error becomes large which indicates that the estimate  $\Delta \bar{f}$  is unreliable. Hence a threshold of  $\Gamma_{\mathcal{S}}=0.5$  was used to determine if the signal quality is sufficient for analysis.

## 3.2. Estimation of Respiration Rate in Clinical Data

Respiration rate  $f_r(n)$  was estimated from the clinical dataset using the method described in section 2.6. **Table 2** summarizes

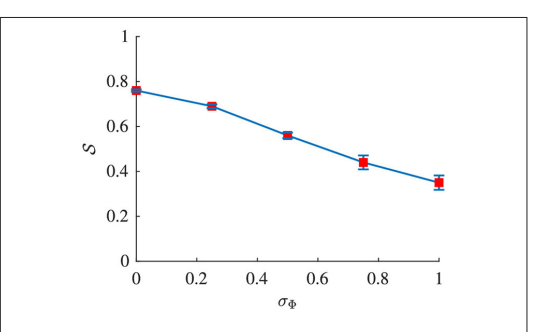


**FIGURE 4** | Signal quality S of  $x_{sim}(n)$  plotted vs.  $\sigma_{\Phi}$ . Red dots indicate the mean and blue whiskers indicate the std of S.

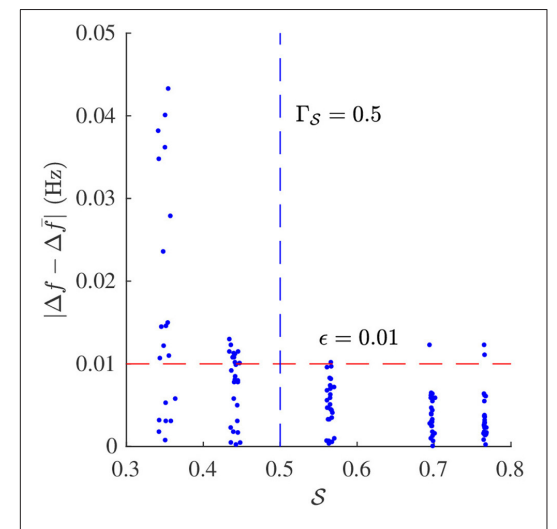


**FIGURE 5** | Estimation error  $|\Delta \bar{f} - \Delta f|$  and corresponding signal quality S of  $x_{\rm sim}(n)$ .

the estimated respiration rates  $\hat{f}_r(n)$  for each patient during B, CR, and PA, respectively. The standard deviation of  $\hat{f}_r(n)$  within each recording is smaller than the bandwidth of the filter  $\beta$ , implying that the center frequency  $f_r$  can be fixed to the mean  $\bar{f}_r$ .

The estimation accuracy of  $\hat{f}_r(n)$  was evaluated on the CR and PA phases, for which the respiration rate is known to be 0.125 Hz. In all patients except one,  $\hat{f}_r(n)$  gave an accurate estimate of the true respiration rate in the CR and PA phases (see **Table 2**). It should be noted that patient b, for which  $\hat{f}_r(n)$  did not correspond to 0.125 Hz in CR and PA, has a considerable amount of ectopic beats, which may explain why the respiration rate estimation failed. This patient was excluded from further analysis.

**TABLE 2** | Estimated respiration rate  $\hat{t}_r(n)$  (mean  $\pm$  std) for B, CR, and P, respectively.

Patient	$\hat{f}_{r_B}$ (Hz)	$\hat{f}_{r_{CR}}$ (Hz)	$\hat{f}_{r_{PA}}$ (Hz)	
a	0.268 ± 0.007	0.125 ± 0.000	0.125 ± 0.000	
b	$0.252 \pm 0.006$	$0.162 \pm 0.000^{*}$	$0.180 \pm 0.056^{*}$	
С	$0.208 \pm 0.008$	$0.125 \pm 0.000$	$0.125 \pm 0.000$	
d	$0.215 \pm 0.007$	$0.125 \pm 0.000$	$0.125 \pm 0.001$	
е	$0.232 \pm 0.003$	$0.125 \pm 0.000$	$0.125 \pm 0.000$	
f	$0.308 \pm 0.002$	$0.125 \pm 0.000$	$0.125 \pm 0.000$	
g	$0.232 \pm 0.019$	$0.125 \pm 0.000$	$0.125 \pm 0.000$	
h	$0.163 \pm 0.003$	$0.125 \pm 0.000$	$0.125 \pm 0.000$	
Gross average	0.235 ± 0.043	0.129 ± 0.013	0.131 ± 0.019	

<sup>\*</sup>Indicates that  $\hat{f}_r(n)$  differed significantly from the true respiration rate.

# 3.3. Estimation of Respiratory f-Wave Modulation in Clinical Data

The methodology as described in sections 2.3–2.6 was applied to analyze the clinical data described in section 2.2. The sampling frequency  $f_s$  in Equation (4). was set to 50 Hz to match the sampling frequency of the f-wave signals. **Figure 6** illustrates the signals obtained in each step of the analysis for patient b in phase B.

The signal quality was sufficient for analysis ( $S > \Gamma_S$ ) in all recordings except one. The mean and standard deviation of  $\hat{f}(n)$ and  $\Delta \hat{f}(n)$  are shown in the **Table 3**. A Kruskal-Wallis test with Dunn-Sidak correction was applied to analyze if the differences between phases for each patient were significant. Results indicate that  $\Delta \hat{f}(n)$  was significantly larger in CR than in B for all patients, and that  $\Delta \hat{f}(n)$  was significantly smaller in PA than in CR for four patients (p < 0.05). For  $\hat{f}(n)$  the results were more heterogeneous;  $\hat{f}(n)$  was significantly larger in CR than in B for three patients and significantly smaller in CR than in B for three patients (p < 0.05). Further,  $\hat{f}(n)$  was significantly larger in PA than in CR for four patients and significantly smaller in PA than in CR for three patients (p < 0.05). The gross average  $\Delta \hat{f}$  was  $0.15 \pm 0.01$ Hz (mean $\pm$ std) during B, 0.18  $\pm$  0.02 Hz during CR, 0.17  $\pm$  0.03 Hz during PA. There is a trend toward increased  $\Delta \bar{f}$  during CR and decreased  $\Delta f$  during PA (see **Figure 7**). A Friedman test was applied to analyze if the differences in  $\Delta f$  between B, CR, and PA were significant. Results indicate that only the changes between B and CR are significant.

The modulation magnitude  $\Delta \bar{f}$  is plotted vs. the average  $\hat{f}(n)$ , denoted  $\bar{f}$ , in **Figure 8**. There is no correlation between  $\Delta \bar{f}$  and  $\bar{f}$  in any of the phases.

# 4. DISCUSSION

The aim of the study was to develop a method to quantify respiratory modulation in the f-wave frequency. Simulation

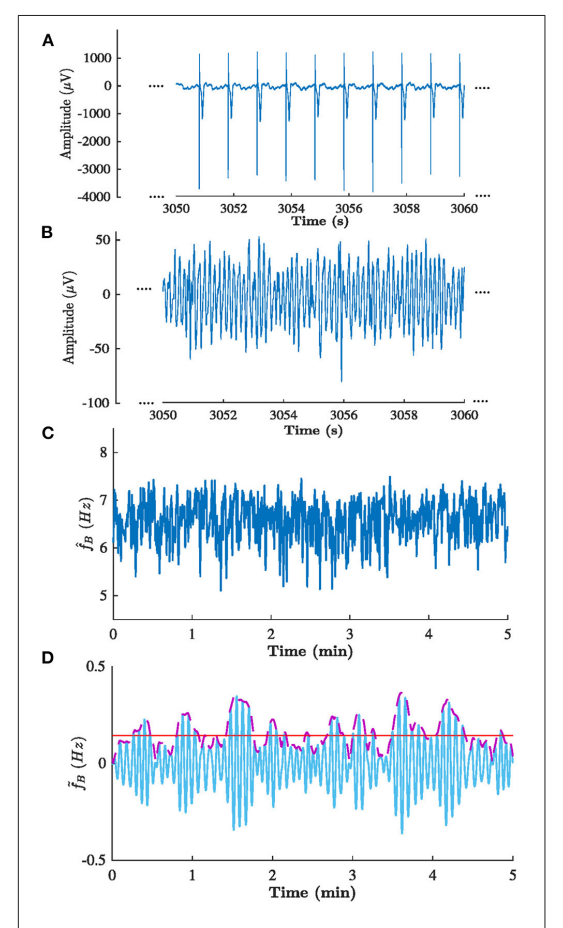


**FIGURE 6** | Signals obtained in each step of the analysis of patient b in phase B. (A) ECG from lead V1, (B) corresponding extracted f-waves  $\kappa(n)$ , (C) estimated f-wave frequency trend  $\hat{f}(n)$ , and (D) corresponding (solid blue) filtered  $\hat{f}(n)$ , (dashed purple)  $\Delta \hat{f}(n)$ , and (solid red) estimated  $\Delta \hat{f}$ . Note the that (A,B) shows 10 s excerpts of the signals, whereas (C,D) shows the full 5 min signal.

results shows that the method works accurately provided that the signal quality is sufficient (cf. **Figure 5**). Our results from analysis of clinical data suggest that the magnitude of the respiratory f-wave frequency modulation provide complementary information to the average f-wave frequency (cf. **Figure 8**).

In previous studies that have investigated respiratory modulation in the f-wave frequency, a spectral approach was used (Stridh et al., 2003; Holmqvist et al., 2005). In this study, we use a recently proposed model-based approach that allows more detailed f-wave characterization and provides a signal quality metric  $\mathcal{S}$  that can be used to exclude unreliable frequency estimates caused by artifacts in the f-wave signal (Henriksson

 $6.88 \pm 0.71$ 

Gross average

Patient	$\Delta \hat{f}_B(n)(Hz)$	$\Delta \hat{f}_{CR}(n)(Hz)$	$\Delta \hat{f}_{PA}(n)(Hz)$	$\hat{f}_B(n)(Hz)$	$\hat{f}_{CR}(n)(Hz)$	$\hat{f}_{PA}(n)(Hz)$
a	0.16 ± 0.06	0.17 ± 0.09*	0.16 ± 0.08°	$6.84 \pm 0.43$	6.77 ± 0.45*	6.71 ± 0.41**
С	$0.13 \pm 0.06$	$0.16 \pm 0.08^*$	0.13 ± 0.07°	$6.17 \pm 0.35$	$6.31 \pm 0.37^*$	$6.46 \pm 0.36^{\bullet*}$
d	$0.16 \pm 0.08$	$0.17 \pm 0.08^{*}$	$0.14 \pm 0.07^{\bullet*}$	$6.57 \pm 0.43$	$6.75 \pm 0.39^*$	6.36 ± 0.43**
fe	$0.16 \pm 0.08$	$0.19 \pm 0.10^{*}$	$0.19 \pm 0.10^{*}$	$7.68 \pm 0.51$	$7.39 \pm 0.54$ *	$7.57 \pm 0.54^{\bullet*}$
f	$0.14 \pm 0.07$	$0.21 \pm 0.10^{*}$	$0.21 \pm 0.12^*$	$7.46 \pm 0.46$	$7.29 \pm 0.49^*$	$7.14 \pm 0.48^{\bullet*}$
g	_	$0.17 \pm 0.08$	0.16 ± 0.08°	_	$5.91 \pm 0.41$	$5.96 \pm 0.42$
h	$0.15 \pm 0.08$	0.17 ± 0.07*	0.17 ± 0.07*	$7.73 \pm 0.43$	8.11 ± 0.44*	7.98 ± 0.43**

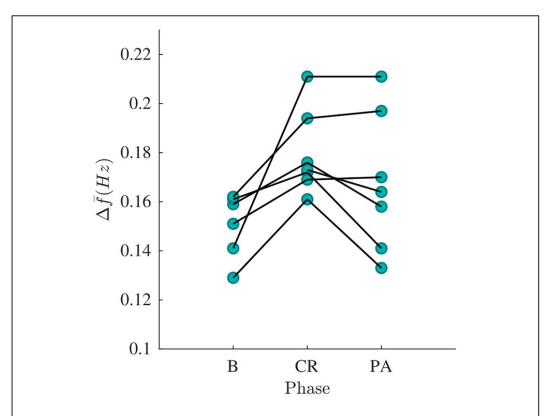
**TABLE 3** | Estimated f-wave frequency  $\hat{f}(n)$  and respiratory frequency modulation  $\Delta \hat{f}(n)$  (mean  $\pm$  std) from clinical data.

 $0.18 \pm 0.02$ 

Subscripts (B, CR, PA) indicates phase of recording, (\*) indicates significant differences to B and (\*) indicates significant differences to CR. The phase B recording from patient g was excluded from analysis due insufficient signal quality (S < \Gamma\_S).

 $0.17 \pm 0.03$ 

 $7.07 \pm 0.64$ 



 $0.15 \pm 0.01$ 

**FIGURE 7** |  $\Delta \bar{t}$  estimated from phase B, CR, and PA recordings, respectively. Each curve corresponds to a patient.

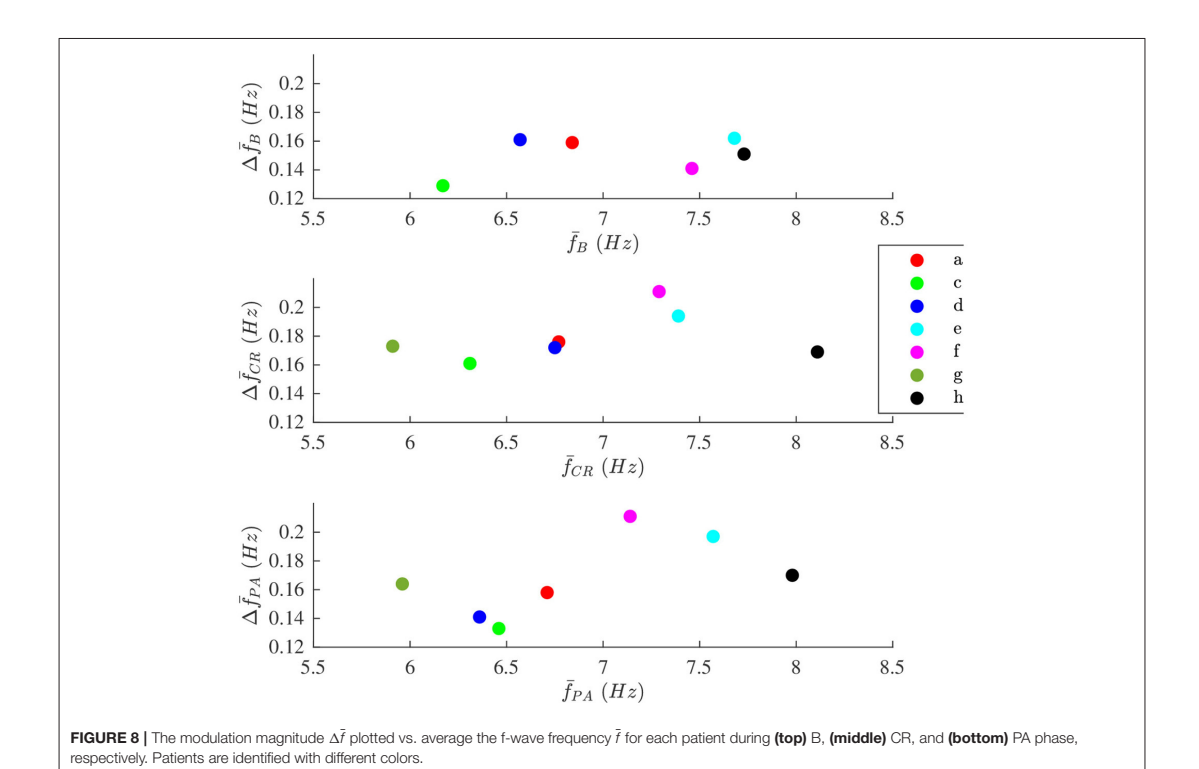
et al., 2018). It should be noted that the settings in the present study were different from the ones used in Henriksson et al. (2018), to facilitate analysis of respiratory modulation in f-wave frequency trend. Since the recordings in the present study were obtained during stationary conditions, the initial frequency estimate was based on the entire 5 min recording rather than on 5 s segments of the recording. Further, we allowed a larger local frequency deviation from the initial estimate; 1.5 Hz rather than 0.25 Hz. In Henriksson et al. (2018), it was shown that  ${\cal S}$ larger than 0.3 was sufficient for accurate estimation of f(n). Our simulation results indicate that a similar S is required for accurate estimation of the average f-wave frequency with the present settings. Analysis of small variations in the frequency trend, however, requires better signal quality, and our simulation results indicate that S larger than 0.5 is required for accurate estimation of respiratory f-wave frequency modulation.

The proposed methodology relies on ECG derived respiration rate estimation. It should be mentioned such estimation requires ECG length sufficiently long due to respiratory frequency during

baseline phase. If the respiration was known the method could be apply to shorter segment. Several methods have been proposed to extract respiratory information from the ECG. One of the most common approaches is to use respiratory sinus arrhythmia, i.e., respiratory induced variations in the heart rate (Charlton et al., 2018). However, such approach is not feasible during AF where the heart beats result from complex interactions between the atria and the atrioventricular node. Another approach is to use beat-to-beat morphological variations in the QRS complexes caused by chest movements, using e.g., vectorcardiogram loop analysis (Bailón et al., 2006). Such analysis is more challenging in AF due to presence of f-waves, however, a recent study showed that respiration rate could be accurately estimated from the ECG using a method based on the differences between the maximal upslope and the minimal downslope within a QRS interval (Kontaxis et al., 2020). In the present study we analyze ECG recordings from patients with pacemakers. The pacemaker causes sharp spikes in the signal and, hence, the previously proposed methods based on morphological variations in the QRS complex are not applicable. Instead, we exploit variation in the ECG amplitude caused by chest movements to estimate the respiration rate. Our results show that the estimated respiration rate corresponded to the expected respiration rate during controlled respiration in all patients except one (cf. Table 3). For that patient we found that a considerable amount of ectopic beats caused the respiration rate estimation to fail.

 $6.93 \pm 0.73$ 

In the present study we used a filtering approach to extract respiratory variations in the f-wave frequency trend. Adaptation of the filter to varying respiration rates is possible, however, in the present data the respiration rate was found to be constant within each phase and no adaptation of the filter was required. Another approach to extract respiratory variations in the f-wave frequency trend would be to use orthogonal subspace projections. In this approach the f-wave frequency trend can be decomposed into two different components, one respiratory component, and one residual component by a projection matrix. Such approach has previously been used to remove respiratory influence in the heart rate for improved heart rate variability analysis (Varon et al., 2019). In contrast to the filtering approach which relies on the



respiration rate, the subspace projections approach requires that a respiratory signal is available.

It has been shown that respiratory modulation in heat rate, i.e., respiratory sinus arrhythmia, can be used for noninvasive assessment of parasympathetic activity (Katona and Jih, 1975; Alcalay et al., 1992). In this study we aim to quantify respiratory modulation in the atrial activity during AF. Our results from clinical data shows that the magnitude of respiratory f-wave frequency modulation increase with deep breathing (increased parasympathetic activity) and decrease with vagal block (decreased parasympathetic tone), suggesting that respiratory modulation in the f-wave frequency trend can be partly attributed to parasympathetic regulation in the atria during AF. This is supported by a recent simulation study that showed that the parasympathetic neurotransmitter acetylcholine could be an important factor involved in f-wave frequency modulation (Celotto et al., 2020). After injection of atropine, there is still considerable variation in the respiration frequency band; these variations may be caused by other factors such as the endocrine system (Gordan et al., 2015) or stretch of the atrial tissue induced by respiratory chest movements.

# 4.1. Limitations

The proposed methodology requires ECG recordings longer than the 10 s clinical standard. The requirement that is motivated by the respiratory cycle length, which is assumed to be between 10 and 2.5 s corresponding to a respiration rate of 6–24 breaths per minute. Therefore, a 10 s ECG segment may contain only one complete respiratory cycle which is insufficient for robust analysis of respiratory modulation. The methodology was tested in a small group of AF patients with pacemakers in controlled settings and the feasibility of the methodology has to be verified in a larger study population. Further, the clinical significance of respiratory induced f-wave modulation remains to be established.

# 5. CONCLUSIONS

We introduce a novel approach to quantify respiratory induced variations in the f-wave frequency from the ECG. Results from simulated signals indicate that respiratory modulation can be accurately estimated when the signal quality is sufficient. Results from analysis of clinical data suggest that respiratory f-wave frequency modulation increase during deep breathing and decrease after injection of atropine, implying that parasympathetic ANS regulation is a contributing factor to the modulation.

# **DATA AVAILABILITY STATEMENT**

The raw data supporting the conclusions of this article will be made available by the authors, without undue reservation.

## **ETHICS STATEMENT**

The studies involving human participants were reviewed and approved by the local ethic committee and complied with the Declaration of Helsinki. The patients/participants provided their written informed consent to participate in this study.

## **AUTHOR CONTRIBUTIONS**

FS devised the project and the main conceptual ideas and was responsible for overseeing the research and providing critical insight and recommendations regarding the focus, structure, and content of the paper. MA processed the data, performed the analysis, drafted the manuscript, and designed the figures. FH was responsible for the clinical data acquisition protocol. PP helped supervise the project focusing on clinical aspects. All authors contributed to the final version of the manuscript.

## **FUNDING**

This work was supported by the European Union's Horizon 2020 research and innovation programme under the Marie Sklodowska-Curie grant agreement No. 766082, the Swedish Research Council (grant VR2019-04272), and the Crafoord Foundation (grant 20200605).

# SUPPLEMENTARY MATERIAL

The Supplementary Material for this article can be found online at: https://www.frontiersin.org/articles/10.3389/fphys. 2021.653492/full#supplementary-material

# **REFERENCES**

- Abdollahpur, M., Holmqvist, F., Platonov, P. G., and Sandberg, F. (2020). "Respiratory modulation in permanent atrial fibrillation," in 2020 Computing in Cardiology (Rimini), 1–4. doi: 10.22489/CinC.2020.182
- Alcalay, M., Izraeli, S., Wallach-Kapon, R., Tochner, Z., Benjamini, Y., and Akselrod, S. (1992). Paradoxical pharmacodynamic effect of atropine on parasympathetic control: a study by spectral analysis of heart rate fluctuations. Clin. Pharmacol. Ther. 52, 518–527. doi: 10.1038/clpt.1992.180
- Alcaraz, R., Sandberg, F., Sörnmo, L., and Rieta, J. J. (2011). Classification of paroxysmal and persistent atrial fibrillation in ambulatory ECG recordings. IEEE Trans. Biomed. Eng. 58, 1441–1449. doi: 10.1109/TBME.2011.2112658
- Bailón, R., Sörnmo, L., and Laguna, P. (2006). A robust method for ECG-based estimation of the respiratory frequency during stress testing. *IEEE Trans. Biomed. Eng.* 53, 1273–1285. doi: 10.1109/TBME.2006.871888
- Benjamin, E. J., Muntner, P., Alonso, A., Bittencourt, M. S., Callaway, C. W., Carson, A. P., et al. (2019). Heart disease and stroke statistics-2019 update: a report from the American heart association. *Circulation* 139, e56-e528. doi: 10.1161/CIR.0000000000000059
- Bollmann, A., Husser, D., Steinert, R., Stridh, M., Soernmo, L., Olsson, S. B., et al. (2003). Echocardiographic and electrocardiographic predictors for atrial fibrillation recurrence following cardioversion. J. Cardiovasc. Electrophysiol. 14(10 Suppl.), S162–S165. doi: 10.1046/j.1540.8167.90306.x
- Bollmann, A., Tveit, A., Husser, D., Stridh, M., Sörnmo, L., Smith, P., et al. (2008). Fibrillatory rate response to candesartan in persistent atrial fibrillation. *Europace* 10, 1138–1144. doi: 10.1093/europace/eun195
- Celotto, C., Sánchez, C., Mountris, K. A., Abdollahpur, M., Sandberg, F., Laguna, P., et al. (2020). "Relationship between atrial oscillatory acetylcholine release pattern and f-wave frequency modulation: a computational and experimental study," in 2020 Computing in Cardiology (Rimini), 1–4. doi: 10.22489/CinC.2020.303
- Charlton, P. H., Birrenkott, D. A., Bonnici, T., Pimentel, M. A. F., Johnson, A. E. W., Alastruey, J., et al. (2018). Breathing rate estimation from the electrocardiogram and photoplethysmogram: a review. *IEEE Rev. Biomed. Eng.* 11, 2–20. doi: 10.1109/RBME.2017.2763681
- Cheng, Z., Deng, H., Cheng, K., Chen, T., Gao, P., Yu, M., et al. (2013). The amplitude of fibrillatory waves on leads aVF and V1 predicting the recurrence of persistent atrial fibrillation patients who underwent catheter ablation: the amplitude of F wave in persistent atrial fibrillation. Ann. Noninvasive Electrocardiol. 18, 352–358. doi: 10.1111/anec.12041
- Choudhary, M. B., Holmqvist, F., Carlson, J., Nilsson, H.-J., Roijer, A., and Platonov, P. G. (2013). Low atrial fibrillatory rate is associated with spontaneous

- conversion of recent-onset atrial fibrillation.  $\it Europace~15,~1445-1452.$  doi: 10.1093/europace/eut057
- Fabritz, L., Guasch, E., Antoniades, C., Bardinet, I., Benninger, G., Betts, T. R., et al. (2016). Expert consensus document: defining the major health modifiers causing atrial fibrillation: a roadmap to underpin personalized prevention and treatment. Nat. Rev. Cardiol. 13, 230–237. doi: 10.1038/nrcardio.2015.194
- Gordan, R., Gwathmey, J. K., and Xie, L.-H. (2015). Autonomic and endocrine control of cardiovascular function. World J. Cardiol. 7, 204–214. doi: 10.4330/wic.v7.i4.204
- Henriksson, M., Petrenas, A., Marozas, V., Sandberg, F., and Sornmo, L. (2018). Model-based assessment of f-wave signal quality in patients with atrial fibrillation. *IEEE Trans. Biomed. Eng.* 65, 2600–2611. doi: 10.1109/TBME.2018.2810508
- Hindricks, G., Potpara, T., Dagres, N., Arbelo, E., Bax, J. J., Blomström-Lundqvist, C., et al. (2020). 2020 ESC guidelines for the diagnosis and management of atrial fibrillation developed in collaboration with the European association of Cardio-Thoracic surgery (EACTS). Eur. Heart J. 42, 373–498. doi: 10.1093/eurhearti/ehaa612
- Holmqvist, F., Stridh, M., Waktare, J. E. P., Brandt, J., Sörnmo, L., Roijer, A., et al. (2005). Rapid fluctuations in atrial fibrillatory electrophysiology detected during controlled respiration. Am. J. Physiol. Heart Circ. Physiol. 289, H754–H760. doi: 10.1152/ajpheart.00075.2005
- Ingemansson, M. P., Holm, M., and Olsson, S. B. (1998). Autonomic modulation of the atrial cycle length by the head up tilt test: non-invasive evaluation in patients with chronic atrial fibrillation. *Heart* 80, 71–76. doi: 10.1136/hrt.80.1.71
- Katona, P. G., and Jih, F. (1975). Respiratory sinus arrhythmia: noninvasive measure of parasympathetic cardiac control. J. Appl. Physiol. 39, 801–805. doi: 10.1152/jappl.1975.39.5.801
- Kontaxis, S., Lazaro, J., Corino, V. D. A., Sandberg, F., Bailon, R., Laguna, P., et al. (2020). ECG-derived respiratory rate in atrial fibrillation. *IEEE Trans. Biomed. Eng.* 67, 905–914. doi: 10.1109/TBME.2019.2923587
- Lankveld, T., Zeemering, S., Scherr, D., Kuklik, P., Hoffmann, B. A., Willems, S., et al. (2016). Atrial fibrillation complexity parameters derived from surface ECGs predict procedural outcome and long-term follow-up of stepwise catheter ablation for atrial fibrillation. Circ. Arrhythm. Electrophysiol. 9:e003354. doi: 10.1161/CIRCEP.115.003354
- Lankveld, T. A. R., Zeemering, S., Crijns, H. J. G. M., and Schotten, U. (2014). The ECG as a tool to determine atrial fibrillation complexity. *Heart* 100, 1077–1084. doi: 10.1136/heartinl-2013-305149
- Lázaro, J., Gil, E., Bailón, R., Mincholé, A., and Laguna, P. (2013). Deriving respiration from photoplethysmographic pulse width. Med. Biol. Eng. Comput. 51, 233–242. doi: 10.1007/s11517-012-0954-0

- Liu, L., and Nattel, S. (1997). Differing sympathetic and vagal effects on atrial fibrillation in dogs: role of refractoriness heterogeneity. Am. J. Physiol. 273(2 Pt 2), H805–H816. doi: 10.1152/ajpheart.1997.273.2.H805
- Meo, M., Zarzoso, V., Meste, O., Latcu, D. G., and Saoudi, N. (2013). Spatial variability of the 12-lead surface ECG as a tool for noninvasive prediction of catheter ablation outcome in persistent atrial fibrillation. *IEEE Trans. Biomed. Eng.* 60, 20–27. doi: 10.1109/TBME.2012.2220639
- Meurling, C. J., Waktare, J. E., Holmqvist, F., Hedman, A., Camm, A. J., Olsson, S. B., et al. (2001). Diurnal variations of the dominant cycle length of chronic atrial fibrillation. Am. J. Physiol. Heart Circ. Physiol. 280, H401–H406. doi: 10.1152/ajpheart.2001.280.1.H401
- Nault, I., Lellouche, N., Matsuo, S., Knecht, S., Wright, M., Lim, K.-T., et al. (2009). Clinical value of fibrillatory wave amplitude on surface ECG in patients with persistent atrial fibrillation. *J. Interv. Card. Electrophysiol.* 26, 11–19. doi: 10.1007/s10840-009-9398-3
- Östenson, S., Corinto, V. D. A., Carlsson, J., and Platonov, P. G. (2017). Autonomic influence on atrial fibrillatory process: head-up and head-down tilting. Ann. Noninvasive Electrogardial. 22:e12405. doi: 10.1111/ane.12405
- Park, J., Lee, C., Leshem, E., Blau, I., Kim, S., Lee, J. M., et al. (2019). Early differentiation of long-standing persistent atrial fibrillation using the characteristics of fibrillatory waves in surface ECG multi-leads. Sci. Rep. 9:2746. doi: 10.1038/s41598-019-38928-6
- Petrutiu, S., Ng, J., Nijm, G. M., Al-Angari, H., Swiryn, S., and Sahakian, A. V. (2006). Atrial fibrillation and waveform characterization. a time domain perspective in the surface ECG. IEEE Eng. Med. Biol. Mag. 25, 24–30. doi: 10.1109/EMB-M.2006.250505
- Platonov, P. G., Corino, V. D. A., Seifert, M., Holmqvist, F., and Sörnmo, L. (2014). Atrial fibrillatory rate in the clinical context: natural course and prediction of intervention outcome. *Europace* 16(Suppl. 4), iv110-iv119. doi: 10.1093/europace/euu249
- Platonov, P. G., Cygankiewicz, I., Stridh, M., Holmqvist, F., Vazquez, R., Bayes-Genis, A., et al. (2012). Low atrial fibrillatory rate is associated with poor outcome in patients with mild to moderate heart failure. Circ. Arrhythm. Electrophysiol. 5, 77–83. doi: 10.1161/CIRCEP.111.964395
- Raja Kumar, R. V., and Pal, R. N. (1985). A gradient algorithm for center-frequency adaptive recursive bandpass filters. Proc. IEEE Inst. Electr. Electron. Eng. 73, 371–372. doi: 10.1109/PROC.1985.13149
- Rezek, I., Roberts, S. J. (1998). Envelope Extraction via Complex Homomorphic Filtering. Imperial College of Science, Technology, and Medicine Technical Report TR-98-9.
- Sandberg, F., Bollmann, A., Husser, D., Stridh, M., and Sörnmo, L. (2010). Circadian variation in dominant atrial fibrillation frequency in persistent atrial fibrillation. *Physiol. Meas.* 31, 531–542. doi: 10.1088/0967-3334/31/4/005

- Sandberg, F., Holmer, M., and Olde, B. (2019). Monitoring respiration using the pressure sensors in a dialysis machine. *Physiol. Meas.* 40:025001. doi: 10.1088/1361-6579/aaf978
- Sharifov, O. F., Fedorov, V. V., Beloshapko, G. G., Glukhov, A. V., Yushmanova, A. V., and Rosenshtraukh, L. V. (2004). Roles of adrenergic and cholinergic stimulation in spontaneous atrial fibrillation in dogs. J. Am. Coll. Cardiol. 43, 483–490. doi: 10.1016/j.jacc.2003.09.030
- Shen, M. J., Shinohara, T., Park, H.-W., Frick, K., Ice, D. S., Choi, E.-K., et al. (2011). Continuous low-level vagus nerve stimulation reduces stellate ganglion nerve activity and paroxysmal atrial tachyarrhythmias in ambulatory canines. Circulation 123, 2204–2212. doi: 10.1161/CIRCULATIONAHA.111.0 18028
- Shen, M. J., and Zipes, D. P. (2014). Role of the autonomic nervous system in modulating cardiac arrhythmias. Circ. Res. 114, 1004–1021. doi: 10.1161/CIRCRESAHA.113.302549
- Smith, J. G., Platonov, P. G., Hedblad, B., Engström, G., and Melander, O. (2010). Atrial fibrillation in the Malmö diet and cancer study: a study of occurrence, risk factors and diagnostic validity. Eur. J. Epidemiol. 25, 95–102. doi: 10.1007/s10654-009-9404-1
- Sörnmo, L. (ed.). (2018). Atrial Fibrillation From an Engineering Perspective. Cham: Springer International Publishing.
- Stridh, M., Meurling, C., Olsson, B., and Sörnmo, L. (2003). Detection of autonomic modulation in permanent atrial fibrillation. *Med. Biol. Eng. Comput.* 41, 625–629. doi: 10.1007/BF02349969
- Stridh, M., and Sörnmo, L. (2001). Spatiotemporal QRST cancellation techniques for analysis of atrial fibrillation. *IEEE Trans. Biomed. Eng.* 48, 105–111. doi: 10.1109/10.900266
- Varon, C., Lazaro, J., Bolea, J., Hernando, A., Aguilo, J., Gil, E., et al. (2019). Unconstrained estimation of HRV indices after removing respiratory influences from heart rate. *IEEE J. Biomed. Health Inform.* 23, 2386–2397. doi: 10.1109/IBHI.2018.2884644

Conflict of Interest: The authors declare that the research was conducted in the absence of any commercial or financial relationships that could be construed as a potential conflict of interest.

Copyright © 2021 Abdollahpur, Holmqvist, Platonov and Sandberg. This is an openaccess article distributed under the terms of the Creative Commons Attribution License (CC BY). The use, distribution or reproduction in other forums is permitted, provided the original author(s) and the copyright owner(s) are credited and that the original publication in this journal is cited, in accordance with accepted academic practice. No use, distribution or reproduction is permitted which does not comply with three terms

# $oxed{Paper\ II}$



#### **OPEN ACCESS**

EDITED BY Ruben Coronel, University of Amsterdam, Netherlands

REVIEWED BY

Andrius Petrènas, Kaunas University of Technology, Lithuania Marianna Meo, EPD Solutions, a Philips company,

\*CORRESPONDENCE

Mostafa Abdollahpur, mostafa.abdollahpur@bme.lth.se

SPECIALTY SECTION

This article was submitted to Cardiac Electrophysiology, a section of the journal Frontiers in Physiology

RECEIVED 01 July 2022 ACCEPTED 23 August 2022 PUBLISHED 19 September 2022

#### CITATION

Abdollahpur M, Engström G, Platonov PG and Sandberg F (2022), A subspace projection approach to quantify respiratory variations in the fwave frequency trend. Front. Physiol. 13:976925. doi: 10.3389/fphys.2022.976925

#### COPYRIGHT

© 2022 Abdollahpur, Engström, Platonov and Sandberg. This is an openaccess article distributed under the terms of the Creative Commons Attribution License (CC BY). The use, distribution or reproduction in other forums is permitted, provided the original author(s) and the copyright owner(s) are credited and that the original publication in this journal is cited, in accordance with accepted academic practice. No use, distribution or reproduction is permitted which does not comply with these terms.

# A subspace projection approach to quantify respiratory variations in the f-wave frequency trend

Mostafa Abdollahpur<sup>1\*</sup>, Gunnar Engström<sup>2</sup>, Pyotr G. Platonov<sup>3</sup> and Frida Sandberg<sup>1</sup>

<sup>1</sup>Department of Biomedical Engineering, Lund University, Lund, Sweden, <sup>2</sup>Department of Clinical Sciences, Cardiovascular Research—Epidemiology, Malmö, Sweden, <sup>3</sup>Department of Cardiology, Clinical Sciences, Lund University, Lund, Sweden

**Background:** The autonomic nervous system (ANS) is known as a potent modulator of the initiation and perpetuation of atrial fibrillation (AF), hence information about ANS activity during AF may improve treatment strategy. Respiratory induced ANS variation in the f-waves of the ECG may provide such information.

**Objective:** This paper proposes a novel approach for improved estimation of such respiratory induced variations and investigates the impact of deep breathing on the f-wave frequency in AF patients.

**Methods:** A harmonic model is fitted to the f-wave signal to estimate a high-resolution f-wave frequency trend, and an orthogonal subspace projection approach is employed to quantify variations in the frequency trend that are linearly related to respiration using an ECG-derived respiration signal. The performance of the proposed approach is evaluated and compared to that of a previously proposed bandpass filtering approach using simulated f-wave signals. Further, the proposed approach is applied to analyze ECG data recorded for 5 min during baseline and 1 min deep breathing from 28 AF patients from the Swedish cardiopulmonary bioimage study (SCAPIS).

**Results:** The simulation results show that the estimates of respiratory variations obtained using the proposed approach are more accurate than estimates obtained using the previous approach. Results from the analysis of SCAPIS data show no significant differences between baseline and deep breathing in heart rate (75.5  $\pm$  22.9 vs. 74  $\pm$  22.3) bpm, atrial fibrillation rate (6.93  $\pm$  1.18 vs. 6.94  $\pm$  0.66) Hz and respiratory f-wave frequency variations (0.130  $\pm$  0.042 vs. 0.130  $\pm$  0.034) Hz. However, individual variations are large with changes in heart rate and atrial fibrillatory rate in response to deep breathing ranging from –9% to +5% and –8% to +6%, respectively and there is a weak correlation between changes in heart rate and changes in atrial fibrillatory rate (r = 0.38, p < 0.03).

**Conclusion:** Respiratory induced f-wave frequency variations were observed at baseline and during deep breathing. No significant changes in the magnitude of these variations in response to deep breathing was observed in the present study population.

KEVWORDS

atrial fibrillation, autonomic nervous system, respiratory variation, f-wave frequency, ECG processing

## 1 Introduction

Atrial fibrillation is known as the most common heart arrhythmia and is a growing public health concern worldwide. Atrial fibrillation has been estimated to affect 10 million people in the United States by 2050 (Miyasaka et al., 2006) and 17.9 million in Europe by 2060, with more than half of these patients aged 80 years or older (Krijthe et al., 2013). Atrial fibrillation is associated with increased mortality and morbidity resulting from stroke and congestive heart failure, and increased hospitalization costs (Patel et al., 2014). Despite progression in AF treatment, including medications aimed at controlling heart rate, rhythm, or both, and ablative therapy, finding the most accurate therapy for an individual patient is still problematic (Crandall et al., 2009). Historically, research has shown that multiple etiological mechanisms, such as atrial fibrosis, ion-channel dysfunction, autonomic imbalance, and genetic background, likely drive the factors associated with the maintenance and progression of AF (Lip et al., 2010; Fabritz et al., 2016).

This study focuses on respiratory modulation in the atrial activity during AF. It is well established from a variety of studies that the refractory period of the atria during atrial fibrillation can be influenced by various underlying mechanisms, including pathological changes, electrophysiological dynamics, and an imbalanced autonomic tone (Waldo, 2003; Nitta et al., 2004; Saksena et al., 2005). The refractory period of the atria has been found to have linear correlation with f-waves frequency (Capucci et al., 1995). The frequency of the f-waves in the ECG, also referred to as the atrial fibrillatory rate (AFR) (Platonov et al., 2014), has previously been analyzed with respect to ANS induded changes during AF. For instance (Stridh et al., 2003; Holmqvist et al., 2005), have shown that variation in the f-wave frequency during controlled respiration can be linked to the parasympathetic activity. Östenson et al. studied changes in the f-wave frequency in response to changes in ANS tone induced by tilt-test in 40 patients with persistent AF, results showed f-wave frequency decreased during head-down tilt (HDT) compared to baseline and increased during head-up tilt (HUT) (Östenson et al., 2017). In a previous study, we investigated changes in f-wave frequency variations in response to controlled respiration (Abdollahpur et al., 2021). In a study population of eight pacemaker patients with permanent AF recorded at baseline, during controlled respiration, and during controlled respiration after injection of atropine. Briefly, a high-resolution f-wave frequency trend obtained using model-based approach was filtered using a narrow bandpass filter with center frequency corresponding to respiration rate and fixed bandwidth. The envelope of the filtered frequency trend served as an estimate of the magnitude of the respiratory variation; the results indicated that this magnitude was affected by parasympathetic regulation (Abdollahpur et al., 2021).

The present study addresses main weaknesses of our previous study. In contrast to the previous study, where the AF patients had pacemakers set at a fixed heart rate, the present study is based on AF patients without pacemaker whose heart rate varies over time. Such variations in heart rate may affect the ANS and hence the ANS induced variations in atrial electrical activity. Second, the previous approach to quantify respiratory variation in the f-wave frequency is sensitive to noise and cannot handle time-varying respiration rates. Hence, the objectives of the present study were twofold: 1) To propose a novel subspace projection approach to quantify respiratory variation in the f-wave frequency trend that is robust to noise and can handle time-varying respiration, and 2) to investigate the impacts of deep breathing on the f-wave frequency in a population of AF patients without a pacemaker.

# 2 Materials and methods

A schematic overview of the methodology is shown in Figure 1. The clinical data is described in Section 2.1, the ECG processing aiming to obtain an f-wave signal x(n) is explained in Section 2.2. As follow, a model-based approach is applied to the extracted signal x(n) to estimate an f-wave frequency trend f(n) (Section 2.3). An ECG-derived respiration signal r(n) is estimated using the slope range approach (Section 2.4). Respiratory variation in f(n) is estimated using orthogonal subspace projection method (Section 2.5). Simulated f-wave signals are used to evaluate the performance of the proposed methodology (Section 2.6). Finally, statistical tests are applied to the results from analysis of clinical data to determine if there is a significant differences in heart rate, f-wave frequency, and respiratory variation in f-wave frequency trend between deep breathing phase and baseline (Section 2.7).

# 2.1 ECG data

The study population consists of a subset of 28 participants from the Swedish cardiopulmonary bioimage study (SCAPIS) (Bergström et al., 2015) that were diagnosed with AF. The clinical characteristics of the study population are summarized in Table 1. The subjects performed a deep breathing task. The task was 5-s inhalation and 5-s exhalation as deep-breathing (D) phase for 1 min, and as follows 5 min during baseline (B); the patients were in AF during the recordings. For further details on the study protocol, the reader is referred to (Engström et al.,

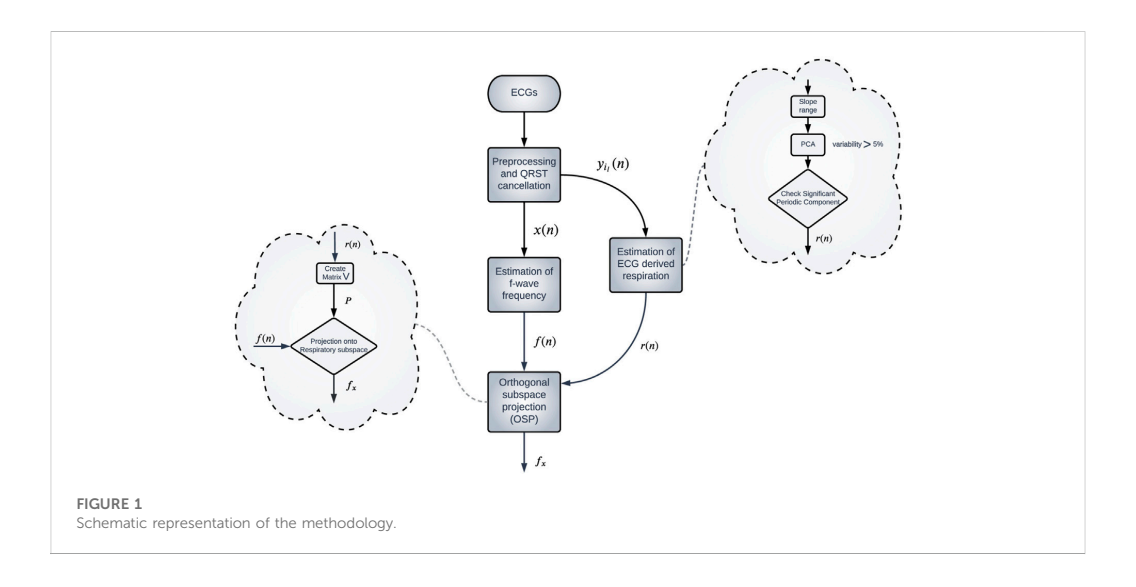


TABLE 1 Clinical characteristics of patients.

	Number
Age (mean ± SD, range)	60.1 ± 4.0 [50.1-64.9]
Men (%)	23 (82)
BMI (mean ± SD, range)	31.8 ± 7.2 [18.8-50.8]
Systolic BP	124 ± 23 [90-188]
Diastolic BP	79.9 ± 11 [61–104]
Hypertension*(%)	17 (61)
Diabetes (%)	2 (7)
Never smokers (%)	9 (32)
Heart failure (%)	2 (7)
Previous AMI or angina (%)	2 (7)
Treatment	
Beta blocker (%)	15 (54)
Ca-antagonist (%)	6 (21)
Antiarrhythmic drug (%)	4 (14)

<sup>\* ≥140/90</sup> mmHg or treatment for hypertension.

2022). A standard 12-lead ECG at 500 Hz sampling rate was recorded throughout the protocol.

# 2.2 ECG processing

The CardioLund ECG parser (CardioLund Research AB, Lund, Sweden) is used for preprocessing, beat-detection, and beat

classification and QRST cancellation. Briefly, in this software, a linear-phase high-pass filter is applied to the ECG to eliminate baseline wander, and fiducial points in the QRS complexes are detected; also, the QRS complexes are classified based on their morphology. The ectopic beats were identified based on correlation to template beats and were clustered and treated as a separate class for the QRST-cancellation. The QRS interval  $v_{i}(n)$  is set to 140 ms, starting 110 ms before the end of the S wave and finishing 30 ms after the end of the S wave, where i and l denotes beat-number and lead, respectively. A spatiotemporal QRST cancellation approach (Stridh and Sörnmo, 2001) is employed to extract f-wave signals from the ECG. This average beat subtraction method compensates for minor morphological variations in the QRST complex by combining beat averages from different leads. For each beat class, one beat average is calculated and used for QRST cancellation in the corresponded beats in the ECG leads. The extracted f-wave signal is downsampled from 1 kHz to 50 Hz using appropriate low-pass filtering and decimation since such signals have negligible frequency content above 25 Hz. In the present study, the extracted f-wave signal from lead V1 denoted x(n), is subjected to analysis. For further analysis, the ECG data was divided into 1-min segments, resulting in five segments at baseline and one segment during deep breathing. The AFR and respiratory f-wave modulation was estimated from each 1-min segment of x(n) as described in Section 2.3 and Section 2.5, respectively. A respiration signal, which is required for estimation of respiratory f-wave modulation, was obtained from the corresponding QRS intervals  $y_{i_1}(n)$  as described in Section 2.4; ectopic beats were removed for this analysis. For each patient, results from the 1-min segments recorded at baseline were averaged to obtain the heart rate (HRB), atrial fibrillatory rate

 $(AFR^B)$ , and respiratory f-wave frequency modulation  $(\Delta f_{OSP}^B)$ , respectively. The corresponding estimates during deep breathing  $(HR^D, AFR^D, \Delta f_{OSP}^D)$  were based on one segment.

# 2.3 Estimation of f-wave frequency trend

For the estimation of a high-resolution f-wave frequency trend, a harmonic f-wave model (Henriksson et al., 2018) is employed. The model f-wave signal is defined as the sum of a complex exponential signal with fundamental frequency f and its second harmonic.

$$s(n;\boldsymbol{\theta}) = \sum_{m=1}^{2} A_m e^{j\left(m2\pi \frac{f}{f_s}n + \phi_m\right)}, \tag{1}$$

where  $A_m$  and  $\phi_m$  denote the amplitude and phase of m:th harmonic, respectively, and  $f_s$  is sampling frequency. The use of two harmonics in the model is motivated by the observations in (Henriksson et al., 2018), that additional harmonic results in more noise due to the additional degrees of freedom of this model. The parameters  $\boldsymbol{\theta} = \begin{bmatrix} f & A_1 & A_2 & \phi_1 & \phi_2 \end{bmatrix}^T$ , are estimated by fitting the harmonic model  $s(n; \boldsymbol{\theta})$  to the analytic equivalent of x(n), denoted  $x_o(n)$ , using maximum likelihood approach.

$$\hat{\boldsymbol{\theta}} = \arg\min_{\boldsymbol{\theta}} \|x_a(\boldsymbol{n}) - s(\boldsymbol{n}; \boldsymbol{\theta})\|^2, \tag{2}$$

The model is fitted to 20 ms overlapping 0.5-second segments of  $x_a(n)$ . For this fitting, f is constrained to the interval  $[f_0 \pm 1.5]$  Hz, where global frequency estimate  $(f_0)$  is the maximum peak in the interval [4,12] Hz of the Welch periodogram of the whole x(n). The estimates of f result in an f-wave frequency trend f(n) sampled at 50 Hz. Then, correspond to the sampling rate of the respiration signal (cf. Section 2.4), f(n) is resampled to 5Hz. To quantify accuracy of the fitted model, a signal quality index, denoted  $\mathcal{S}$ , is computed

$$S = 1 - \frac{\sigma_{\hat{e}}}{\sigma_{r}},\tag{3}$$

where  $\sigma_{\hat{e}}$  and  $\sigma_{x_a}$  denote the standard deviation of the model error  $(\hat{e}(n) = x_a(n) - s(n; \hat{\theta}))$  and  $x_a(n)$ , respectively. In this study,  $\mathcal{S}$  is computed for non-overlappning 5 s segments.  $\mathcal{S}$  ranges from 0 to 1, where a higher value corresponds to a better fit. Only segments with  $\mathcal{S} > 0.3$  is considered for further analysis, since previous studies has shown that  $\mathcal{S}$  larger than 0.3 was sufficient for accurate estimation of f(n) (Henriksson et al., 2018). The atrial fibrillatory rate (AFR) is estimated by the median of f(n).

# 2.4 Estimation of ECG-derived respiration

The slope range method (Kontaxis et al., 2019) is applied to each lead of the ECG separately to obtain a respiratory signal. The

method quantifies variations in the QRS morphology, which are assumed to reflect respiratory activity, using the difference between the maximum and minimum derivative in the QRS interval,

$$r_l(i) = \max_{n} \{ y'_{i_l}(n) \} - \min_{n} \{ y'_{i_l}(n) \}, \tag{4}$$

where i and l denotes beat-number and lead, respectively, and  $y_{i}'(n) = y_{i}(n) - y_{i}(n-1)$ . The resulting signal  $r_{i}(i)$  is resampled to 5Hz using cubic spline interpolation to obtain a uniformly sampled signal  $r_i(n)$ . Principal component analysis (PCA) is applied to the set of  $r_l(n)$  to derive a joint respiratory signal from all leads. The principal component that has the greatest variance and a significant periodic component in the respiratory interval ([0.1 0.5] Hz) is selected as the respiratory signal, denoted as r(n). A principal component is considered to have a significant periodic component if the magnitude of the largest peak in the respiratory interval of its spectrum is at least 85% of the largest peak in the whole spectrum. The spectra are estimated by Welch periodograms based on 30 s sliding 25 s overlapping segments of PCA components. If none of the principal component accounting for more than 5% of the total variance has a significant periodic component in the respiration interval, no respiration signal is extracted.

# 2.5 Orthogonal subspace projection

To extract variations in the f-wave frequency trend that are linearly related to the respiration, an orthogonal subspace projection approach is employed (Chang, 2005). The demeaned f(n) denoted as  $\tilde{f}(n)$  is projected onto a subspace defined by the matrix V, constructed using the respiratory signal r(n),

$$V = [r_0, r_1, \dots, r_d, \dots, r_m], \tag{5}$$

$$\mathbf{r}_d = \{r(1+d), r(2+d), \dots, r(N-m+d)\}^T,$$
 (6)

The model order m is determined by analysis of the simulated data (cf. Section 3.1). After creating the matrix V, the signal  $\tilde{f}(n)$  is projected onto the respiratory subspace using

$$f_{r} = V(V^{T}V)^{-1}V^{T}f = Pf, \tag{7}$$

where f is a length N vector of  $\tilde{f}(n)$ , P is the projection matrix of size  $N-m\times N-m$ , and  $f_x$  is the component of f that is linearly related to respiration. The power of the variations linearly related to respiration  $(f_x^\top f_x)$  is a fraction of the total power of the variations  $(f^\top f)$ . Assuming that the variations in  $f_x$  are sinusoidal, the peak-to-peak amplitude is given by

$$\Delta \bar{f}_{OSP} = \sqrt{\frac{2 \cdot (f_x^{\top} f_x)}{N}},$$
 (8)

In the present study,  $\Delta \bar{f}_{OSP}$  serves as an estimate of the magnitude of the respiratory induced f-wave frequency variations.

## 2.6 Performance evaluation

Simulated f-wave signals were used in order to assess the performance of the orthogonal subspace projection approach and its dependence on model order m (Section 2.5), signal quality S (Section 2.3) and characteristics of the f-wave signals. The f-wave signals were simulated by a modified version of the sawtooth model proposed by (Stridh and Sörnmo, 2001). The f-wave signal is the sum of a sinusoid and its harmonic with time-varying frequency

$$x_{sim}(n) = \sum_{k=1}^{2} A_k(n) \sin(2\pi k F(n)n) + v(n), \qquad (9)$$

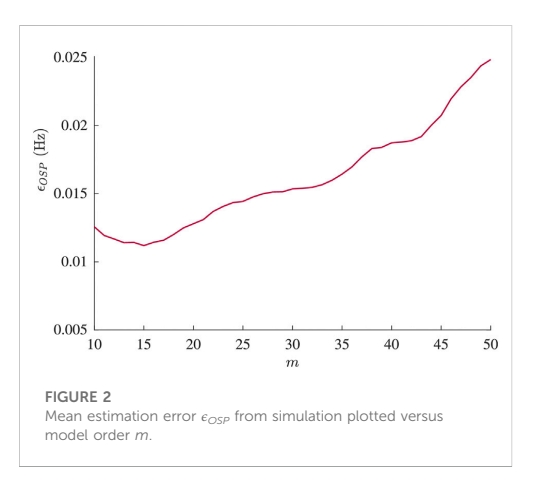
$$F(n) = \frac{F}{F_s} + \frac{\Delta F}{2\pi F_r n} \sin\left(2\pi n \frac{F_r}{F_s}\right) + \frac{\Phi(n)}{2\pi k n},\tag{10}$$

where F defines the average fundamental frequency, and respiratory f-wave frequency variation is quantified by  $F_r$  and  $\Delta F$ , defining the variation frequency and the variation magnitude, respectively. To incorporate other forms of variation in the f-wave frequency, random phase variation,  $\Phi(n)$ , is added; it is modeled as white Gaussian noise with standard deviation  $\sigma_{\Phi}$ . The amplitude of the k:th harmonic is given by

$$A_k(n) = \frac{2}{k\pi} (A + \Delta A(n)), \tag{11}$$

where A is the average f-wave amplitude, and  $\Delta A(n)$  quantifies random amplitude variation and is assumed to have a Gaussian distribution with mean zero and standard deviation A/5; the parameter A was chosen to obtain a signal standard deviation of signal  $\sigma_x$  equal to 50. The following parameters were used for simulating one minute-long f-wave signals:  $F = \{4, 5, 6, 7, 8, 9, 10\}$  Hz,  $F_r = \{0.1, 0.15, 0.20, 0.25, 0.30\}$  Hz,  $\Delta F = \{0, 0.025, 0.05, \ldots, 0.3\}$  Hz,  $\sigma_{\Phi} = \{0.27, 0.40, 0.55, 0.67, 0.80\}$ . White Gaussian noise v(n) with  $\sigma_v = \{0.1A, 0.2A, 0.3A, 0.4A, 0.5A\}$  is added to form realistic f-wave signals and the sampling frequency was set to  $F_s = 50$  Hz. Ten realizations of  $x_{sim}(n)$  for each parameter setting were considered, resulting in a total of 113,750 simulated signals.

Through these simulated signals, the accuracy of  $\Delta \bar{f}_{OSP}$  as an estimate of  $\Delta F$  is compared to our previously proposed band-pass filtering approach to quantify respiratory induced variations in the f-wave frequency trend (Abdollahpur et al., 2021). In that method, respiratory variation is estimated by applying a narrow band-pass filter with a fixed bandwidth of 0.06 Hz and a center frequency corresponding to the  $F_r$ . The f-wave frequency trend f(n) obtained as described in Section 2.3. The average envelope of the filtered f(n), denoted  $\Delta \bar{f}_{BP}$ , is used to quantify the magnitude of the respiratory variation. The absolute difference between  $\Delta F$  and  $\Delta \bar{f}_{BP}$ , denoted as  $\epsilon_{BP}$ , and the absolute difference between



 $\Delta F$  and  $\Delta \bar{f}_{OSP}$  denoted as  $\epsilon_{OSP}$  are used to assess the performance of the methods.

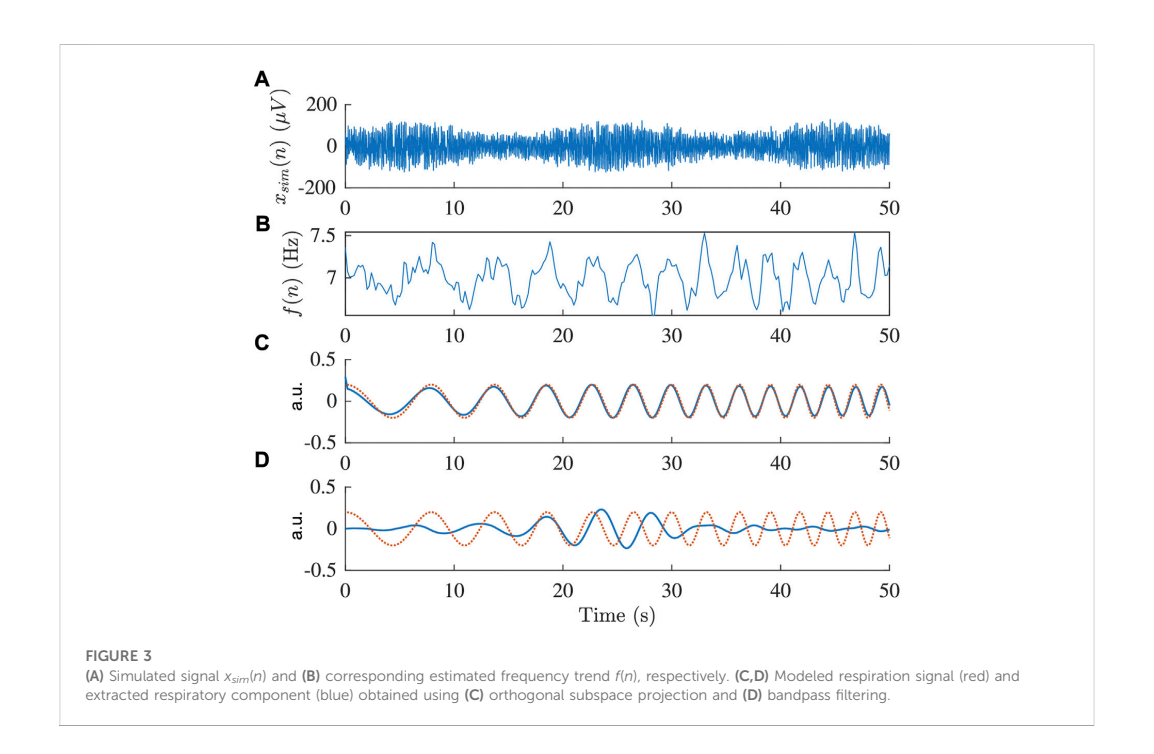
# 2.7 Statistical analysis

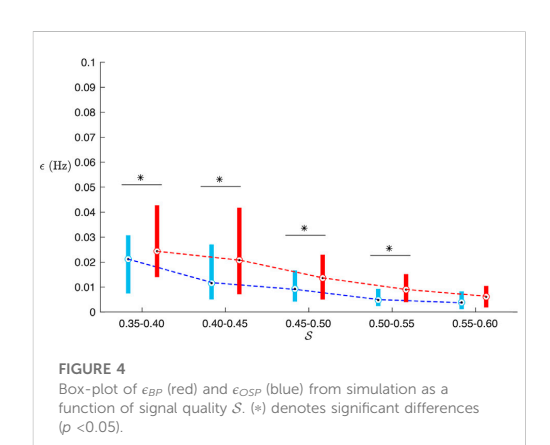
Results are presented as mean  $\pm$  std, and as median (range) for Gaussian and non-gaussian variables, respectively; the Lilliefors test is used to test for gaussianity. Student's t-test and Wilcoxon signed-rank test are applied to determine if differences are significant for Gaussian and non-gaussian variables, respectively. Hence, a paired t-test is applied to evaluate the difference between  $\epsilon_{OSP}$  and  $\epsilon_{BP}$ , and a Wilcoxon signed-rank test is applied to determine whether differences in HR, AFR, and  $\Delta f_{OSP}$  between baseline and deep breathing are significant. Further, Spearman rank correlation is used to evaluate the relationship between changes in HR, AFR, and  $\Delta f_{OSP}$  in response to deep breathing. The level of statistical significance is considered p < 0.05.

## 3 Results

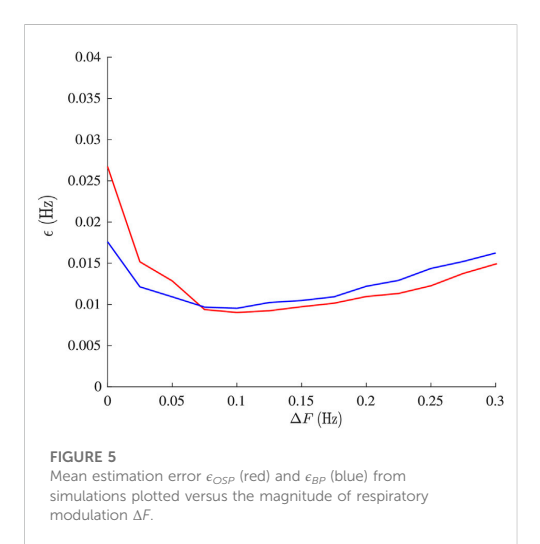
# 3.1 Simulations

Results from the analysis of simulated data are presented in Figures 2–5. From Figure 2, it is apparent that the smallest  $\epsilon_{OSP}$  was achieved for m=15, and hence, m was set to 15 for the remaining analysis. The effect of the time-varying respiration is illustrated in Figure 3 where  $F_r$  changes from 0.1 to 0.3 Hz during 1 minute. As shown in Figure 3, the

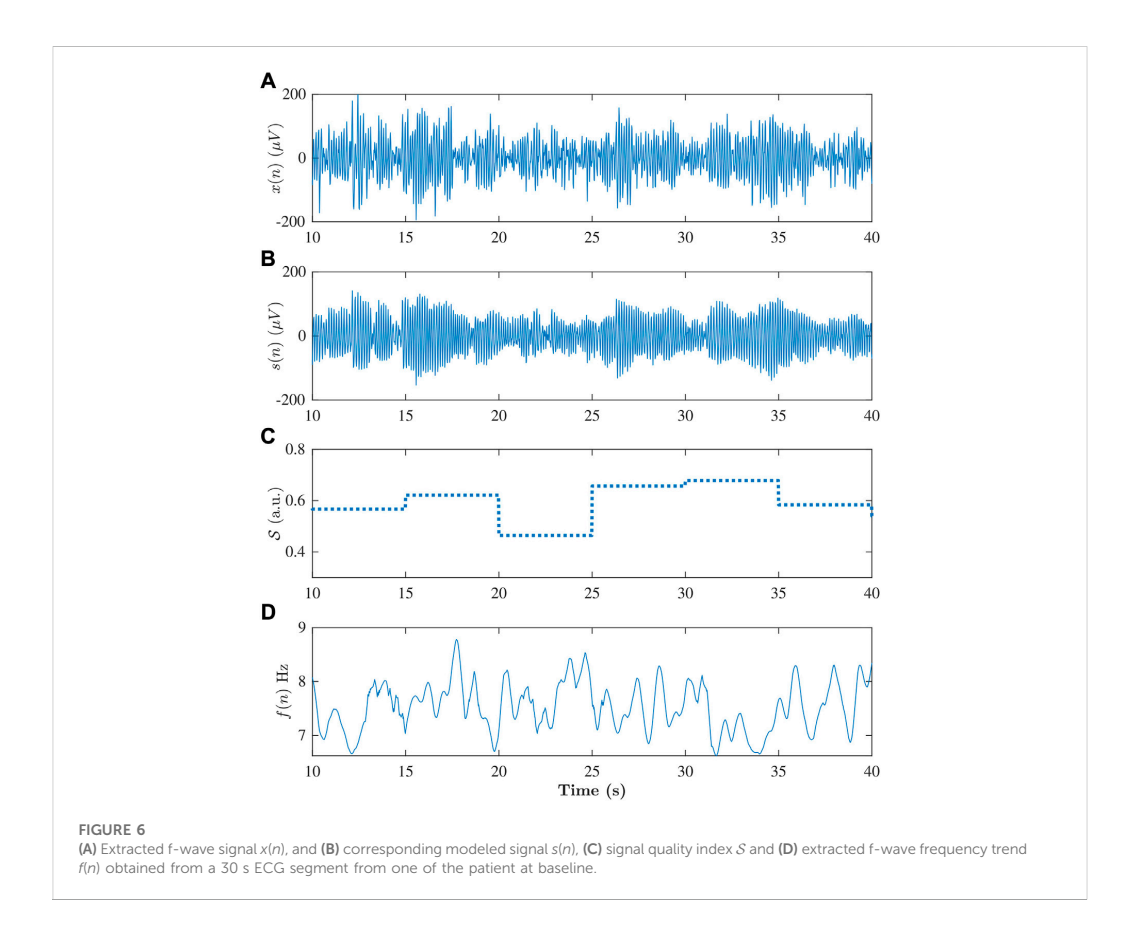




respiratory variations can be accurately extracted using the orthogonal subspace projection approach, while the previously proposed bandpass filtering approach fails. The  $\epsilon_{OSP}$  was significantly smaller than  $\epsilon_{BP}$  (0.017  $\pm$  0.012 vs. 0.021  $\pm$  0.015, p < 0.001). The improved accuracy obtained with the orthogonal subspace projection approach is more



prominent for lower values of S, corresponding to higher noise levels, cf. Figure 4. The accuracy of the estimates was



not affected by the f-wave frequency and the respiration rate (results not shown). However, for both approaches the estimates were less accurate for respiratory variations of small magnitudes ( $\Delta f < 0.075 \text{ Hz}$ ), cf. Figure 5.

# 3.2 Heart rate and f-wave frequency

An example of a 30-second f-wave signal x(n) and the corresponding model signal  $s(n;\theta)$ , signal quality index S, and extracted f-wave frequency trend f(n) is displayed in Figure 6. The signal quality was sufficient (S > 0.3) for estimation of f(n) in 98% of the data. The  $AFR^B$  was 6.93 (4.65–6.97) Hz and  $AFR^D$  was 6.94 (4.56–6.99) Hz, a paired t-test showed no significant difference between baseline and deep breathing. The  $HR^B$  was 75.5 (37–150) bpm and  $HR^D$  was 74 (37–146) bpm; there were no significant differences between baseline and deep breathing. The changes in AFR versus changes in HR are displayed in Figure 7. The changes

in AFR range between -8 and 6%, and the changes in HR range between -9 and 5%. There was a weak correlation between changes in HR and changes in AFR (r=0.38, p<0.03). The linear dependence between changes in HR and changes in AFR appears to be more pronounced for patients where the heart rate decreases in response to deep breathing, cf. Figure 7.

# 3.3 Respiration

Figure 8 gives an example of extracted respiratory signals  $r_l(n)$  and the corresponding principal components for one patient during deep breathing. In this example, both  $r_{PC_1}(n)$  and  $r_{PC_2}(n)$  have a significant periodic component according to definition in Section 2.4. The  $r_{PC_1}(n)$  is selected as respiration signal (r(n)) since it has the largest variance. Respiration signals r(n) could be obtained from 118 out of 168 (70%) of the analyzed 1-min segments. The estimated respiration rate  $F_r$  was

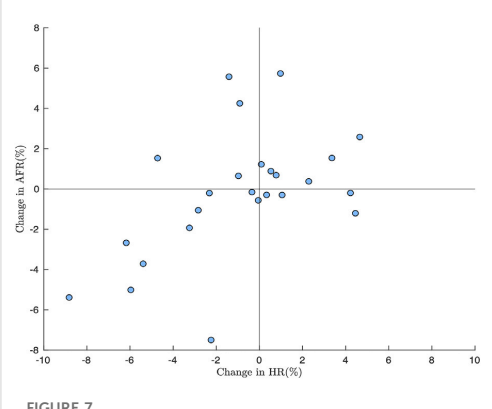
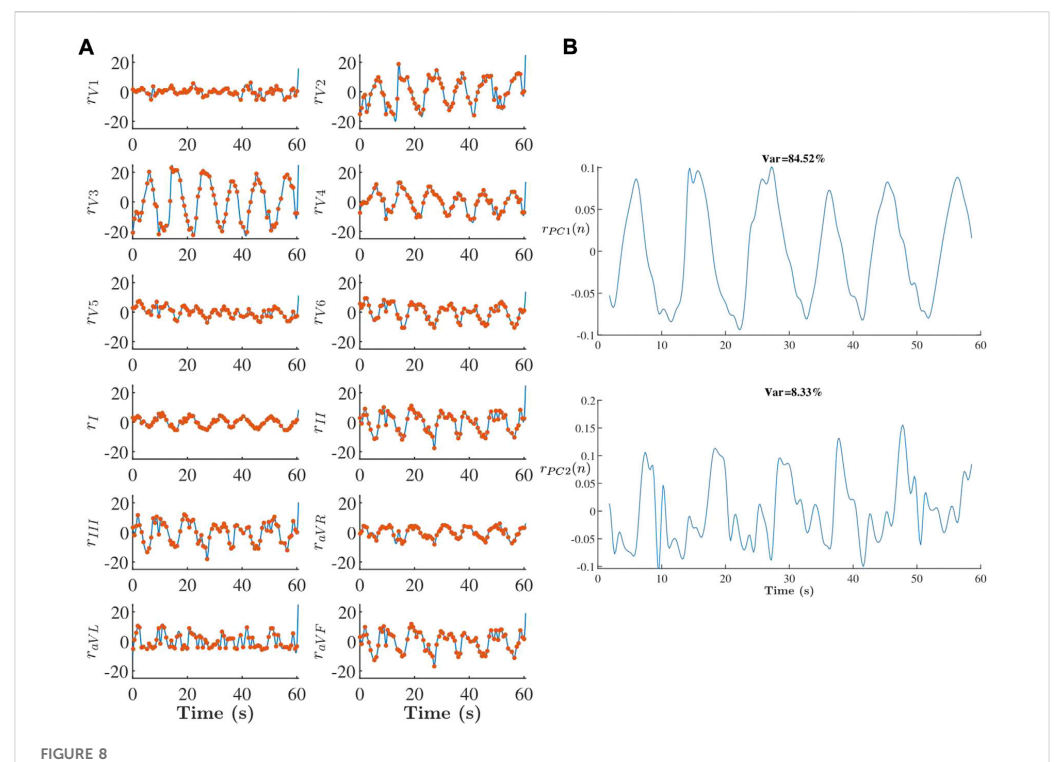


**FIGURE 7** Relative changes between  $AFR^{\rm D}$  and  $AFR^{\rm B}$  plotted versus relative between  $HR^{\rm D}$  and  $HR^{\rm B}$ 

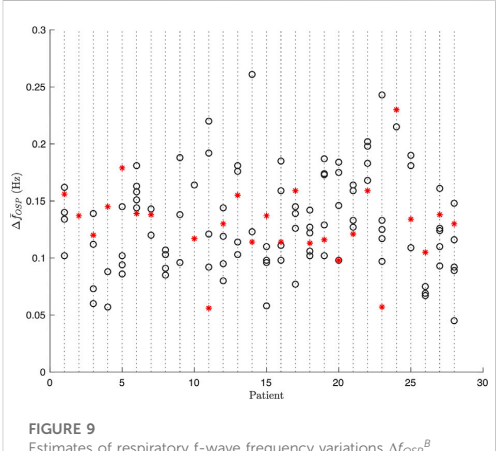
significantly higher at baseline (0.20  $\pm$  0.06) Hz than during deep breathing (0.10  $\pm$  0.01) Hz; the  $F_r$  estimated during deep breathing corresponded to the respiration frequency in controlled of the study protocol.

# 3.4 Respiratory f-wave variation

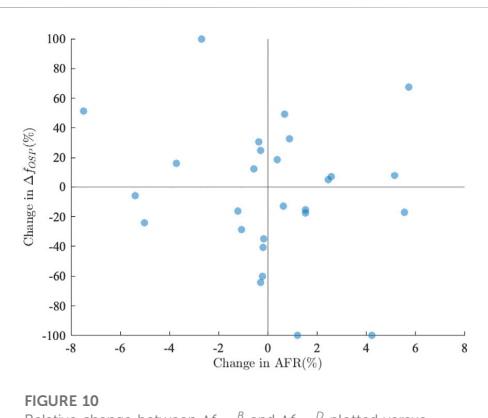
The  $\Delta \bar{f}_{OSP}$  could be obtained from all 1-min segments with a valid respiration signal, i.e., 118 out of 168.; these estimates are displayed in Figure 9. The  $\Delta f_{OSP}^B$  was 0.130 (0.045–0.260) Hz and  $\Delta f_{OSP}^D$  was 0.130 (0.056–0.230) Hz. A paired t-test showed no significant differences between baseline and deep breathing. The changes in  $\Delta \bar{f}_{OSP}$  from phase from baseline to deep breathing plotted versus the corresponding changes in the AFR in Figure 10. The changes ranged from –100 to 100% for  $\Delta \bar{f}_{OSP}$ . The Spearman method showed no correlation between changes in  $\Delta \bar{f}_{OSP}$  and changes in the AFR.



(A) Respiration signals  $r_l(n)$  (blue line) and  $r_l(i)$  (red dots) derived from 1-min ECG during deep breathing and (B) corresponding PCA components. In this example r(n) is set to  $r_{PC_1}(n)$  since it has a significant periodic component and accounts for most of the total variance.



Estimates of respiratory f-wave frequency variations  $\Delta f_{OSP}^{B}$  (black circle) and  $\Delta f_{OSP}^{D}$  (red \*) from all 1-min segments for each patient.



Relative change between  $\Delta f_{OSP}{}^B$  and  $\Delta f_{OSP}{}^D$  plotted versus relative change between  $AFR^B$  and  $AFR^D$ .

# 4 Discussion

In the present study, we propose a novel methodology, based on orthogonal subspace projection, for quantifying respiratory variations in the f-wave frequency trend. Results from analysis of simulated data show that the estimation accuracy of the proposed approach is comparable to that of our previously proposed bandpass filtering approach (Abdollahpur et al., 2021). However, the proposed approach is better suited for analysis of standard ECG recordings since it can handle time-varying

respiration (Figure 3) and provides more accurate estimates of respiratory variations at low SNR (Figure 4).

Orthogonal subspace projection has previously been proposed for removing respiratory influences in heart rate variability signal for improved estimation of sympathovagal balance (Varon et al., 2018). In contrast, in this study we aimed to keep variations in f-wave frequency trend that were linearly related to respiration and remove other variations. Such respiratory-induced f-wave frequency variations have previously been shown to be affected by parasympatetic regulation in a cohort of AF patients with complete AV block and pacemaker set at a fixed pacing rate (Abdollahpur et al., 2021).

The orthogonal subspace projection relies on an ECG-derived respiration (EDR) signal. It should be noted that standard RR interval-based algorithms for ECG-derived respiration (Widjaja et al., 2014) are not applicable during AF since variations in heart rate during AF do not originate from the sinus node. Hence, the slope range method was selected for this since previous studies (Kontaxis et al., 2019) has shown that this method is robust during AF and provides more accurate estimates compared to QRS loop rotation angle (Bailón et al., 2006) and the R-wave angle (Lázaro et al., 2014). In the slope range method f-wave suppression is not needed and its performance is less affected by the presence of f-waves (Kontaxis et al., 2019). An EDR signal is derived from each lead separately, and PCA is employed to merge respiratory information from EDR signals from different leads. It is assumed that the PCA component that has a significant periodicity in the 0.1-0.4 Hz interval and accounts for the largest part of the variations in the EDR signals contains the respiratory information. Respiration signals couldn't be obtained from 30% of the analyzed 1-min segments due to criteria defined in Section 2.4. Since this methodology aimed for the effect of timevarying respiration on the f-wave frequency, we used PCA to find respiration signal. The PCA uses a maximum-variance criteria to separate respiration signal and noise into orthogonal subspaces. Its components are sensitive to the high variance noise, which may not be the best way to find respiration signals. An alternative solution would be to use periodic component analysis (Saul and Allen, 2000), which has previously been proposed for decomposition of multilead ECG (Sameni et al., 2008) and applied for analysis of, e.g., t-wave alternans (Monasterio et al., 2010; Palmieri et al., 2021). Whereas PCA uses a maximum-variance criteria to decompose signals, periodic component analysis maximizes the periodic structure. Periodic component analysis has the advantage of being less sensitive to large amplitude noise, however, it is requires prior knowledge on the periodicity of the desired signal.

Respiratory induced f-wave frequency variations has previously been shown to be affected by parasympathetic regulation. In our previous study, (Abdollahpur et al., 2021), 5-min ECGs recorded from eight patients during controlled respiration before and after full vagal blockade were analyzed; in 50% of the patients, respiratory variation was significantly reduced after the vagal blockade. Moreover, results from computational simulations of human

atrial tissues confirmed that the pattern of the parasympathetic neurotransmitter acetylcholine release could be an important factor involved in f-wave frequency variation (Celotto et al., 2020). These results suggest that respiratory f-wave frequency variations can potentially be used to quantify ANS activity, which is of clinical interest since ANS activity is an important factor on the maintenance and progression of AF (Linz et al., 2019). For example, vagus nerve stimulation has been shown to shorten the atrial effective refractory period and suppress autonomic remodeling in dogs with obstructive apnea induced AF (Yu et al., 2017). Further, it has been shown that AF progression through cellular remodeling could be reduced by minimizing sympathetic or increasing parasympathetic tone (Bashir et al., 2019). In a recent study (Sohinki et al., 2021), investigated the impact of low-level electromagnetic fields (LL-EMF) which is specifically targeted for vagal stimulation, on AF inducibility in humans.

In present study no significant differences were found between f-wave frequency variations at baseline and during deep breathing. Several factors could contribute to this observation. Firstly, the duration of the deep breathing task was just 1 min which may not be sufficient time to observe the effect of changes in autonomic tone on the f-wave frequency trend. Further, considering the large variation of  $\Delta \bar{f}_{\textit{OSP}}$  from the 1-min segments at baseline (cf Figure 9), recordings of longer duration during deep breathing are desired for robust estimation. Secondly, the heterogeneous behavior of changes in  $\Delta \bar{f}_{OSP}$  in response to deep breathing may be due to individual differences in AF progression which may effect the ANS regulation (Linz et al., 2019). The patients in the present study have paroxysmal and persistent AF with unknown duration. However, due to the small study population subgroup analysis is not possible. Thirdly, the fluctuations in intrathoracic pressure as a result of respiration have an important effect on the heart rate during normal sinus rhythm. The effect of these fluctuations on the heart rate during AF are largely unknown. It is possible that variations in heart rate counteract the impact of respiration on the fluctuations in acetylcholine level in the atrial tissues and, as a result, the f-wave frequency variation. In the previous study, the effect of the parasympathetic activity was investigated in a cohort of AF patients with complete AV block and fixed-rate (60 beat/min) pacemaker (Abdollahpur et al., 2021) and hence the effect of changes in ANS activity induced by variations in heart rate was eliminated. In contrast, the present dataset consists of patients without a pacemaker. Finally, it should be noted that the estimation accuracy of the proposed methodology sets a lower bound for changes that can be detected (cf. Section 3.1), and we cannot exclude the possibility that there are changes below this limit that remain undetected.

# 5 Conclusion

We propose a novel orthogonal subspace projection approach to quantify respiratory variations in the f-wave frequency trend obtained from the ECG during AF. Results from simulated f-wave signals show that the proposed approach offers more robust performance in respiratory variation estimation compared to the previously proposed bandpass filtering approach. Results from analysis of clinical data were heterogeneous and no significant differences in HR, AFR and respiratory f-wave frequency variations  $\Delta \bar{f}_{OSP}$  between baseline and deep breathing were found in SCAPIS dataset.

# Data availability statement

The data analyzed in this study is subject to the following licenses/restrictions: The data is owned by Lund University. Requests to access these datasets should be directed to the steering committee of SCAPIS. Requests to access these datasets should be directed to scapis@scapis.org.

# Ethics statement

The studies involving human participants were reviewed and approved by the Written informed consent was obtained from all SCAPIS participants. The project was approved by the ethics committee at Lund University (2016/1031). The patients/participants provided their written informed consent to participate in this study.

# **Author contributions**

FS devised the project and the main conceptual ideas and was responsible for overseeing the research and providing critical insight and recommendations regarding the focus, structure, and content of the paper. MA processed the data, performed the analysis, drafted the manuscript and designed the figures. GE was responsible for the clinical data acquisition protocol. PP helped supervise the project focusing on clinical aspects. All authors contributed to the final version of the manuscript.

# **Funding**

This work was supported by the European Union's Horizon 2020 research and innovation programme under the Marie Sklodowska-Curie Grant Agreement No. 766082, the Swedish Research Council (Grant VR2019-04272) and the Crafoord Foundation (Grant 20200605). The main funding body of SCAPIS is the Swedish Heart and Lung Foundation. The study was also supported by grants from Swedish Research Council (2019-01236), Swedish Heart Lung Foundation (20200173) and grant from the Swedish state under the

agreement between the Swedish government and the county councils (ALF-project 2018-0030).

# Conflict of interest

The authors declare that the research was conducted in the absence of any commercial or financial relationships that could be construed as a potential conflict of interest.

## References

Abdollahpur, M., Holmqvist, F., Platonov, P., and Sandberg, F. (2021). Respiratory induced modulation in f-wave characteristics during atrial fibrillation. Front. Physiol. 12, 653492. doi:10.3389/fphys.2021.653492

Bailón, R., Sornmo, L., and Laguna, P. (2006). A robust method for ecg-based estimation of the respiratory frequency during stress testing. *IEEE Trans. Biomed. Eng.* 53, 1273–1285. doi:10.1109/TBME.2006.871888

Bashir, M. U., Bhagra, A., Kapa, S., and McLeod, C. J. (2019). Modulation of the autonomic nervous system through mind and body practices as a treatment for atrial fibrillation. *Rev. Cardiovasc. Med.* 20, 129–137. doi:10.31083/j.rcm.2019.03.517

Bergström, G., Berglund, G., Blomberg, A., Brandberg, J., Engström, G., Engvall, J., et al. (2015). The Swedish cardiopulmonary bioimage study: Objectives and design. *J. Intern. Med.* 278, 645–659. doi:10.1111/joim.12384

Capucci, A., Biffi, M., Boriani, G., Ravelli, F., Nollo, G., Sabbatani, P., et al. (1995). Dynamic electrophysiological behavior of human atria during paroxysmal atrial fibrillation. *Circulation* 92, 1193–1202. doi:10.1161/01.cir.92.5.1193

Celotto, C., Sánchez, C., Mountris, K. A., Abdollahpur, M., Sandberg, F., Laguna, P., et al. (2020). Relationship between atrial oscillatory acetylcholine release pattern and Fwave frequency modulation: A computational and experimental study. Comput. Cardiol, 1–4.

Chang, C.-I. (2005). Orthogonal subspace projection (osp) revisited: A comprehensive study and analysis. *IEEE Trans. Geosci. Remote Sens.* 43, 502–518. doi:10.1109/tgrs.2004.839545.

Crandall, M. A., Bradley, D. J., Packer, D. L., and Asirvatham, S. J. (2009). Contemporary management of atrial fibrillation: Update on anticoagulation and invasive management strategies. *Mayo Clin. Proc.* 84, 643–662.

Engström, G., Hamrefors, V., Fedorowski, A., Persson, A., Johansson, M. E., Ostenfeld, E., et al. (2022). Cardiovagal function measured by the deep breathing test: Relationships with coronary atherosclerosis. J. Am. Heart Assoc. 11, e024053. doi:10.1161/JAFA.121.074053

Fabritz, L., Guasch, E., Antoniades, C., Bardinet, I., Benninger, G., Betts, T. R., et al. (2016). Expert consensus document: Defining the major health modifiers causing atrial fibrillation: A roadmap to underpin personalized prevention and treatment. *Nat. Rev. Cardiol.* 13, 230–237. doi:10.1038/nrcardio.2015.194

Henriksson, M., Petrenas, A., Marozas, V., Sandberg, F., and Sornmo, L. (2018). Model-based assessment of f-wave signal quality in patients with atrial fibrillation. *IEEE Trans. Biomed. Eng.* 65, 2600–2611. doi:10.1109/TBME.2018.2810508

Holmqvist, F., Stridh, M., Waktare, J. E. P., Brandt, J., Sörnmo, L., Roijer, A., et al. (2005). Rapid fluctuations in atrial fibrillatory electrophysiology detected during controlled respiration. Am. J. Physiol. 14eart Gr. Physiol. 289, 1754–14760. doi:10.1152/ajpheart.00075.2005

Kontaxis, S., Lázaro, J., Corino, V. D., Sandberg, F., Bailón, R., Laguna, P., et al. (2019). Ecg-derived respiratory rate in atrial fibrillation. *IEEE Trans. Biomed. Eng.* 67, 905–914. doi:10.1109/TBME.2019.2923587

Krijthe, B. P., Kunst, A., Benjamin, E. J., Lip, G. Y., Franco, O. H., Hofman, A., et al. (2013). Projections on the number of individuals with atrial fibrillation in the European Union, from 2000 to 2060. Eur. Heart J. 34, 2746–2751. doi:10.1093/eurhearti/eht280

Lázaro, J., Alcaine, A., Romero, D., Gil, E., Laguna, P., Pueyo, E., et al. (2014). Electrocardiogram derived respiratory rate from qrs slopes and r-wave angle. Ann. Biomed. Eng. 42, 2072–2083. doi:10.1007/s10439-014-1073-x

Linz, D., Elliott, A. D., Hohl, M., Malik, V., Schotten, U., Dobrev, D., et al. (2019). Role of autonomic nervous system in atrial fibrillation. *Int. J. Cardiol.* 287, 181–188. doi:10.1016/j.ijcard.2018.11.091

Lip, G. Y., Nieuwlaat, R., Pisters, R., Lane, D. A., and Crijns, H. J. (2010). Refining clinical risk stratification for predicting stroke and thromboembolism in atrial fibrillation using a novel risk factor-based approach: The euro heart survey on atrial fibrillation. Chest 137, 263–272. doi:10.1378/chest.09-1584

# Publisher's note

All claims expressed in this article are solely those of the authors and do not necessarily represent those of their affiliated organizations, or those of the publisher, the editors and the reviewers. Any product that may be evaluated in this article, or claim that may be made by its manufacturer, is not guaranteed or endorsed by the publisher.

Miyasaka, Y., Barnes, M. E., Gersh, B. J., Cha, S. S., Bailey, K. R., Abhayaratna, W. P., et al. (2006). Secular trends in incidence of atrial fibrillation in olmsted county, Minnesota, 1980 to 2000, and implications on the projections for future prevalence. Circulation 114, 119–125. doi:10.1161/CIRCULATIONAHA.105.595140

Monasterio, V., Clifford, G. D., Laguna, P., and MARTInez, J. P. (2010). A multilead scheme based on periodic component analysis for t-wave alternans analysis in the ecg. *Ann. Biomed. Eng.* 38, 2532–2541. doi:10.1007/s10439-010-0029-2

Nitta, T., Ishii, Y., Miyagi, Y., Ohmori, H., Sakamoto, S.-i., and Tanaka, S. (2004). Concurrent multiple left atrial focal activations with fibrillatory conduction and right atrial focal or reentrant activation as the mechanism in atrial fibrillation. *J. Thorac. Cardiovasc. Surg.* 127, 770–778. doi:10.1016/j.jtcvs.2003.05.001

Östenson, S., Corino, V. D. A., Carlsson, J., and Platonov, P. G. (2017). Autonomic influence on atrial fibrillatory process: Head-up and head-down tilting. *Ann. Noninvasive Electrocardiol.* 22, e12405. doi:10.1111/anec.12405

Palmieri, F., Gomis, P., Ruiz, J. E., Ferreira, D., Martín-Yebra, A., Pueyo, E., et al. (2021). Ecg-based monitoring of blood potassium concentration: Periodic versus principal component as lead transformation for biomarker robustness. *Biomed. Signal Process. Control* 68, 102719. doi:10.1016/j.bspc.2021.102719

Patel, N. J., Deshmukh, A., Pant, S., Singh, V., Patel, N., Arora, S., et al. (2014). Contemporary trends of hospitalization for atrial fibrillation in the United States, 2000 through 2010: Implications for healthcare planning. Circulation 129, 2371–2379. doi:10.1161/CIRCULATIONAHA.114.008201

Platonov, P. G., Corino, V. D., Seifert, M., Holmqvist, F., and Sörnmo, L. (2014). Atrial fibrillatory rate in the clinical context: Natural course and prediction of intervention outcome. *Europace* 16, iv110-iv119. iv110-iv119. doi:10.1093/europace/euu249

Saksena, S., Skadsberg, N. D., Rao, H. B., and Filipecki, A. (2005). Biatrial and three-dimensional mapping of spontaneous atrial arrhythmias in patients with refractory atrial fibrillation. *J. Cardiovasc. Electrophysiol.* 16, 494–504. doi:10.1111/j. 1540-8167.2005.40531.x

Sameni, R., Jutten, C., and Shamsollahi, M. B. (2008). Multichannel electrocardiogram decomposition using periodic component analysis. *IEEE Trans. Biomed. Eng.* 55, 1935–1940. doi:10.1109/TBME.2008.919714

Saul, L., and Allen, J. (2000). Periodic component analysis: An eigenvalue method for representing periodic structure in speech. Adv. Neural Inf. Process. Syst. 13.

Sohinki, D., Thomas, J., Scherlag, B., Stavrakis, S., Yousif, A., Po, S., et al. (2021). Impact of low-level electromagnetic fields on the inducibility of atrial fibrillation in the electrophysiology laboratory. *Heart Rhythm O2* 2, 239–246. doi:10.1016/j.hroo.2021.04.004

Stridh, M., Meurling, C., Olsson, B., and Sörnmo, L. (2003). Detection of autonomic modulation in permanent atrial fibrillation. Med. Biol. Eng. Comput. 41, 625–629. doi:10.1007/bf02349969

Stridh, M., and Sörnmo, L. (2001). Spatiotemporal QRST cancellation techniques for analysis of atrial fibrillation. *IEEE Trans. Biomed. Eng.* 48, 105–111. doi:10.1109/10.900266

Varon, C., Lázaro, J., Bolea, J., Hernando, A., Aguiló, J., Gil, E., et al. (2018). Unconstrained estimation of hrv indices after removing respiratory influences from heart rate. *IEEE J. Biomed. Health Inf.* 23, 2386–2397. doi:10.1109/JBHL.2018.2884644

Waldo, A. L. (2003). Mechanisms of atrial fibrillation. *J. Cardiovasc. Electrophysiol.* 14, S267–S274. doi:10.1046/j.1540-8167.2003.90401.x

Widjaja, D., Caicedo, A., Vlemincx, E., Van Diest, I., and Van Huffel, S. (2014). Separation of respiratory influences from the tachogram: A methodological evaluation. *PloS one* 9, e101713. doi:10.1371/journal.pone.0101713

Yu, L., Li, X., Huang, B., Zhou, X., Wang, M., Zhou, L., et al. (2017). Impacts of renal sympathetic activation on atrial fibrillation: The potential role of the autonomic cross talk between kidney and heart. J. Am. Heart Assoc. 6, e004716. doi:10.1161/JAHA.116.004716

# Paper III





#### **OPEN ACCESS**

EDITED BY
Tomislav Stankovski,
Saints Cyril and Methodius University of
Skopie. North Macedonia

REVIEWED BY

Zoran Andrija Matić, University of Pisa, Italy Alejandro Liberos, Universitat Politècnica de València, Spain Pawel Stanislav Kostka, Silesian University of Technology, Poland

\*CORRESPONDENCE

Mostafa Abdollahpur,

mostafa.abdollahpur@bme.lth.se

<sup>†</sup>These authors have contributed equally to this work and share first authorship

RECEIVED 18 September 2024 ACCEPTED 23 May 2025 PUBLISHED 13 June 2025

#### CITATION

Abdollahpur M, Celotto C, Sánchez C, Plappert F, Östenson S, Platonov PG, Laguna P, Pueyo E and Sandberg F (2025) Tilt-induced changes in f-wave characteristics during atrial fibrillation: an experimental and computational investigation. Front. Physiol. 16:1498426. doi: 10.3389/fphys.2025.1498426

#### COPYRIGHT

© 2025 Abdollahpur, Celotto, Sánchez, Plappert, Östenson, Platonov, Laguna, Pueyo and Sandberg. This is an open-access article distributed under the terms of the Creative Commons Attribution License (CC BY). The use, distribution or reproduction in other forums is permitted, provided the original author(s) and the copyright owner(s) are credited and that the original publication in this journal is cited, in accordance with accepted academic practice. No use, distribution or reproduction is permitted which does not comply with these terms.

# Tilt-induced changes in f-wave characteristics during atrial fibrillation: an experimental and computational investigation

Mostafa Abdollahpur<sup>1</sup>\*†, Chiara Celotto<sup>2,3</sup>†, Carlos Sánchez<sup>2,3</sup>, Felix Plappert<sup>1</sup>, Sten Östenson<sup>4</sup>, Pyotr G. Platonov<sup>5</sup>, Pablo Laguna<sup>2,3</sup>, Esther Pueyo<sup>2,3</sup> and Frida Sandberg<sup>1</sup>

<sup>1</sup>Department of Biomedical Engineering, Lund University, Lund, Sweden, <sup>2</sup>BSICoS Group, Aragon Institute of Engineering Research (I3A) and IIS Aragón, University of Zaragoza, Zaragoza, Spain, <sup>3</sup>Centro de Investigación Biomédica en Red en Bioingenieria, Biomateriales y Nanomedicina (CIBER-BBN), Zaragoza, Spain, <sup>4</sup>Department of Internal Medicine and Department of Clinical Physiology, Central Hospital Kristianstad, Kristianstad, Sweden, <sup>5</sup>Department of Cardiology, Clinical Sciences and Center for Integrative Electrocardiology at Lund University (CIEL), Lund, Sweden

Introduction: This study explores transient and stationary effects of sympathetic and parasympathetic stimulation on f-wave characteristics in atrial fibrillation (AF) patients undergoing a tilt test. Transient phase is defined as the initial 2-minute interval following each postural change, reflecting immediate autonomic adaptation, whereas steady phase refers to the subsequent interval (from 3 minutes post-change until phase end) representing a stable autonomic state.

Methods: Our primary aim is to investigate how the two branches of the autonomic nervous system (ANS) influence the f-wave frequency time series (f(m)). An analysis of f(m) in terms of the mean over time  $(\mathcal{F}_f)$  and the magnitude of respiration-modulated f(m) variations ( $\Delta \mathcal{F}_{\rm f}$ ) is conducted during baseline supine rest (B), head-down tilt (HDT) and head-up tilt (HUT). We analyzed data from a previous study in which 24 patients with persistent AF underwent a tilt test protocol, during which electrocardiograms (ECGs) were recorded. A model-based method was used to extract f(m) series from the ECG. Subsequently, an orthogonal subspace projection method was employed to quantify  $\Delta \mathcal{F}_{f_r}$  considering an ECG-derived respiratory signal. Electrophysiological computational simulations were conducted on 2D and 3D human atrial persistent AF models to aid the interpretation of clinical findings. Various levels of cholinergic stimulation by acetylcholine and  $\beta$ adrenergic stimulation by isoproterenol were tested in the models. The temporal modulation of acetylcholine, representing changes associated with respiration, was cyclically modeled using sinusoidal waveforms.

**Results:** Analysis of the clinical data showed a decrease in  $\mathcal{F}_{\rm f}$  from B to HDT and an increase from HDT to HUT. During HDT,  $\Delta\mathcal{F}_{\rm f}$  initially increased in the transient phase before decreasing in the steady phase, then rose again during HUT. Analysis of the simulated data showed that increasing the concentration of Isoproterenol and/or acetylcholine resulted in a rise in  $\mathcal{F}_{\rm f}$ . Additionally, the magnitude of  $\Delta\mathcal{F}_{\rm f}$  was shown to be associated with the extent of acetylcholine fluctuation.

**Discussion:** These results suggest that changes in f-wave frequency characteristics during HUT and HDT could be linked to changes in sympathetic

activity, with parasympathetic activity possibly modulating the effects of sympathetic activity rather than being an independent driver of fibrillatory rate changes.

KEYWORDS

atrial fibrillation, autonomic nervous system, ECG processing, f-wave frequency, parasympathetic regulation, respiratory modulation

# 1 Introduction

Atrial fibrillation (AF) is the most prevalent cardiac arrhythmia characterized by irregular and rapid electrical impulses in the atria, leading to ineffective atrial contractions. This condition disrupts the heart's normal rhythm posing serious health risks, including stroke, heart failure and decreased quality of life. As the incidence of AF continues to rise globally, understanding the mechanisms underlying this condition becomes increasingly important (Hindricks et al., 2021). However, despite advancements in the treatment of AF, identifying the most suitable therapy for each individual patient remains challenging (Hindricks et al., 2021; Joglar et al., 2024). The pathophysiology of AF is complex and involves various modulators that act via multiple mechanisms. Several studies have described a role of the autonomic nervous system (ANS) in the onset and perpetuation of AF (Gould et al., 2006; Chen et al., 2014; Vandenberk et al., 2023).

In healthy subjects, the sympathetic and parasympathetic branches of the ANS work together in coordination, with sympathetic activation increasing heart rate and contractility, and parasympathetic activation decreasing them. An imbalance in the activity of the ANS can lead to electrical instability in the heart, both acting as an AF trigger and contributing to the AF substrate required for the perpetuation of AF (Dimmer et al., 1998; Herweg et al., 1998; Fioranelli et al., 1999; Tomita et al., 2003; Chang et al., 2016). Therefore, assessing ANS activity in AF patients could be highly relevant, as inter-patient variability in ANS activity might contribute to explain the large differences in the effectiveness of anti-AF therapies between patients and might help in the development of personalized treatments.

Parasympathetic stimulation (PSS) triggers the release of the neurotransmitter acetylcholine (ACh). ACh binds to muscarinic receptors in atrial myocytes, ultimately causing the activation of a specific subset of potassium channels known as G proteinactivated inwardly rectifying potassium channels. The AChactivated potassium current, denoted as IKACh, is involved in the slowing of the impulse formation at the sinoatrial node (SAN), leading to bradycardia, and in the shortening of the action potential (AP) duration (APD) and the hyperpolarization of the resting membrane potential in atrial myocytes. These effects, which are concentration-dependent, enhance the dispersion of refractoriness in atrial tissue and render the atria more susceptible to reentry and AF by reducing the wavelength of reentry (Rohr et al., 1998). Conversely, sympathetic stimulation (SS) increases the firing rate of the SAN and causes a variety of changes in the activity of atrial myocytes by activating the  $\beta$ -adrenergic signaling cascade, which triggers the phosphorylation of various cellular substrates by protein kinase A (Xie et al., 2013). Sympathetic hyperactivity induces arrhythmias by different mechanisms, including the enhancement of  $Ca^{2+}$  influx into the cell and the promotion of spontaneous releases of  $Ca^{2+}$  from the sarcoplasmic reticulum (Chelu et al., 2009). The increase in the intracellular  $Ca^{2+}$  concentration can lead to an abnormal automaticity of atrial cells, manifested as early or delayed afterdepolarizations.

During AF, the P waves of the ECG, representative of atrial activation, are replaced with irregular and erratic waveforms of smaller amplitude denoted f-waves (Sornmo, 2018). With the aim to characterize the atrial electrical activity during AF, the f-wave frequency has received considerable clinical attention (Lankveld et al., 2014; Platonov et al., 2014). Particularly, the atrial dominant frequency, often referred to as the atrial fibrillatory rate and here denoted as  $\mathcal{F}_f$ , can be derived either through spectral (frequency domain) analysis by identifying the frequency presenting the highest peak in the power spectral density of the fwave signal (Park et al., 2019), or through time-domain analysis of the ECG using model-based approaches (Henriksson et al., 2018a). Previous studies have shown that variations in ANS activity can result in f-wave frequency variations, an aspect which can not be studied by restricting the analysis to the dominant frequency  $\mathcal{F}_f$ , but requires detailed analysis of the f-waves frequency time series f(m) (Abdollahpur et al., 2021; Abdollahpur et al., 2022). Slow controlled breathing (0.125 Hz) in persistent AF (psAF) patients with permanent pacemaker has been shown to cause f(m) modulation at the respiration frequency (Stridh et al., 2003; Holmqvist et al., 2005), with the magnitude of the respiratory f-wave frequency modulation  $\Delta F_f$ being reduced after vagal blockade (Abdollahpur et al., 2021). This suggests a link between f(m) modulation through respiration and parasympathetic activity.

Also, we conducted computational simulations to shed light on the mechanisms underlying those findings (Celotto et al., 2022; Celotto et al., 2024). We evaluated the role of the spatiotemporal release pattern of ACh, considered to vary in phase with inspiration and expiration, in modulating the f-wave frequency and reported that changes in the ACh concentrations were linearly correlated with changes in the f-wave frequency.

A common way used in clinical settings to assess autonomic function is the tilt test, which can provide valuable information about the ability of the ANS to regulate blood pressure and heart rate in response to postural changes (Freeman, 2006). A study examined changes in the f-wave frequency in response to changes in ANS activity induced by head-down tilt (HDT) and head-up tilt (HUT) in 40 patients with psAF and reported a reduction in the f-wave frequency during HDT compared to the baseline (B) and an increase in f-wave frequency in response to HUT (Östenson et al., 2017). Our further analysis of the data from that study showed that a change in the sign of the derivative of the population averaged f-wave frequency trends is noticeable after the initial 2 min of each

5-minute tilt phase (Plappert et al., 2022). This may indicate an initial transient response of the ANS (Fois et al., 2022), after which the system begins to return to baseline.

In this study, we investigated the relationship between autonomic influences and changes in  $\mathcal{F}_{P}$ ,  $\Delta\mathcal{F}_{f}$  and heart rate ( $\mathcal{F}_{HR}$ ) during HUT and HDT in psAF patients. To assess both the transient and the steady-state responses, we separately analyzed the ECG signals for the first 2 and the last 3 min of baseline, HDT and HUT.

To provide further insight into the autonomic modulation of changes in heart rate and f-wave characteristics, we developed 2D and 3D atrial computational models under different combinations of cholinergic and  $\beta$  – adrenergic stimulation. Preliminary results of this study were presented at the 2023 Computing in Cardiology conference (Celotto et al., 2023).

# 2 Materials and methods

The description of the clinical tilt test data is provided in Section 2.1. A brief description of the methods for ECG-based estimation of heart rate  $\mathcal{F}_{HR}$ , f-wave frequency  $\mathcal{F}_f$ , and the respiratory modulation quantified in terms of  $\Delta \mathcal{F}_f$  is provided in Sections 2.2–2.4 (Abdollahpur et al., 2022). The human atrial models with incorporation of autonomic effects and the numerical simulations are expanded from Section 2.5 to Section 2.8 (Celotto et al., 2023; 2024). Section 2.9 describes the statistical analysis performed to identify significant differences in the extracted characteristics between B, HDT and HUT.

# 2.1 Materials

The present study is based on analysis of data acquired in a previous study (Östenson et al., 2017) where patients admitted with persistent AF and planned for elective cardioversion were screened for participation. Patients with abnormal levels of thyroid hormones, severe renal failure requiring dialysis, or heart valve disease were excluded as well as were patients ablated for AF or on any of the Class I or Class III antiarrhythmic drugs. The 40 patients that were included in that study were all on anticoagulant therapy. Table 1 lists the clinical characteristics of this population. Standard 12-lead ECGs, sampled at 1 kHz, were recorded in three different phases: 5 minutes in the baseline supine rest (B) position (0°), 5 minutes in the HDT position (-30°), and 5 minutes in the HUT position (+60°), respectively. Details about the tilt test protocol can be found in Östenson et al. (2017). In this study, we analyzed ECG recordings from a subgroup of 29 patients, since 11 patients were excluded due to missing ECG data. This subgroup is consistent with the subgroup previously examined in Plappert et al. (2022).

## 2.2 ECG preprocessing

The ECG preprocessing, ectopic beat detection, and QRST cancellation were performed using the CardioLund<sup>®</sup> ECG parser, developed by CardioLund Research AB, Lund, Sweden. The original ECG sampling rate of 1 kHz provides high-resolution suitable for QRS cancellation and f-wave extraction. However, this high

TABLE 1 Clinical characteristics of the original study population (Östenson et al., 2017).

Variable	Value
Age (years)	64 ± 12
Gender (male/female)	25/15
AF duration (days)	90 (1-350)
Congestive heart failure	8
Hypertension	32
Ischemic heart disease	4
Diabetes mellitus	3
Beta-blockers	32
Digoxin	7

sampling rate would lead to a considerable computational burden in subsequent f-wave analysis which is not needed given that fwave frequency contents can be assumed constrained well below 25 Hz. Consequently, the extracted f-wave signals from lead V1 were resampled to 50 Hz to obtain an f-wave signal (x(n)). Each recording was split into six segments; first 2 minutes of baseline rest (B1), last 3 minutes of baseline rest (B2), first 2 minutes of HDT corresponding to the transient phase (HDT1), last 3 minutes of HDT corresponding to the steady-state phase (HDT2), first 2 minutes of HUT corresponding to the transient phase (HUT1) and last 3 minutes of HUT corresponding to the steady-state phase (HUT2). The baseline segment was subdivided into B1 and B2 to improve the reliability of phase comparisons. Ectopic beats were disregarded for computation of the average heart rate  $\mathcal{F}_{HR}$  in each phase (B1, B2, HDT1, HDT2, HUT1, HUT2), by assessing the consistency in the shape and timing of each beat relative to the established normal template, identifying those that deviate significantly from the template as ectopic beats.

# 2.3 Estimation of the f-wave frequency trend from patients' ECGs

A harmonic f-wave model was used to estimate the high-resolution trend of the f-wave frequency, f(m) (Henriksson et al., 2018b). This model represents the f-wave signal as the sum of a complex exponential signal with the fundamental frequency f and its second harmonic (Equation 1):

$$s(n; \theta) = \sum_{p=1}^{2} A_{p} e^{j(p2\pi f n/f_{s} + \phi_{p})},$$
 (1)

The model parameters  $\boldsymbol{\theta} = [f \ A_1 \ A_2 \ \phi_1 \ \phi_2]^T$  were estimated by fitting the harmonic model to the analytic equivalent of x(n), denoted as  $x_a(n)$ , using a maximum likelihood approach. The fitting process was performed on 0.5-s segments of  $x_a(n)$ , with 20 ms overlapping, to obtain the f-wave frequency trend f(m) sampled at

50 Hz. For the fitting, the fundamental frequency f was constrained to the interval  $[f_0 \pm 1.5]$  Hz, where  $f_0$  corresponds to the maximum peak in the interval [4, 12] Hz of the Welch periodogram of each x(n) recording.

To assess the accuracy of the fitted model, a signal quality index S was computed (Equation 2):

$$S = 1 - \frac{\sigma_{\hat{e}}}{\sigma_r} \tag{2}$$

where  $\sigma_{\hat{e}}$  and  $\sigma_{x_a}$  denote the standard deviation of the model error and  $x_a(n)$ , respectively. In this study,  $\mathcal{S}$  was computed for non-overlapping 5-s segments. Only segments with  $\mathcal{S} > 0.3$  were considered for further analysis, as previous studies have indicated that  $\mathcal{S}$  larger than 0.3 is sufficient for accurate estimation of f(m) (Henriksson et al., 2018b). Details on the estimation of  $\mathcal{S}$  can be found in Abdollahpur et al. (2022). If more than 10% of the segments in an ECG recording were considered insufficient for further analysis, the recording was completely excluded from further analysis. The f-wave frequency  $\mathcal{F}_f$  in each phase (B1, B2, HDT1, HDT2, HUT1, HUT2) was obtained by calculating the median of the corresponding f(m) trend within each phase.

# 2.4 Respiratory f-wave modulation

An orthogonal subspace projection technique (Varon et al., 2019) was used to extract respiration-related fluctuations in the f(m) series as proposed in Abdollahpur et al. (2022). This procedure was performed separately for each phase (B1, B2, HDT1, HDT2, HUT1, HUT2). For the extraction of an ECG-derived respiration signal, a lead-specific respiration signal was extracted from each ECG lead separately by employing the slope range approach (Kontaxis et al., 2019), which uses the difference between the maximum and minimum derivative in the QRS interval to quantify variations in the QRS morphology related to respiratory activity. Subsequently, a joint-lead respiration signal, r(m), was obtained by employing the periodic component analysis ( $\pi CA$ ) approach proposed by (Plappert et al., 2024); an estimate of the respiration rate ( $\mathcal{F}_{RR}$ ) was also provided by this method.

With r(m) in a window of M samples, an  $(M-q) \times q$  subspace projection matrix, V, was constructed, where each column consisted of a delayed version of r(m) (Equations 3, 4):

$$V = [r_0, r_1, \dots, r_d, \dots, r_q], \qquad (3)$$

$$\mathbf{r}_d = [r(1+d), r(2+d), \dots, r(M-q+d)]^T.$$
 (4)

Then, f(m) was detrended by subtracting its mean, and the resulting signal, denoted as  $\tilde{f}(m)$ , was projected onto the respiratory subspace generated by V to estimate the respiratory-related variations (Varon et al., 2019) (Equation 5):

$$f_r = V(V^{\mathsf{T}}V)^{-1}V^{\mathsf{T}}\tilde{f},\tag{5}$$

where  $\tilde{f} = [\tilde{f}(1), \dots, \tilde{f}(M-q)]^T$ . The vector  $f_r = [f_r(1), \dots, f_r(M-q)]^T$  represents the variations in the f-wave frequency series linearly related to the respiration signal r(m).

The average peak amplitude in  $f_r$ , considered as an estimate of the magnitude of the respiratory-induced f-wave frequency

variations  $(\Delta \mathcal{F}_f)^1$ , was determined by (Equation 6):

$$\Delta \mathcal{F}_{f} = \sqrt{\frac{2 \cdot f_{r}^{\mathsf{T}} f_{r}}{M - q}}.$$
 (6)

Furthermore, to quantify the relative contribution of respiration to the variations in  $f_r$  compared to  $\tilde{f}$ , the relative power of  $f_r$ , denoted as  $\mathcal{P}_r(\%)$ , was computed as (Equation 7):

$$\mathcal{P}_r(\%) = \frac{f_r^{\mathsf{T}} f_r}{\tilde{f}^{\mathsf{T}} \tilde{f}} \times 100. \tag{7}$$

# 2.5 2D and 3D human atrial electrophysiological models

Computational models of human atrial electrical activity were built to run simulations that could aid in the interpretation of the clinical data recorded during tilt tests in patients with psAF. Stationary conditions with different levels of SS and PSS were simulated to gain insight into their contribution to f-wave frequency characteristics.

Human atrial electrical activity was simulated both in 2D square sheets of tissue as well as in 3D biatrial anatomical models representative of psAF. The 2D models represented square pieces of  $7 \times 7$  cm<sup>2</sup> tissue, discretized in square elements of 200- $\mu$ m side. A uniform bottom-to-top fiber direction was assigned to the tissues. For the 3D biatrial models, the anatomy was in all cases defined as in Ferrer et al. (2015). The 3D anatomical model was discretized in a multi-layer mesh using linear hexahedral elements with an average edge length of 300  $\mu$ m. This resulted in a total of 754,893 nodes and 515,010 elements. The model included detailed regional descriptions of fiber direction and functional heterogeneity, considering eight regions with different electrophysiological properties (Celotto et al., 2024).

In the 3D models, we used longitudinal conductivity values and transverse to longitudinal conductivity ratios adapted from (Ferrer et al., 2015), as detailed in (Celotto et al., 2024). With these conductivity values in healthy atrial tissue (without fibrosis and without electrical remodeling), the total activation time (TAT) was 130 ms, which is consistent with values reported in the literature. Introducing electrical remodeling caused a slight increase in TAT to 134 ms. Additional incorporation of fibrosis elevated TAT to 180 ms, consistent with findings from (Wesselink et al., 2022) in patients with psAF. In the 2D models, we applied the same longitudinal conductivity values and transverse-to-longitudinal conductivity ratios as those used in the left atrial (LA) region of the 3D model. This configuration resulted in a longitudinal conduction velocity (CV) of 94.12 cm/s without fibrosis and 58 cm/s with fibrosis. These findings are consistent with values reported in previous studies involving patients with and without AF (Bayer et al., 2019).

The electrophysiological activity of human atrial cardiomyocytes was described by the Courtemanche AP model (Courtemanche et al., 1998). All the myocardial nodes in the 2D tissue mesh were assigned with the same electrophysiological

<sup>1</sup> In the original publication Abdollahpur et al. (2022), this  $\Delta \mathcal{F}_{\text{f}}$  was denoted  $\Delta f_{\text{OSP}}$  to indicate that it was estimated with the Orthogonal Subspace Projection method.

characteristics representative of LA tissue. In the 3D models, the Courtemanche model was adapted to represent different atrial regions by varying the ionic current conductances as in Ferrer et al. (2015). These adjustments were made based on experimental observations regarding AP morphology and duration reported in several studies (Wang et al., 1990; 1993; Li et al., 2001; Cha et al., 2005; Seemann et al., 2006).

Parasympathetic stimulation effects were described by introducing the ACh-activated potassium current I<sub>KACh</sub> in the cellular models. The IKACh formulation was based on the study by Kneller et al. (2002) and subsequently updated as proposed by Bayer et al. (2019). The effects of  $\beta$ -adrenergic stimulation were modeled as proposed in González de la Fuente et al. (2013). In brief, the effects of the nonspecific  $\beta$ -adrenergic agonist Isoproterenol (Iso) were modeled by increasing the maximal conductances of the L-type calcium current (ICaL) and the slow delayed rectifier potassium current (I<sub>Ks</sub>) and by decreasing the maximal conductance of the transient outward potassium current (Ita), following the experimentally reported concentration-dependent conductance modulation curves reported in González de la Fuente et al. (2013). Specifically, for  $0.005 \,\mu\mathrm{M}$  Iso, the conductance values were increased by 169% for  $g_{CaL}$ , by 76.6% for  $g_{Ks}$ , and decreased by 54.8% for  $g_{to}$ . At the higher concentration of 1  $\mu$ M, these values were increased by 300% for  $g_{CaL}$ , by 79.2% for  $g_{Ks}$ , and decreased by 61.4% for  $g_{to}$ .

Since the simulations aimed to replicate conditions similar to those observed in psAF patients, both electrical and structural remodeling (Sanders et al., 2003) was incorporated into the models, as follows. Electrical remodeling associated with psAF was represented by reducing the conductances of Ito, ICaI and the ultrarapid delayed rectifier potassium current (IKur) by 50%, 70% and 50%, respectively, as in Courtemanche (1999), by increasing the conductance of the inward rectifier potassium current (I<sub>K1</sub>) by 100% (Dobrev et al., 2001), and by increasing the conductance of IKs by 100% (González de la Fuente et al., 2013). To incorporate psAF-induced structural remodeling in the 2D and 3D models, we introduced 20% diffuse fibrosis based on the ranges reported experimentally (Platonov et al., 2011). Specifically, we randomly selected 20% of the nodes based on a uniform distribution and we assigned them the MacCannell active fibroblast computational model (MacCannell et al., 2007). The fibroblast-fibroblast gap-junctional conductance was reduced 4-fold with respect to the myocyte-myocyte conductance. When myocytes were coupled to fibroblasts, the junctional conductance was linearly adjusted depending on the number of fibroblasts coupled to a myocyte.

# 2.6 Simulated ACh and Iso release patterns

In both the 2D and 3D models, 30% of nodes were randomly chosen to be either ACh- or Iso-release nodes. This resulted in four possible scenarios: nodes that released only ACh, nodes that released only Iso, nodes that released both Iso and ACh and nodes that released neither Iso nor ACh.

To model the respiratory modulation of ACh concentration, the temporal pattern of ACh release was modeled as cyclically varying following a sinusoidal waveform with a frequency equal to the average respiration frequency measured in patients (0.14 Hz), see Table 2. A mean ACh level of 0.05  $\mu$ M was considered, while two different peak-to-peak variation ranges of ACh ( $\Delta$ ACh) equal to 0.1 and 0.025  $\mu$ M, were tested, all of them laying within the ACh ranges used in previous studies (0.0 – 0.1  $\mu$ M) (Bayer et al., 2019). The effects of β-adrenergic stimulation were simulated by administration of Iso at spatially and temporally fixed concentrations of 0.0, 0.005 and 1.0  $\mu$ M.

## 2.7 Numerical methods and simulations

To establish steady-state conditions, single cells were paced at a fixed cycle length (CL) of 800 ms over a period of 16 min (Celotto et al., 2024). The resulting steady-state values of the cellular model's state variables were used to initialize the multi-cellular models.

In the 2D models, four stimuli at a CL of 800 ms were administered at the lower edge of the 2D tissue to pre-excite the model. Subsequently, a cross-stimulation protocol (S1-S2) was employed to induce a rotor. The first stimulus (S1) was applied at the lower edge of the tissue, while the second stimulus (S2) was applied onto a 3.5 by 3.5 cm square at the bottom right corner.

In the 3D whole-atria models, an S1-S2 protocol was applied to trigger arrhythmias too. The S1 stimulus was administered at a line connecting the region between the superior and inferior left pulmonary veins with the area between the right pulmonary veins. Subsequently, the S2 stimulus was applied parallel to the first one starting from the inferior left PV and covering only half of the length of the S1 line (Celotto et al., 2024).

Following the delivery of the S1 stimulus, the simulations were conducted for a duration of 24 s, and results are presented for the last 10 s.

In both the 2D and 3D simulations, the S1-S2 intervals varied mainly based on the underlying Iso concentration, ranging from 130 ms at Iso =  $0\mu$ M, to 110 ms at the highest concentration of Iso =  $1\mu$ M.

Electrical propagation in the atria was described by the monodomain model and solved with the Finite Element Method in combination with the operator splitting numerical scheme using the software ELVIRA (Heidenreich et al., 2010).

# 2.8 Estimation of the simulated atrial activation frequency trend

From the simulations, transmembrane voltage time series were extracted from 169 uniformly distributed points in the 2D tissue models and 223 points manually selected to be approximately uniformly distributed in the 3D whole-atria models. For each extracted point c, the time instant  $t_{c,i}$  corresponding to the maximum upstroke velocity of the i-th action potential was determined.

The simulated instantaneous frequency,  $f_c^s(m)$ , was computed by resampling the series  $1/(t_{c,i+1}-t_{c,i})$  to a sampling frequency of 10 Hz, for all beat indices i in the recording. The time series  $f_c^s(m)$  was subjected to power spectral analysis. Spectral "peak-conditioned" selection was performed as in Bailon et al. (2006) so that the series whose spectrum was not sufficiently peaked were discarded. The frequency trend of this simulated signals,  $f^s(m)$ ,

Median (IQR)	В		HDT		HUT	
mean ± SD	B1	B2	HDT1	HDT2	HUT1	HUT2
$\mathcal{F}_{\mathrm{f}}\left(\mathrm{Hz}\right)$	6.74 (6.36 – 7.30)	6.69 (6.43 – 7.35)	6.49 (6.32 – 7.10)*,***	6.55 (6.13 – 6.91)**	6.77 (6.42 – 7.27) <sup>†,‡</sup>	6.72 (6.48 – 7.22) <sup>‡</sup>
$\mathcal{F}_{HR}$ (bpm)	93.5 (80 – 105)	89.75 (80 – 104)	90.25 (80 – 106)**	93.5 (82 – 107)**,†	98.5 (84.5 – 114) <sup>†,‡</sup>	96 (82 – 111)#
$\mathcal{F}_{RR}$ (Hz)	0.13 (0.11 – 0.16)	0.13 (0.11 – 0.24)	0.15 (0.12 – 0.21)	0.16 (0.12 – 0.25)	0.12 (0.11 – 0.14)	0.15 (0.12 – 0.16)
$\Delta \mathcal{F}_{\mathrm{f}}\left(\mathrm{Hz}\right)$	0.077 ± 0.028	0.070 ± 0.025	0.090 ± 0.038**	$0.063 \pm 0.019^{\dagger}$	$0.081 \pm 0.022^{\ddagger}$	$0.079 \pm 0.024^{\ddagger}$
P <sub>r</sub> (%)	2.84 ± 1.69	1.97 ± 1.04*	3.22 ± 2.21**	$1.66 \pm 0.85^{\dagger}$	$2.86 \pm 1.40^{\ddagger}$	2.36 ± 1.37

TABLE 2 Results of the evaluated parameters  $\mathcal{F}_{\text{fr}}$ ,  $\mathcal{F}_{\text{HR}}$ ,  $\mathcal{F}_{\text{FR}}$ ,  $\Delta \mathcal{F}_{\text{f}}$  and  $\mathcal{P}_{\text{r}}$  in the tilt test phases B1, B2, HDT1, HDT2, HUT1, and HUT2.

Significant differences are denoted by "\*" for B1, "\*" for B2, "†" for HDT1, "‡" for HDT2, and "#" for HUT1.

was computed as the mean over the remaining  $f_c^c(m)$  series for all points c not discarded for the analysis [more details can be found in Celotto et al. (2024)].

 $\mathcal{F}_f^s$  was calculated as the median over time of f(m).  $\Delta \mathcal{F}_f^s$  was computed using the method described in Section 2.4, considering as the respiration signal a sinusoidal waveform of frequency equal to 0.14 Hz.

# 2.9 Statistical analysis

The Lilliefors test was employed to assess the normality of the data. Results for Gaussian-distributed variables are presented as mean±std, while results for non-Gaussian-distributed variables are presented as median (lower quartile–upper quartile). The Wilcoxon signed-rank test was used to assess statistically significant differences in  $\mathcal{F}_{\rm HR},\,\mathcal{F}_{\rm P}\,\Delta\mathcal{F}_{\rm P}$  and  $\mathcal{P}_{\rm r}$  between phases. To account for multiple comparisons, a Bonferroni correction was applied, adjusting the statistical significance threshold. The corrected significance level was set at p<0.05/n, where n is the number of pairwise comparisons made.

Figure 1 illustrates the comparisons that were performed in the study. Specifically, we compared each sub-phase (transient and steady-state) with the immediately preceding sub-phase. Additionally, we compared each steady-state phase with the previous steady-state one and each transient phase with the previous transient one.

# 3 Results

An example of an original ECG signal and the corresponding extracted f-wave signal, estimated f-wave frequency trend f(m), extracted respiratory signal r(m), and respiratory-related f-wave frequency variations  $f_r(m)$ , from a 30-s ECG segment during phase B2, are displayed in Figure 2.

The estimated f-wave frequency trend f(m) from the entire recording of one patient is displayed in Figure 3, highlighting the variations in f(m) across phases (B1, B2, HDT1, HDT2, HUT1, HUT2). The signal quality index  $\mathcal{S}$ , displayed for a 1-min subsegment of phase B1, shows that the f-wave signal quality is

sufficient for analysis in a majority of the subsegment and pinpoints critical areas where the estimated f-wave frequency trend f(m) is considered unreliable.

# 3.1 Heart rate and f-wave frequency

Five out of the 29 patients were excluded entirely from further analysis based on the exclusion criteria outlined in Section 2.3 and thus the results are based on 24 patients. For the remaining 24 patients, 2.2% of the 5-s segments in B1, 1.7% in B2, 0.8% in HDT1, 2.9% in HDT2, 4.3% in HUT1, and 1.9% in HUT2 exhibited  $\mathcal{S} < 0.3$ , leading to their exclusion from further analysis. Regarding the prevalence of ectopic beats in our analyzed segments, they accounted for approximately 1.07% of the total beats identified.

Table 2, first row, shows the results for  $\mathcal{F}_f$  in the first 2 min (transient) and last 3 min (steady state) of each tilt phase B, HDT and HUT. As can be seen from the table, there was a significant reduction in  $\mathcal{F}_f$  from B2 to HDT1 and no significant differences between HDT1 and HDT2. Conversely, a substantial rise from HDT2 to HUT1 was observed, again with no significant differences between HUT1 and HUT2. The second row in Table 2 shows results for  $\mathcal{F}_{HR}$ . A significant increase was observed from B2 to HDT1, from HDT1 to HDT2, from HDT2 to HUT1 and finally a significant decrease was observed from HUT1 to HUT2. Focusing on the steady state, a significant increase was observed from B2 to HDT2. Focusing on the transients, a significant increase was observed from HDT1 to HUT1.

The subplots (a) and (b) of Figure 4 show the values of  $\mathcal{F}_{HR}$  and  $\mathcal{F}_f$  for each patient during each phase segment. The colors and shape of the points display the individual behavior of each patient in terms of increase (green squares), decrease (red triangles) and minimal variation (black circles, differences thives 1%) with respect to the previous phase segment, for  $\mathcal{F}_f$  and  $\mathcal{F}_{HR}$ , respectively. The behavior of  $\mathcal{F}_{HR}$  and  $\mathcal{F}_f$  notably varies among individuals. Note that heart rate  $\mathcal{F}_{HR}$  is expressed in bpm for consistency with other works and clinical conventions. However, it can be easily converted to Hz by dividing by  $60:\mathcal{F}_{HR}(Hz)=\mathcal{F}_{HR}(bpm)/60$ . This conversion highlights the significantly higher frequency of f-waves compared to R-peaks repetition, i.e., the heart rate.

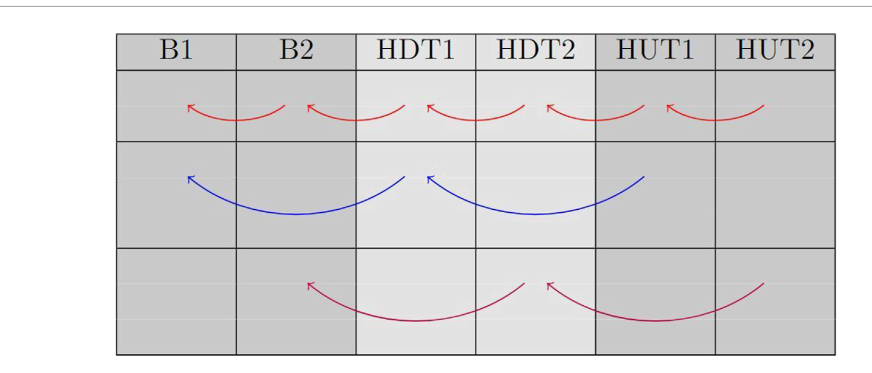
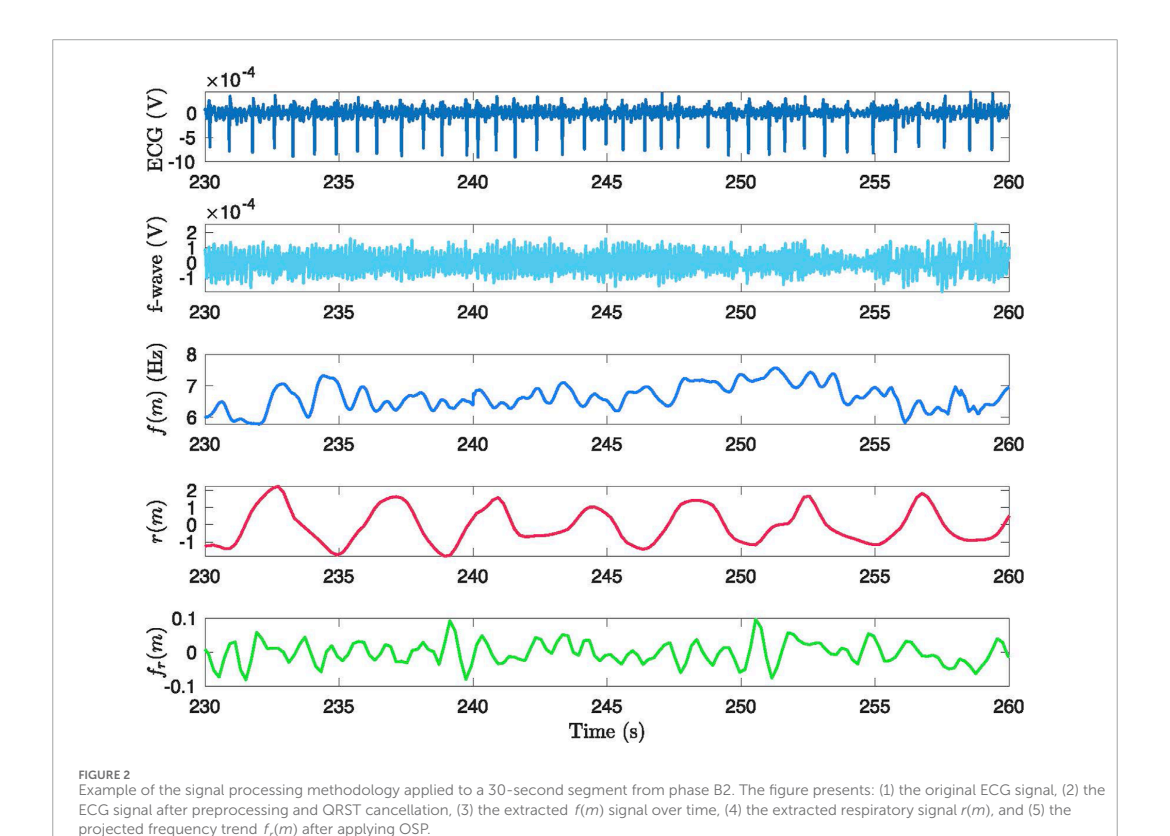


FIGURE 1
This table displays the comparisons that were made between phases. Red arrows represent comparisons between each sub-phase and the previous one; blue arrows represent comparison between transient phases; magenta arrows represent comparison between steady-state phases.



# 3.2 Respiration related f-wave variation and its relative power

The third row of Table 2 presents the results for the respiration rate  $\mathcal{F}_{RR}$  in each of the analyzed phase segments. There were

no significant changes in respiration rate between the tilt phases. The fourth row of Table 2 shows the results for  $\Delta \mathcal{F}_f$ . There was a significant increase in  $\Delta \mathcal{F}_f$  from B2 to HDT1 and a significant decrease from HDT1 to HDT2. Also, there was a significant increase from HDT2 to HUT1. Comparing steady-states, there

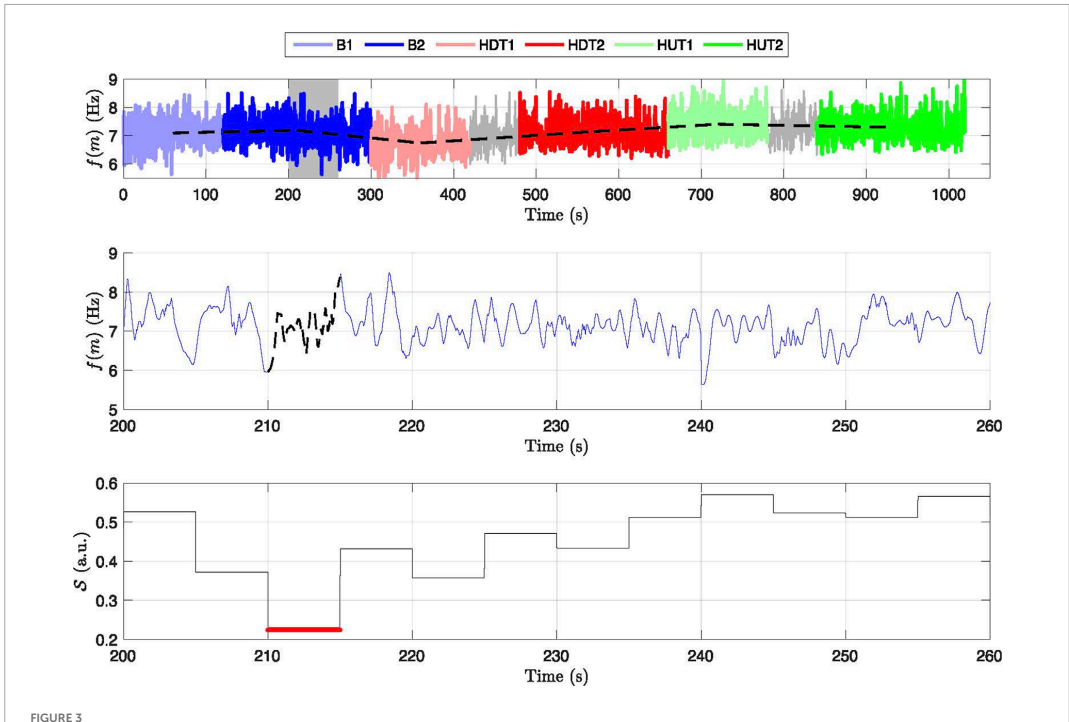


FIGURE 3 Frequency variation and signal quality across different phases for a subject. Top panel: Displays the frequency trend, f(m), across baseline (B1, B2), head-down tilt (HDT1, HDT2), and head-up tilt (HUT1, HUT2) phases, with distinct colors marking the different phases. Dashed lines connect the mean f-wave frequency in each phase. Middle panel: Zoom in of a 60-s interval of f(m) corresponding to the shaded area in the top panel with dashed black line indicating segments where f(m) is excluded from further analysis. Bottom panel: Signal quality index S with red line indicating values below the threshold 0.3.

are no significant differences between phases, while considering transients there is a significant increase from HDT2 to HUT2. The last row of Table 2 shows the results for  $\mathcal{P}_r$ , indicating a significant decrease from B1 to B2, a significant increase from B2 to HDT1, a significant decrease from HDT1 to HDT2 and, finally, a significant increase from HDT2 to HUT1, similar to what was observed for  $\Delta \mathcal{F}_f$ .

The subplots (c) and (d) of Figure 4 illustrate the comparison of  $\Delta \mathcal{F}_f$  and  $\mathcal{P}_r$  in each patient for each phase segment. The colors and shape of the points display the individual behavior of each patient in terms of increase (green squares), decrease (red triangles) and minimal variation differences thives 1%) with respect to the previous phase (black circles), for  $\Delta \mathcal{F}_f$  and  $\mathcal{P}_r$ , respectively. Both  $\Delta \mathcal{F}_f$  and  $\mathcal{P}_r$  exhibited heterogeneous behavior across different patients.

# 3.3 The f-wave frequency analysis from computational simulations

In the 2D tissue models, a single stable rotor was initiated after application of the S1-S2 protocol, while in the 3D biatrial models, S1-S2 stimulation was able to generate multiple stable rotors, as illustrated in Figure 5 and in the videos provided in the Supplementary Material. An increase in the number

of stable rotors (from 1 to 3) was observed when adding 0.005 or 1  $\mu$ M Iso to ACh varying from 0 to 0.1  $\mu$ M. When  $\Delta$ ACh was 0.025  $\mu$ M, the addition of 1  $\mu$ M Iso increased the number of rotors from 1 to 5.

Table 3 reports the values of  $\mathcal{F}_f^s$  and  $\Delta \mathcal{F}_f^s$  for the different simulations. Figure 6 shows the temporal evolution of  $f^s(m)$  compared to ACh concentration for each case. Additionally, Supplementary Figure S2S in the Supplementary Material displays the APD at 90% repolarization (APD<sub>90</sub>) over time across different locations within the tissue for the 3D simulations. 2D and 3D biatrial simulations render qualitatively and quantitatively comparable results in terms of  $f^s(m)$ , with  $\mathcal{F}_f^s$  ranging from 7.12 Hz to 9.12 Hz in the different simulated cases. It can be observed that an increase in the minimum ACh level (from 0 μM to 0.0375 μM, corresponding to ΔACh = 0.025 μM) resulted in slightly higher  $\mathcal{F}_f^s$  values, with increases of 0.04–0.32 Hz in both the 2D and 3D simulations.

 $\beta$ -adrenergic stimulation via Iso significantly increased  $\mathcal{F}_f^s$  in all cases, with effects dependent on the concentration used (Table 3). In both the 2D and 3D models, an Iso concentration of 0.005  $\mu$ M resulted in an increase in  $\mathcal{F}_f^s$  ranging from 0.31 to 1.13 Hz compared to the control condition (no Iso). At a higher Iso concentration of 1  $\mu$ M, the increase was more pronounced, ranging from 0.81 to 1.75 Hz (Figure 6).

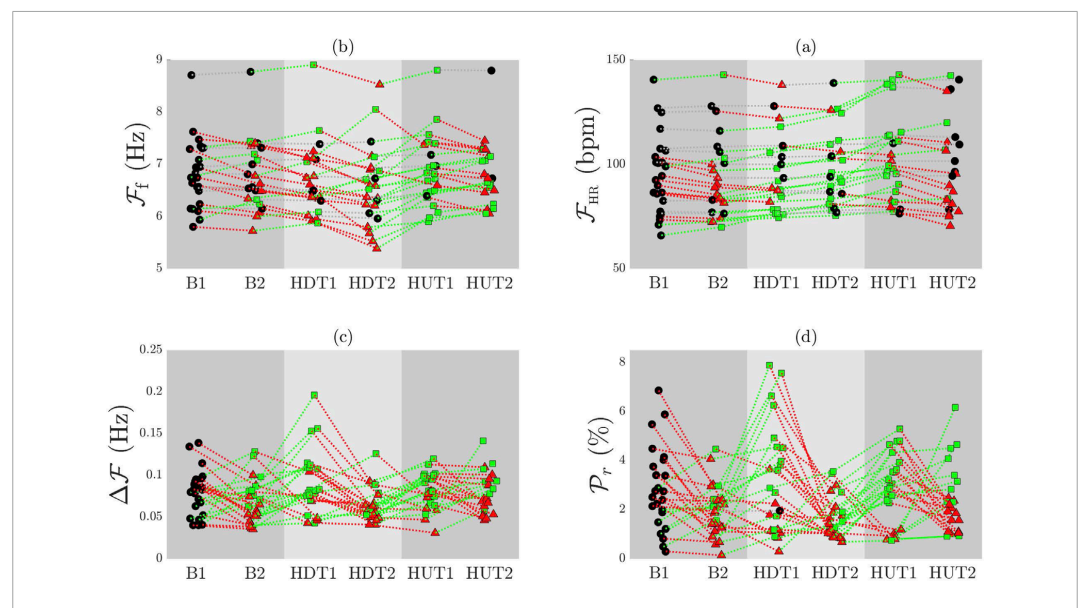
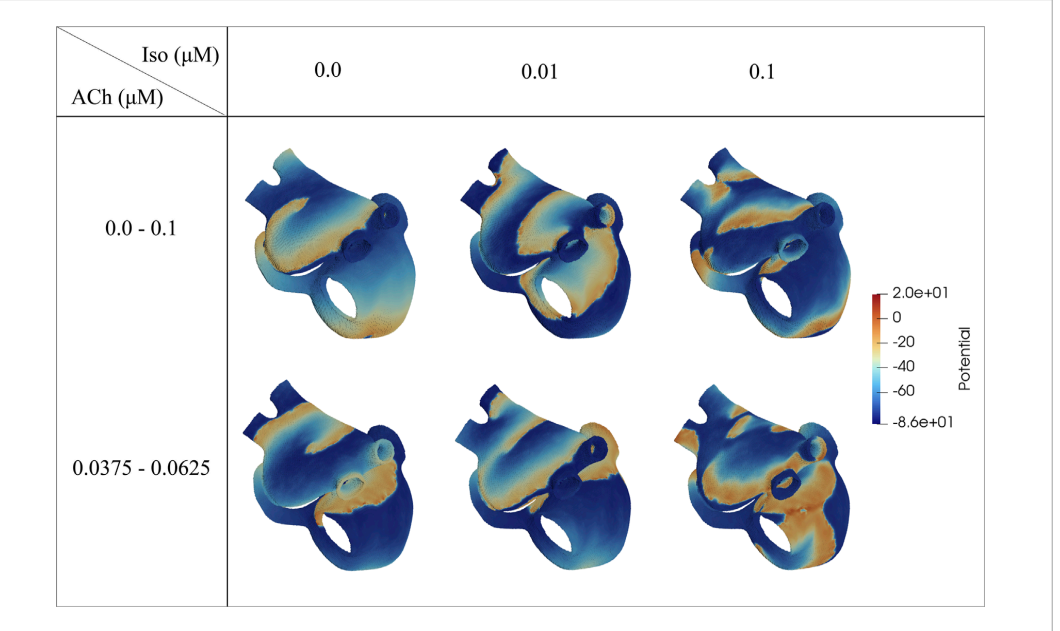


FIGURE 4 Individual patient trends for  $\mathcal{F}_{HR}$  (a),  $\mathcal{F}_f$  (b),  $\Delta \mathcal{F}_f$  (c), and  $\mathcal{P}_r$  (d) across different phases of the tilt test. Responses relative to the preceding phase are illustrated by point shapes and line colors: increases are shown by green squares with green lines, decreases by red triangles with red lines, and minimal variations (less than 1%) by black circles with gray lines.



#### FIGURE 5

Voltage maps representative of the induced fibrillatory pattern after application of S1-S2 stimulation. The ACh values represent the range of variation ( $\Delta$ ACh). All snapshots were taken at the 20<sup>th</sup> second from rotor initiation.

The state of the s									
ACh			2D		3D		Mean values		
	release 0.14 Hz		Iso (μM)		Iso (μM)				
ΔACh		0.0	0.005	1.0	0.0	0.005	1.0		
0.1	$\mathcal{F}_{\mathrm{f}}^{s}$	8.02	8.35	8.97	7.12	8.25	8.80	$\overline{\mathcal{F}_{\mathrm{f}}^{s}}$	8.25
0.1	$\Delta \mathcal{F}_{\mathrm{f}}^{s}$	0.14	0.14	0.14	0.13	0.13	0.13	$\overline{\Delta \mathcal{F}_{\mathrm{f}}^{s}}$	0.13
0.025	$\mathcal{F}_{\mathrm{f}}^{s}$	8.20	8.51	9.01	7.37	8.50	9.12	$\overline{\mathcal{F}_{\mathrm{f}}^{s}}$	8.37
0.025	$\Delta \mathcal{F}_{\mathrm{f}}^{s}$	0.03	0.03	0.03	0.03	0.03	0.03	$\overline{\Delta \mathcal{F}_f^s}$	0.03

TABLE 3  $\mathcal{F}_{\epsilon}^{s}$  and  $\Delta \mathcal{F}_{\epsilon}^{s}$  (Hz) computed from 2D and 3D simulations.

Regarding the variations in  $\Delta \mathcal{F}_{\rm f}^s$  with ACh and Iso, we found that  $\Delta \mathcal{F}_{\rm f}^s$  was mainly dependent on the range of ACh concentration variation, with its magnitude augmenting as the range increased, while Iso played a less relevant role. For the lowest ACh variation range of 0.025  $\mu$ M,  $\Delta \mathcal{F}_{\rm f}^s$  was around 0.03 Hz. For the largest ACh variation range of 0.1  $\mu$ M,  $\Delta \mathcal{F}_{\rm f}^s$  varied from 0.13 Hz (for the 2D cases) to 0.14 Hz (for the 3D cases).

# 4 Discussion

In this study, we analyzed ECGs of psAF patients undergoing a tilt table test and we computationally simulated the electrophysiology of the human atria to assess the relationship between ANS activity and f-wave frequency characterization.

We decided to analyze phases by distinguishing between transient and steady-state responses to postural changes in patients. In the study by Fois et al. (2022), the transient phases lasted approximately 1–1.5 min. In our dataset, these phases seemed to conclude around the 2-min mark. To avoid potentially overestimating the transient effects, we opted to consider slightly longer transient durations potentially including some of the steady-state.

Based on the analysis of the clinical data, substantial changes in  $\mathcal{F}_{\rm f}$  were observed across B, HDT and HUT, both in transient and steady states. There was a decrease in  $\mathcal{F}_{\rm f}$  transitioning from B to HDT, followed by an increase when transitioning from HDT to HUT. A similar behavior was observed in  $\mathcal{F}_{\rm HR}$ . The most pronounced change in  $\Delta\mathcal{F}_{\rm f}$  occurred during the HDT phase, with a significant increase from B2 to HDT1 and a significant decrease from HDT1 to HDT2. During the HUT phase,  $\Delta\mathcal{F}_{\rm f}$  increased from HDT2 to HUT1 and then stabilized. A similar behavior was observed for  $\mathcal{P}_{r}$ .

Generally, the behavior of  $\mathcal{F}_{HR}$  and  $\mathcal{F}_f$  was shown to largely vary among individuals, with a relevant number of cases deviating from the overall trend. Inter-patient variability may arise from physiological differences among individuals, such as underlying health conditions, genetic predispositions and individual pharmacokinetic profiles, as well as from the use of  $\beta$ -blockers.

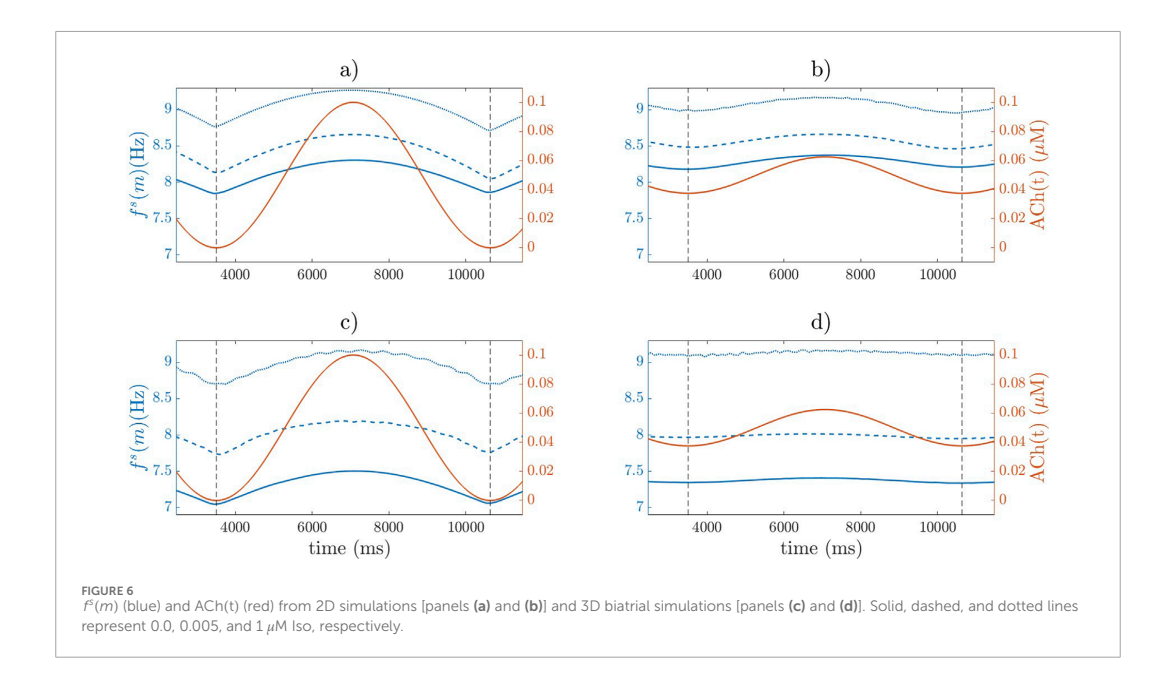
Through simulations, we found that increasing or decreasing the Iso concentration caused a corresponding increase or decrease in  $\mathcal{F}_{s}^{s}$ . Additionally, increasing the minimum ACh concentration

led to a reduction in APD and resulted in a slight increase in  $\mathcal{F}_f^s$  (Supplementary Figure S1 in the Supplementary Material). Moreover, the level of ACh variation was found to be correlated with  $\Delta \mathcal{F}_f^s$ , as already shown in Celotto et al. (2024). Regarding the effects of the respiratory frequency, we only simulated a frequency of 0.14 Hz, corresponding to the average respiratory frequency of the patients in the various phases. Based on our previous study, we expect that variations in the respiratory rate within the 0.125–0.33 Hz range would not significantly affect  $\mathcal{F}_f^s$ , or phase matching between ACh concentration variation and f(m) (Celotto et al., 2024).

A large number of studies have postulated an increase in SS during HUT in subjects in sinus rhythm (SR) (Cooke et al., 1999; Furlan et al., 2000; Whittle et al., 2022). This could be explained by the fact that during the transition to the HUT position, there is a sudden decrease in venous return, prompting a compensatory response from the sympathetic nervous system to maintain blood pressure. In our study, this observation is further reinforced in the context of AF. Specifically, the increase in  $\mathcal{F}_f$  that we observed in response to the HUT maneuver in AF patients is consistent with the increase in  $\mathcal{F}_f^s$  that we measured for increased Iso in our simulations.

Although there is scarce research on the autonomic effects during HDT, some studies in SR have associated the slowing of  $\mathcal{F}_{HR}$ during HDT with both an increase in PSS and a decrease in SS (Whittle et al., 2022; Porta et al., 2014). Only one study reported a decrease in both PSS and SS (Malhotra et al., 2021). In the case of AF or atrial flutter, some studies have linked the observed outcomes to an increase in PSS (Mase et al., 2008; Östenson et al., 2017). The findings of this work are not fully in line with those studies in AF, since PSS, causing a shortening of the effective refractory period, actually leads to an increase in  $\mathcal{F}_f^s$ , as reported in the literature and confirmed by our simulations (Sarmast, 2003). In our observations, there is a slight reduction in  $\mathcal{F}_f$  when going from B2 to HDT1 and no significant difference from HDT1 to HDT2. However, patients exhibit heterogeneous behavior, with 25% of patients showing an increase, 50% showing a decrease in  $\mathcal{F}_f$  and 25% showing no substantial change during HDT1 with respect to B2 and HDT2 with respect to HDT1, with larger inter-subject variability observed during HDT2. Simultaneously, in the majority of patients (75%), an increase in  $\Delta F_f$  was observed during HDT1, which may indicate an increased parasympathetic predominance. Based on the results of our study, these HDT-induced changes could be explained by a reduction in SS and an increase in PSS predominance. In the case of  $\mathcal{F}_f$ , the reduction in SS and the increase in PSS may be balanced in some cases and not in others, leading to either an increase or a decrease in Ff depending on which effect is predominant (if the extent of SS decrease predominates over the PSS increase, a reduction in  $\mathcal{F}_f$  would be expected, and vice versa).

During HDT2, we observed a decrease in  $\Delta\mathcal{F}_f$  compared to its value in HDT1, followed by an increase in  $\Delta\mathcal{F}_f$  during HUT1. This behavior could be attributed to the differing time course of PSS and SS effects. Parasympathetic activation affects the heart rate almost immediately and briefly, with inputs occurring every 2–4 s. In contrast, SS has longer latency effects, receiving inputs every 20–40 s and producing effects that last longer (Pizzo et al., 2022; Nair et al., 2023). Additionally, the continued stimulation by ACh might lead to the build-up of inhibitory substances that counteract its effects. This could dampen the  $\Delta\mathcal{F}_f$  response even while  $\mathcal{F}_f$  remains elevated.



This is supported by the fact that the release of ACh in the mammalian heart has been reported to be modulated by a negative feedback mechanism (Wetzel and Brown, 1985; Manabe et al., 1991).

The inclusion of simulations in our study provided useful insights into the expected direction of the changes in the mean f-wave frequency and the magnitude of respiratory modulation during PSS and SS.

We did not incorporate studies involving direct microneurography measurements of sympathetic activity or in vivo ACh concentration changes during maneuvers such as tilt testing for model validation, as we could not identify studies specifically linking tilt testing, microneurography, and AF. Instead, we based our validation on more global electrophysiological markers, such as CV and total atrial activation time (Bayer et al., 2019; Sanders et al., 2003), as well as f-wave frequencies (Stridh et al., 2003; Holmqvist et al., 2005), which have been extensively studied in relation to autonomic modulation and AF.

The simulation methods employed in this study build upon well-established modeling approaches that have been previously validated in the literature. The Courtemanche model and its adaptations have been widely used to simulate atrial electrophysiology, including the effects of autonomic modulation (Courtemanche et al., 1998). The ionic current modifications used to implement the effects of ACh and  $\beta$ -adrenergic stimulation on atrial electrophysiology were based on experimentally characterized data (Kneller et al., 2002; González de la Fuente et al., 2013).

The observed discrepancies in the absolute values in clinical data and simulations (around 2 Hz in  $\mathcal{F}_f$  and 0.1–1 Hz in  $\Delta\mathcal{F}_f$ ) could be attributed to various factors, which can arise from limitations in either the clinical data or the simulations.

In this regard, we performed one additional simulation at the 2D level (Supplementary Figure S1 in the Supplementary Material). Particularly, we reduced the level of psAF electrical remodeling by 50%, resulting in an increase in APD $_{90}$  of the baseline AP (no ACh, no Iso) of 25%. These modifications led to a reduction in  $\Delta\mathcal{F}_{\rm f}$  of 0.85 Hz. However, with the longer APD $_{90}$ , it would have been more difficult to establish long-lasting rotors in the 2D tissue. Nevertheless, we believe that the qualitative conclusions remain valid, and that the observed differences can be partially attributed to generally longer APs in the patients. In this sense, matching the dominant frequency observed in simulations and clinical recordings may be useful to estimate the degree of electrical remodeling in each patient.

Furthermore, while in the simulations the modulation of the fibrillatory rate is determined only by ACh and Iso, in the clinical signals the changes in the f-wave frequency characteristics in response to HDT and HUT can possibly be attributed to additional factors beyond the ANS modulation. Among such factors, mechanical stretch and mechano-electrical feedback should be considered, as they have been reported to exert significant contribution to atrial electrical activity in patients with atrial flutter (Mase, et al., 2009; Ravelli et al., 2008; Waxman et al., 1991). A study conducted by Waxman et al. (1991) examined various interventions, including passive upright tilting, the strain phase of the Valsalva maneuver and expiration, and all of them were found to reduce the cardiac size. Interestingly, regardless of the autonomic activity, these interventions were found to independently increase the rate of atrial flutter. Similarly, Ravelli et al. (2008) found that acute atrial stretch caused by ventricular contractions and respiratory movements resulted in a shortening of the atrial flutter CL in humans. Importantly, even after blocking autonomic

influences, oscillations in the atrial flutter CL were still present, further supporting the idea that factors beyond autonomic activity contribute to these oscillations.

The simulation results suggest that impaired sympathetic activity leads to a reduced increase in  $\mathcal{F}_f$  in response to HUT, while impaired parasympathetic activity results in lower  $\Delta\mathcal{F}_f$  values. The results from the analysis of clinical data reveal moderate changes in  $\mathcal{F}_f$  and low  $\Delta\mathcal{F}_f$  values, potentially indicating impairments in both sympathetic and parasympathetic activity, consistent with the clinical characteristics of the study cohort (Table 1).

From a clinical point of view, by elucidating the specific effects of sympathetic and parasympathetic activity on f-wave frequency modulation, clinicians could tailor pharmacological interventions targeting the ANS more effectively. For example, medications that selectively modulate sympathetic or parasympathetic activity could be prescribed based on an individual patient's autonomic profile, potentially leading to improved rhythm control and symptom management (Vandenberk et al., 2023; Chen et al., 2014). Additionally, autonomic modulation of f(m) could serve as a marker for stratifying patients based on their risk of AF progression or complications. Identifying these patients early on could prompt more intensive monitoring and intervention strategies to mitigate their risk. Finally, insights into autonomic influences on f(m) modulation could also inform personalized lifestyle interventions aimed at reducing AF burden and improving overall cardiovascular health.

# 4.1 Limitations

Some limitations of this study should be acknowledged to provide direction for further work.

One of the main limitations of the present study is the small sample size. The results suggest that changes in  $\mathcal{F}_f$  and  $\Delta \mathcal{F}_f$  in response to HUT and HDT are moderate, with considerable interpatient variability. Consequently, these findings should be validated in a larger study population.

This study analyzed ECG recordings from a subset of 24 patients from an original cohort of 40 patients (Östenson et al., 2017). The exclusion was based on the availability and quality of ECG signals: 11 patients were excluded due to missing ECG recordings, and 5 additional patients were excluded due to insufficient ECG signal quality for f-wave analysis. Although excluding low-quality ECGs improves the reliability of the results, it also limits the representativeness of our sample in relation to the full 40-patient cohort (cf. Table1).

The dataset did not provide access to individual patient data, such as age, sex, AF duration, comorbidities and use of drugs. These factors are known to influence the ANS, and hence lack of detailed patient information hampers a deeper exploration of how these factors might interact with the autonomic responses measured, potentially affecting the interpretation and applicability of our results.

Given that 80% of the original 40-patient cohort were diagnosed with hypertension and treated with  $\beta$ -blockers, it is highly likely that the majority of the 24 patients analyzed share these characteristics. However, without detailed individual-level data, we

cannot explicitly confirm these conditions for each patient included in our analysis. These characteristics of the study cohort may limit the generalizability of our findings across the broader population of AF patients, potentially biasing our results toward individuals with more pronounced autonomic disturbances associated with hypertension and the use of  $\beta$ -blockers.

Another limitation of this study is the absence of a direct ground truth measurement for respiration, as we did not use an independent reference method (e.g., spirometry or respiratory belts) to validate the ECG-derived respiratory signal. While the ECG-derived respiratory signal has been widely used in prior studies (Kontaxis et al., 2019) and provides valuable insights into respiration-related cardiac modulation, it remains an indirect estimate, and potential inaccuracies cannot be entirely ruled out. Additionally, the observed respiratory rate (0.13 Hz) is lower than typical resting respiration rates. Several physiological factors, including the use of beta-blockers, the supine position during tilttable testing, and the controlled quiet room environment, likely contributed to a slower spontaneous breathing rate. Despite these plausible explanations, the lack of direct respiratory measurements prevents us from direct verification of this effect. Future studies incorporating simultaneous direct respiratory monitoring would help validate and refine the precision of the ECG-derived respiration analysis in similar patient populations.

Focusing on the simulations, due to a lack of reported knowledge on the spatial distribution of sympathetic and parasympathetic innervation in the atria, we simply considered a random distribution of an equal number of sympathetic and parasympathetic nodes, to provide some evidence for the effects of the cholinergic and  $\beta$ -adrenergic stimulation.

Our computational models are deterministic and based on averaged patient data. Thus, they do not reproduce all the spectra of inter-patient variability but are representative of a mean psAF patient. Particularly, the use of a single anatomical model and a single model describing cellular electrophysiology may not have fully captured the inter-patient variability observed in the clinical scenario. Further investigations using other computational AP models with different steady-state APD values, as well as using populations of models, could be conducted to assess the impact of AP properties on f-wave frequency characterizations. Furthermore, AF-related structural remodeling of the atria may present with various alterations such as an enlarged atrial chamber, hypertrophy of cardiomyocytes, increased mismatch between epicardial and endocardial myofibers' orientations, changes in atrial wall thickness and, notably, an increased amount of fibrotic or connective tissue (Wyse et al., 2014; Schotten et al., 2011; Heijman et al., 2016). We represented psAF-related structural remodeling by a combination of gap junction remodeling, modeled through tissue conductance reduction in fibrotic regions, and fibroblast proliferation. Future studies incorporating different degrees of fibrosis as well as other psAF characteristics not accounted for in our model could delve deeper into the collective impact of these factors on  $\mathcal{F}_f$  and  $\Delta \mathcal{F}_f$ .

Finally, our current computational models do not allow us to assess the effects of ACh and Iso on  $\mathcal{F}_{HR}$ . However, future studies could incorporate a network model of the human AV node into the 3D model (Plappert et al., 2022), thereby making it suitable for evaluating fibrillatory effects on  $\mathcal{F}_{HR}$ .

# 5 Conclusion

The findings of this study suggest that elevated and reduced sympathetic activity following HUT and HDT, respectively, could contribute to the increase and decrease in  $\mathcal{F}_f$  measured in psAF patients. Parasympathetic activity, assessed by the magnitude of  $\Delta\mathcal{F}_f$  could exert a modulating role on the effects of sympathetic activity.

# Data availability statement

The data analyzed in this study is subject to the following licenses/restrictions: The data is owned by the Department of Cardiology, Clinical Sciences, Lund University, Sweden. Requests to access these datasets should be directed to pyotr.platonov@med.lu.se.

# **Ethics statement**

The studies involving humans were approved by Regionala Etikprövningsnämnden i Lund. The studies were conducted in accordance with the local legislation and institutional requirements. The participants provided their written informed consent to participate in this study.

## **Author contributions**

MA: Conceptualization, Writing – original draft, Writing – review and editing. CC: Conceptualization, Writing – original draft, Writing – review and editing. CS: Conceptualization, Supervision, Writing – review and editing. FP: Writing – review and editing. SÖ: Writing – review and editing. PP: Supervision, Writing – review and editing. PL: Conceptualization, Supervision, Writing – review and editing. EP: Conceptualization, Supervision, Writing – review and editing. FS: Conceptualization, Supervision, Writing – review and editing.

## References

Abdollahpur, M., Engström, G., Platonov, P. G., and Sandberg, F. (2022). A subspace projection approach to quantify respiratory variations in the f-wave frequency trend. Front. Physiology 1929. doi:10.3389/fphys.2022.976925

Abdollahpur, M., Holmqvist, E., Platonov, P. G., and Sandberg, F. (2021). Respiratory induced modulation in f-wave characteristics during atrial fibrillation. *Front. Physiology* 12, 653492. doi:10.3389/fphys.2021.653492

Bailon, R., Sörnmo, L., and Laguna, P. (2006). A robust method for ECG-based estimation of the respiratory frequency during stress testing. *IEEE Trans. bio-medical Eng.* 53, 1273–1285. doi:10.1109/TBME.2006.871888

Bayer, J. D., Boukens, B. J., Krul, S. P. J., Roney, C. H., Driessen, A. H. G., Berger, W. R., et al. (2019). Acetylcholine delays atrial activation to facilitate atrial fibrillation. *Front. Physiology* 10, 1105. doi:10.3389/fphys.2019.01105/phys.2019.01105

Celotto, C., Sánchez, C., Abdollahpur, M., Sandberg, F., Laguna, P., and Pueyo, E. (2023) "Dependence of atrial fibrillatory rate variations induced by head-up/down tilt-test on autonomic action," in 2023 computing in Cardiology (CinC), 50. IEEE, 1–4.

Celotto, C., Sanchez, C., Abdollahpur, M., Sandberg, F., Rodriguez, J. F., Laguna, P., et al. (2022). Effects of acetylcholine release spatial distribution on the frequency of atrial reentrant circuits: a computational study. Comput. Cardiol. (CinC) 498, 1–4. doi:10.22489/CinC.2022.396

# **Funding**

The author(s) declare that financial support was received for the research and/or publication of this article. This work was supported by the European Union's Horizon 2020 research and innovation programme under the Marie Sklodowska-Curie grant agreement No. 766082, the Swedish Research Council (grant VR2019-04272) and the Crafoord Foundation (grant 20200605), by Ministerio de Ciencia e Innovación, Spain, through projects PID2022-140556OB-I00 and TED2021-130459B-I00 and by European Social Fund (EU) and Aragón Government through projects LMP94\_21, LMP141\_21 and BSICoS group T39\_23R.

# Conflict of interest

The authors declare that the research was conducted in the absence of any commercial or financial relationships that could be construed as a potential conflict of interest.

# Publisher's note

All claims expressed in this article are solely those of the authors and do not necessarily represent those of their affiliated organizations, or those of the publisher, the editors and the reviewers. Any product that may be evaluated in this article, or claim that may be made by its manufacturer, is not guaranteed or endorsed by the publisher.

# Supplementary material

The Supplementary Material for this article can be found online at: https://www.frontiersin.org/articles/10.3389/fphys.2025. 1498426/full#supplementary-material

Celotto, C., Sánchez, C., Abdollahpur, M., Sandberg, F., Rodriguez Mstas, J. F., Laguna, P., et al. (2024). The frequency of atrial fibrillatory waves is modulated by the spatiotemporal pattern of acetylcholine release: a 3D computational study. Front. Physiology 14, 1189464. doi:10.3389/fphys.2023.1189464

Cha, T.-J., Ehrlich, J. R., Zhang, L., Chartier, D., Leung, T. K., and Nattel, S. (2005). Atrial tachycardia remodeling of pulmonary vein cardiomyocytes: comparison with left atrium and potential relation to arrhythmogenesis. *Circulation* 111, 728–735. doi:10.1161/01.CIR.0000155240.05251.D0

Chang, H.-Y., Lo, L. W., Chou, Y. H., Lin, W. L., Lin, Y. J., Yamada, S., et al. (2016). Effect of vagotomy on the activity of cardiac autonomic ganglia: insight from left atrial high density frequency mapping. *Int. J. Cardiol.* 220, 435–439. doi:10.1016/j.ijcard.2016.06.1832016.06.183

Chelu, M. G., Sarma, S., Sood, S., Wang, S., Van Oort, R. J., Skapura, D. G., et al. (2009). Calmodulin kinase ii-mediated sarcoplasmic reticulum ca 2+ leak promotes atrial fibrillation in mice. *J. Clin. investigation* 119, 1940–1951. doi:10.1172/jci37059

Chen, P.-S., Chen, L. S., Fishbein, M. C., Lin, S.-F., and Nattel, S. (2014). Role of the autonomic nervous system in arrial fibrillation: pathophysiology and therapy. Circulation Res. 114, 1500–1515. doi:10.1161/CIRCRESAHA.114.303772 Cooke, W. H., Hoag, J. B., Crossman, A. A., Kuusela, T. A., Tahvanainen, K. U., and Eckberg, D. L. (1999). Human responses to upright tilt: a window on central autonomic integration. J. Physiology 517 (Pt 2), 617-628. doi:10.1111/j.1469-7793.1999.0617tx

Courtemanche, M., Ramirez, R. J., and Nattel, S. (1998). Ionic mechanisms underlying human atrial action potential properties: insights from a mathematical model. *Am. J. Physiology-Heart Circulatory Physiology* 275, H301–H321. doi:10.1152/ajpheart.1998.275.1.H301

Courtemanche, M., Ramirez, R. J., and Nattel, S. (1999). Ionic targets for drug therapy and atrial fibrillation-induced electrical remodeling: insights from a mathematical model. Cardiovasc. Res. 42, 477–489. doi:10.1016/S0008-6363(99)00034-6

Dimmer, C., Tavernier, R., Gjorgov, N., Van Nooten, G., Clement, D. L., and Jordaens, L. (1998). Variations of autonomic tone preceding onset of atrial fibrillation after coronary artery bypass grafting. *Am. J. Cardiol.* 82, 22–25. doi:10.1016/s0002-9149(98)00231-8

Dobrey, D., Graf, E., Wettwer, E., Himmel, H., Hala, O., Doerfel, C., et al. (2001). Molecular basis of downregulation of g-protein–coupled inward rectifying k+ current (lk, ach) in chronic human atrial fibrillation: decrease in girk4 mrna correlates with reduced lk, ach and muscarinic receptor–mediated shortening of action potentials. Circulation 104, 2551–2557. doi:10.1161/hc4601.099466

Ferrer, A., Sebastián, R., Sánchez-Quintana, D., Rodríguez, J. F., Godoy, E. J., Martínez, L., et al. (2015). Detailed anatomical and electrophysiological models of human atria and torso for the simulation of atrial activation. *PloS One* 10, e0141573. doi:10.1371/journal.pone.0141573

Fioranelli, M., Piccoli, M., Mileto, G. M., Sgreccia, F., Azzolini, P., Risa, M. P., et al. (1999). Analysis of heart rate variability five minutes before the onset of paroxysmal atrial fibrillation. *Pacing Clin. Electrophysiol. PACE* 22, 743–749. doi:10.1111/j.1540-8159.1999.th00538 x

Fois, M., Maule, S. V., Giudici, M., Valente, M., Ridolfi, L., and Scarsoglio, S. (2022). Cardiovascular response to posture changes: multiscale modeling and *in vivo* validation during head-up tilt. *Front. Physiology* 13, 826989. doi:10.3389/fphys.2022.826989

Freeman, R. (2006). Assessment of cardiovascular autonomic function. Clin. Neurophysiol. 117, 716–730. doi:10.1016/j.clinph.2005.09.027

Furlan, R., Porta, A., Costa, F., Tank, J., Baker, L., Schiavi, R., et al. (2000). Oscillatory patterns in sympathetic neural discharge and cardiovascular variables during orthostatic stimulus. *Circulation* 101, 886–892. doi:10.1161/01.cir.101.8.8868.886

González de la Fuente, M., Barana, A., Gomez, R., Amoros, I., Dolz-Gaiton, P., Sacristan, S., et al. (2013). Chronic atrial fibrillation up-regulates  $\beta$ 1-adrenoceptors affecting repolarizing currents and action potential duration. *Cardiovasc. Res.* 97, 379–388. doi:10.1093/cvr/cvs313

Gould, P. A., Yii, M., McLean, C., Finch, S., Marshall, T., Lambert, G. W., et al. (2006). Evidence for increased atrial sympathetic innervation in persistent human atrial fibrillation. *Pacing Clin. Electrophysiol. PACE* 29, 821–829. doi:10.1111/j.1540-8159.2006.00447.x

Heidenreich, E. A., Ferrero, J. M., Doblaré, M., and Rodríguez, J. F. (2010). Adaptive marcinite elements for the numerical solution of monodomain equations in cardiac electrophysiology. *Ann. Biomed. Eng.* 38, 2331–2345. doi:10.1007/s10439-010-9997-2

Heijman, J., Algalarrondo, V., Voigt, N., Melka, J., Wehrens, X. H., Dobrev, D., et al. (2016). The value of basic research insights into atrial fibrillation mechanisms as a guide to therapeutic innovation: a critical analysis. *Cardiovasc. Res.* 109, 467–479. doi:10.1093/cvr/cvv275

Henriksson, M., Petrenas, A., Marozas, V., Sandberg, F., and Sornmo, L. (2018a). Model-based assessment of f-wave signal quality in patients with atrial fibrillation, IEEE Trans. Biomed. Eng., Model-based Assess. f-wave signal Qual. patients Atr. fibrillation 65, 2600–2611. doi:10.1109/TBME.2018.2810508

Henriksson, M., Petrenas, A., Marozas, V., Sandberg, F., and Sornmo, L. (2018b). Model-based assessment of f-wave signal quality in patients with atrial fibrillation. *IEEE Trans. Biomed. Eng.* 65, 2600–2611. doi:10.1109/TBME.2018.28105082018.2810508

Herweg, B., Dalal, P., Nagy, B., and Schweitzer, P. (1998). Power spectral analysis of heart period variability of preceding sinus rhythm before initiation of paroxysmal atrial fibrillation. *Am. J. Cardiol.* 82, 869–874. doi:10.1016/s0002-9149(98)00494-9

Hindricks, G., Potpara, T., Dagres, N., Arbelo, E., Bax, J. J., Blomström-Lundqvist, C., et al. (2021). 2020 esc guidelines for the diagnosis and management of atrial fibrillation developed in collaboration with the european association for cardio-thoracic surgery (eacts) the task force for the diagnosis and management of atrial fibrillation of the european society of cardiology (esc) developed with the special contribution of the european heart rhythm association (ehra) of the esc. Eur. heart J. 42, 373–498. doi:10.1093/curhearti/ehaa612

Holmqvist, F., Stridh, M., Waktare, J. E. P., Brandt, J., Sörnmo, L., Roijer, A., et al. (2005). Rapid fluctuations in atrial fibrillatory electrophysiology detected during controlled respiration. *Am. J. Physiology-Heart Circulatory Physiology* 289, H754–H760. doi:10.1152/ajpheart.00075.2005

Joglar, J. A., Chung, M. K., Armbruster, A. L., Benjamin, E. J., Chyou, J. Y., Cronin, E. M., et al. (2024). 2023 ACC/AHA/ACCP/HRS guideline for the diagnosis and management of atrial fibrillation: a report of the American college of cardiology/American heart association joint committee on clinical practice guidelines. Circulation 149, e1–e156. doi:10.1161/CIR.000000000001193

Kneller, J., Zou, R., Vigmond, E. J., Wang, Z., Leon, L. J., and Nattel, S. (2002). Cholinergic atrial fibrillation in a computer model of a two-dimensional sheet of canine atrial cells with realistic ionic properties. Circulation Res. 90, E73–E87. doi:10.1161/01.RES.0000019783.88094.BA

Kontaxis, S., Lázaro, J., Corino, V. D., Sandberg, F., Bailón, R., Laguna, P., et al. (2019). ECG-derived respiratory rate in atrial fibrillation. *IEEE Trans. Biomed. Eng.* 67, 905–914. doi:10.1109/TBME.2019.2923587

Lankveld, T. A. R., Zeemering, S., Crijns, H. J. G. M., and Schotten, U. (2014). The ECG as a tool to determine atrial fibrillation complexity. *Heart British Card. Soc.* 100, 1077–1084. doi:10.1136/heartjin-2013-305149

Li, D., Zhang, L., Kneller, J., and Nattel, S. (2001). Potential ionic mechanism for repolarization differences between canine right and left atrium. *Circulation Res.* 88, 1168–1175. doi:10.1161/hl101.091266

MacCannell, K., Bazzazi, H., Chilton, L., Shibukawa, Y., Clark, R. B., and Giles, W. R. (2007). A mathematical model of electrotonic interactions between ventricular myocytes and fibroblasts. *Biophysical J.* 92, 4121–4132. doi:10.1529/biophysj.106.101410

Malhotra, V., Thakare, A. E., Hulke, S. M., Wakode, S. L., Parashar, R., and Ravi, N. (2021). Effect of head down tilt on heart rate variability. J. Fam. Med. Prim. Care 10, 439–442. doi:10.4103/fjmpc.jfmpc\_1642\_20

Manabe, N., Foldes, F. F., Torocsik, A., Nagashima, H., Goldiner, P. L., and Vizi, E. S. (1991). Presynaptic interaction between vagal and sympathetic innervation in the heart: modulation of acetylcholine and noradrenaline release. *J. Aut. Nerv. Syst.* 32, 233–242. doi:10.1016/0165-1838/91190117-1

Mase, M., Disertori, M., and Ravelli, F. (2009). Cardiorespiratory interactions in pase, the atrial flutter. J. Appl. Physiology Bethesda, Md. 106 (106), 29–39. doi:10.1152/japplphysiol.91191.2008

Mase, M., Glass, L., and Ravelli, F. (2008). A model for mechano-electrical feedback effects on atrial flutter interval variability. *Bull. Math. Biol.* 70, 1326–1347. doi:10.1007/s11538-008-391-x

Nair, S. S., Govindankutty, M. M., Balakrishnan, M., Prasad, K., Sathyaprabha, T. N., and Udupa, K. (2023). Investigation of autonomic dysfunction in alzheimer's disease-a computational model-based approach. *Brain Sci.* 13, 1322. doi:10.3390/brainsci13091322

Östenson, S., Corino, V. D. A., Carlsson, J., and Platonov, P. G. (2017). Autonomic influence on atrial fibrillatory process: head-up and head-down tilting. *Ann. Noninvasive Electrocardiol.* 22, e12405. doi:10.1111/anec.12405

Park, J., Lee, C., Leshem, E., Blau, I., Kim, S., Lee, J. M., et al. (2019). Early differentiation of long-standing persistent atrial fibrillation using the characteristics of fibrillatory waves in surface ECG multi-leads. *Sci. Rep.* 9, 2746. doi:10.1038/s41598-019-2009.

Pizzo, E., Berrettoni, S., Kaul, R., Cervantes, D. O., Di Stefano, V., Jain, S., et al. (2022). Heart rate variability reveals altered autonomic regulation in response to myocardial infarction in experimental animals. Front. Cardiovasc. Med. 9, 843144. doi:10.3389/fcvm.2022.843144

Plappert, F., Engstrom, G., Platonov, P. G., Wallman, M., and Sandberg, F. (2024). ECG-based estimation of respiration-induced autonomic modulation of AV nodal conduction during atrial fibrillation. Front. Physiology 15, 1281343. doi:10.3389/fphys.2024.1281343

Plappert, F., Wallman, M., Abdollahpur, M., Platonov, P. G., Östenson, S., and Sandberg, F. (2022). An atrioventricular node model incorporating autonomic tone. Front. Physiology 13, 976468. doi:10.3389/fphys.2022.976468

Platonov, P. G., Corino, V. D. A., Seifert, M., Holmqvist, F., and Sornmo, L. (2014). Atrial fibrillatory rate in the clinical context: natural course and prediction of intervention outcome. Eur. Eur. Pacing, Arrhythm. Cardiac Electrophysiol. J. Work. Groups Cardiac Pacing, Arrhythm. Cardiac Cell. Electrophysiol. Eur. Soc. Cardiol. 16 (Suppl. 4), iv110-iv119. doi:10.1093/europace/euu249

Platonov, P. G., Mitrofanova, L. B., Orshanskaya, V., and Ho, S. Y. (2011). Structural abnormalities in atrial walls are associated with presence and persistency of atrial fibrillation but not with age. *J. Am. Coll. Cardiol.* 58, 2225–2232. doi:10.1016/j.jacc.2011.05.061

Porta, A., Marchi, A., Bari, V., Catai, A. M., Guzzetti, S., Raimondi, F., et al. (2014) "Directionality in cardiovascular variability interactions during head-down tilt test," in Annual international Conference of the IEEE Engineering in Medicine and biology society. IEEE Engineering in Medicine and biology society. Annual international conference 2014, 6008–6011. doi:10.1109/EMBC.2014.6944998

Ravelli, F., Mase, M., and Disertori, M. (2008). Mechanical modulation of atrial flutter cycle length. *Prog. Biophysics Mol. Biol.* 97, 417–434. doi:10.1016/j.pbiomolbio.2008.02.018

Rohr, S., Kucera, J. P., and Kléber, A. G. (1998). Slow conduction in cardiac tissue, is effects of a reduction of excitability versus a reduction of electrical coupling on microconduction. *Circulation Res.* 83, 781–794. doi:10.1161/01.res.83.8.781

Sanders, P., Morton, J. B., Davidson, N. C., Spence, S. J., Vohra, J. K., Sparks, P. B., et al. (2003). Electrical remodeling of the atria in congestive heart failure: electrophysiological and electroonatomic mapping in humans. *Circulation* 108, 1461–1468. doi:10.1161/01.CIR.000099688.49283.67

Sarmast, F., Kolli, A., Zaitsev, A., Parisian, K., Dhamoon, A. S., Guha, P. K., et al. (2003). Cholinergic atrial fibrillation: Ik, ACh gradients determine unequal left/right atrial frequencies and rotor dynamics. Cardiovasc. Res. 59, 863–873. doi:10.1016/s0008-6363(03)00540-61016/S0008-6363(03)00540-6

Schotten, U., Verheule, S., Kirchhof, P., and Goette, A. (2011). Pathophysiological mechanisms of atrial fibrillation: a translational appraisal. *Physiol. Rev.* 91, 265–325. doi:10.1152/physrev.00031.2009

Seemann, G., Hoper, C., Sachse, F. B., Dossel, O., Holden, A. V., and Zhang, H. (2006). Heterogeneous three-dimensional anatomical and electrophysiological model of human atria. *Philosophical Trans. Ser. A, Math. Phys. Eng. Sci.* 364, 1465–1481. doi:10.1098/rsta.2006.1781

Sornmo, L. (2018). Atrial fibrillation from an engineering perspective, series in bioengineering (Springer).

Stridh, M., Meurling, C., Olsson, B., and Sornmo, L. (2003). Detection of autonomic modulation in permanent atrial fibrillation. *Med. and Biol. Eng. and Comput.* 41, 625–629. doi:10.1007/BF02349969

Tomita, T., Takei, M., Saikawa, Y., Hanaoka, T., Uchikawa, S.-I., Tsutsui, H., et al. (2003). Role of autonomic tone in the initiation and termination of paroxysmal atrial fibrillation in patients without structural heart disease. *J. Cardiovasc. Electrophysiol.* 14, 559–564. doi:10.1046/j.1540-8167.2003.02462.x1540-8167.2003.02462.x

Vandenberk, B., Haemers, P., and Morillo, C. (2023). The autonomic nervous system in atrial fibrillation-pathophysiology and non-invasive assessment. Front. Cardiovasc. Med. 10, 1327387. doi:10.3389/fcvm.2023.1327387389/fcvm.2023.13273873

Varon, C., Lázaro, J., Bolea, J., Hernando, A., Aguiló, J., Gil, E., et al. (2019). Unconstrained estimation of hrv indices after removing respiratory influences from heart rate. *IEEE J. Biomed. Health Inf.* 23, 2386–2397. doi:10.1109/JBHI.2018.2884644

Wang, Z., Fermini, B., and Nattel, S. (1993). Sustained depolarization-induced outward current in human atrial myocytes. Evidence for a novel delayed rectifier

K+ current similar to Kv1.5 cloned channel currents. Circulation Res. 73, 1061–1076. doi:10.1161/01.res.73.6.1061

Wang, Z. G., Pelletier, L. C., Talajic, M., and Nattel, S. (1990). Effects of flecainide and quinidine on human atrial action potentials. Role of rate-dependence and comparison with Guinea pig, rabbit, and dog tissues. *Circulation* 82, 274–283. doi:10.1161/01.cir.82.1.274

Waxman, M. B., Yao, L., Cameron, D. A., and Kirsh, J. A. (1991). Effects of posture, Valsalva maneuver and respiration on atrial flutter rate: an effect mediated through cardiac volume. *J. Am. Coll. Cardiol.* 17, 1545–1552. doi:10.1016/0735-1097/91)90645-P

Wesselink, R., Neefs, J., van den Berg, N. W. E., Meulendijks, E. R., Terpstra, M. M., Kawasaki, M., et al. (2022). Does left atrial epicardial conduction time reflect atrial fibrosis and the risk of atrial fibrillation recurrence after thoracoscopic ablation? post hoc analysis of the AFACT trial. BMJ open 12, e056829. doi:10.1136/bmjopen-2021-056829

Wetzel, G. T., and Brown, J. H. (1985). Presynaptic modulation of acetylcholine relaese from cardiac parasympathetic neurons. *Am. J. Physiology* 248, H33–H39. doi:10.1152/ajpheart.1985.248.1.H331152/ajpheart.1985.248.1.

Whittle, R. S., Keller, N., Hall, E. A., Vellore, H. S., Stapleton, L. M., Findlay, K. H., et al. (2022). Gravitational dose-response curves for acute cardiovascular hemodynamics and autonomic responses in a tilt paradigm. *J. Am. Heart Assoc.* 11, e024175. doi:10.1161/JAHA.121.024175

Wyse, D. G., Van Gelder, I. C., Ellinor, P. T., Go, A. S., Kalman, J. M., Narayan, S. M., et al. (2014). Lone atrial fibrillation. *J. Am. Coll. Cardiol.* 63, 1715–1723. doi:10.1016/j.iacc.2014.01.023

Xie, Y., Grandi, E., Puglisi, J. L., Sato, D., and Bers, D. M. (2013). β-adrenergic stimulation activates early afterdepolarizations transiently via kinetic mismatch of pka targets. J. Mol. Cell. Cardiol. 58, 153–161. doi:10.1016/j.yjmcc.2013.02.009

 $\overline{P}aper\ IV$ 

# A Chamber Study of Respiratory and Autonomic Responses to Hydrotreated Vegetable Oil Exhaust Using ECG-Derived Respiration (Manuscript)

Mostafa Abdollahpur<sup>a</sup>, Louise Gren<sup>b</sup>, Katrin Dierschke<sup>c</sup>, Leo Stockfelt<sup>d,e</sup>, Aneta Wierzbicka<sup>b</sup>, Frida Sandberg<sup>a</sup>

<sup>a</sup>Department of Biomedical Engineering, Lund University, Lund, Sweden
<sup>b</sup>Ergonomics and Aerosol Technology Lund University, Lund, Sweden
<sup>c</sup>Division of Occupational and Environmental Medicine, Lund University, Lund, Sweden
<sup>d</sup>Department of Occupational and Environmental Medicine, Sahlgrenska University

Hospital, Gothenburg, Sweden

<sup>e</sup>Occupational and Environmental Medicine, School of Public Health and Community Medicine, Institute of Medicine, University of Gothenburg, Gothenburg, Sweden

# Abstract

Background: Air pollution is a major public health concern, contributing to cardiovascular and respiratory diseases. One of the main pathways by which air pollution affects cardiovascular health is through dysregulation of the autonomic nervous system (ANS), which impairs cardiac control. Hydrotreated vegetable oil (HVO) is a renewable fuel with unknown toxicity in comparison to conventional diesel, and the effects of HVO exhaust on autonomic and respiratory regulation remain unclear. Objective: This study investigates the physiological responses to HVO exhaust exposure by assessing heart rate variability (HRV), ECG-derived respiration (EDR) and cardiorespiratory coupling (CRC). Methods: A controlled exposure study was conducted with 19 healthy volunteers (10 males, 9 females, aged 20–55) who underwent four different exposure scenarios in a randomized, double-blind design: filtered air, filtered air with NaCl particles, HVO exhaust with an aftertreatment system, and HVO exhaust without aftertreatment. ECG

signals were continuously recorded, and HRV, EDR, and CRC features were extracted. A linear mixed model was used to assess time- and exposure-dependent changes. **Results:** No statistically significant differences in HRV, EDR, or CRC features were found between exposure scenarios. **Conclusion:** In this study, short-term exposure to HVO exhaust, corresponding to EU OELs for one workday, did not significantly alter autonomic or respiratory regulation in healthy volunteers at the studied pollutant concentrations.

Keywords: Hydrotreated Vegetable Oil (HVO), Heart Rate Variability (HRV), ECG-Derived Respiration (EDR), Cardiorespiratory Coupling (CRC), Mutual Information (MUI), Air Pollution

# Open Access of this manuscript

The full manuscript will be available for open access after publication in a peer reviewed journal.